Theses and Dissertations--Electrical and Computer Engineering

Electrical and Computer Engineering

2021

Electric Power Systems and Components for Electric Aircraft

Damien Lawhorn
University of Kentucky, damien.lawhorn@uky.edu
Author ORCID Identifier:
https://orcid.org/0000-0002-3642-3983
Digital Object Identifier: https://doi.org/10.13023/etd.2021.134

Recommended Citation

STUDENT AGREEMENT:

I represent that my thesis or dissertation and abstract are my original work. Proper attribution has been given to all outside sources. I understand that I am solely responsible for obtaining any needed copyright permissions. I have obtained needed written permission statement(s) from the owner(s) of each third-party copyrighted matter to be included in my work, allowing electronic distribution (if such use is not permitted by the fair use doctrine) which will be submitted to UKnowledge as Additional File.

I hereby grant to The University of Kentucky and its agents the irrevocable, non-exclusive, and royalty-free license to archive and make accessible my work in whole or in part in all forms of media, now or hereafter known. I agree that the document mentioned above may be made available immediately for worldwide access unless an embargo applies.

I retain all other ownership rights to the copyright of my work. I also retain the right to use in future works (such as articles or books) all or part of my work. I understand that I am free to register the copyright to my work.

REVIEW, APPROVAL AND ACCEPTANCE

The document mentioned above has been reviewed and accepted by the student's advisor, on behalf of the advisory committee, and by the Director of Graduate Studies (DGS), on behalf of the program; we verify that this is the final, approved version of the student's thesis including all changes required by the advisory committee. The undersigned agree to abide by the statements above.

<div align="right">

Damien Lawhorn, Student

Dr. Dan M. Ionel, Major Professor

Dr. Daniel L. Lau, Director of Graduate Studies

</div>

Electric Power Systems and Components for Electric Aircraft

DISSERTATION

A dissertation submitted in partial fulfillment of the requirements for the
degree of Doctor of Philosophy in the College of Engineering at the
University of Kentucky

By

Damien Lawhorn

Lexington, Kentucky

Director: Dr. Dan M. Ionel, Professor and L. Stanley Pigman Chair in Power

Lexington, Kentucky

2021

ABSTRACT OF DISSERTATION

ELECTRIC POWER SYSTEMS AND COMPONENTS FOR ELECTRIC

AIRCRAFT

Electric aircraft have gained increasing attention in recent years due to their potential for environmental and economic benefits over conventional airplanes. In order to offer competitive flight times and payload capabilities, electric aircraft power systems (EAPS) must exhibit extremely high efficiencies and power densities. While advancements in enabling technologies have progressed the development of high performance EAPS, further research is required.

One challenge in the design of EAPS is determining the best topology to be employed. This work proposes a new graph theory based method for the optimal design of EAPS. This method takes into account data surveyed from a large set of references on commonly seen components including electric machines, power electronics and jet engines. Thousands of design candidates are analyzed based on performance metrics such as end-to-end system efficiency, overall mass, and survivability. It is also shown that sensitivity analysis may be used to systematically evaluate the impact of components and their parameters on various aspects of the architecture design.

Once an EAPS architecture has been selected, further, detailed, validation of the power system is required. In these EAPS, many subsystems exist with timescales varying from minutes to hours when considering the aerodynamics, to nanosecond dynamics in the power electronics. This dissertation presents a multiphysics co-simulation framework for the evaluation of EAPS with a unique decoupling method to reduce simulation time without sacrificing detail. The framework has been exemplified on a case study of a 500kW all-electric aircraft, including models for aerodynamics, energy storage, electric motors and power electronics.

Electric machines for aviation propulsion must meet several performance requirements, including a constant power speed range (CPSR) of approximately thirty percent above rated speed. This operation is traditionally achieved through the flux weakening technique with an injection of negative d-axis current. However, the degree of CPSR achievable through flux weakening is a strong function of the back emf and d-axis inductance. This dissertation reviews alternative methods for CPSR operation in machines with low inductance. A new method of current weakening has been proposed to address this challenge, involving reducing the machine's current inversely proportional to the operating speed, maintaining constant power through the extended speed range. One benefit of the proposed method is that all current is maintained in the q-axis, maintaining maximum torque per ampere operation.

Coreless axial flux permanent magnet (AFPM) machines have recently gained significant attention due to their specific form factor, potentially higher power density and lower losses. Coreless machine designs promise high efficiency particularly at higher speeds, due to the absence of a ferromagnetic core. In this dissertation, coreless AFPM machines with PCB stators are investigated as candidates for propulsion in electric aircraft applications. Two PCB stator design variations are presented with both simulation and experimental results.

KEYWORDS: Electric aircraft, power system optimization, co-simulation, electric machine drives, PCB stator, axial flux permanent magnet.

Author's signature:_____Damien Lawhorn_____

Date:_____May 11, 2021_____

Electric Power Systems and Components for Electric Aircraft

By

Damien Lawhorn

Director of Dissertation: <u>Dr. Dan M. Ionel</u>

Director of Graduate Studies: <u>Dr. Daniel Lau</u>

Date: <u>May 11, 2021</u>

To my father

ACKNOWLEDGEMENTS

First and foremost, I would like to express my upmost gratitude to my advisor, Professor Dan M. Ionel, Ph. D., FIEEE, L. Stanley Pigman Chair in Power, who has always supported me in academic, professional, and personal growth. Since I took his electric class on Electric Vehicles – Electromechanical Components and System and then joined the SPARK Laboratory, he never wavered to provide his wisdom and guidance to help me pursue my goals. The many hours he has spent with me planning, discussing, and reviewing my work have been invaluable to shaping this dissertation. Under his caring mentorship, I was able to learn how to navigate research, collaboration, and even daunting tasks, as well as what "more and better" may help you achieve. The service that he done for me, not only for directing my PhD studies with dedication and foresight, but also for always believing in me and my potential for success is a debt that I will never be able to repay. I am grateful for all of his many teachings over the past four years, and how they will be valued utilities in the coming years as a professional. I am thankful to him not only for encouraging me to pursue my Ph.D., but for providing me with an atmosphere that fostered growth while doing so.

I am very grateful to Dr. Vandana Rallabandi, an outstandingly knowledgeable mentor with whom I was fortunate to work during her postdoctoral fellowship with the SPARK laboratory. I am proud to count her a close friend. I would also like to thank all my colleague students in our SPARK Laboratory and academic family for their friendship and collaboration.

I would like to thank my parents, Patrick Lawhorn and Tara Mayes, who always encouraged me to chase my dreams and taught me to value kindness, honesty, and diligence. They pushed for me to become the best version of myself and were there to

hold me up every step of the way. I would not have been where I am today without their selfless sacrifices and constant encouragement.

Last, but not least, my most special gratitude goes to my wife, Gracie Lawhorn, for accompanying me through my PhD years with her unwavering support and love.

<div align="right">

Damien Lawhorn

April, 2021

</div>

Contents

List of Figures

List of Tables

Chapter 1

Introduction and Problem Formulation

1.1 Background

Electric aircraft concepts and demonstrators have become increasing more popular in the past decade. Environmental awareness across the world has been one motivator for this movement towards the electrification of flight. With over a quarter of the global greenhouse emissions originate from the transportation economic sector, and a substantial portion of those are due to aerial traffic, a significant impact may be made by decreasing the amount of fossil fuel used in aircraft. Electric airplanes show great potential not only to reduce carbon emissions, but also acoustic pollution when compared with conventional planes. A shift from traditional jet engines to more electric propulsion may be the answer to a quieter sky. In addition to these benefits, the operating costs associated with electric aircraft may be lower once the technology matures. The largest expense for airliners is fuel, leading to a reasonable benefit to a

transition since electricity is less expensive than jet fuel.

With recent advancements in enabling technologies across multiple engineering disciplines, the development of electric transportation available for both the private and commercial aviation industries is becoming more viable. However, there are still many challenges that must be overcome. In the process of transitioning from traditional combustion propulsion, be it jet engines or propeller driven aircraft, significant redesign of the power system is required. Mass is one key aspect of many that must be considered in this process. In the case of combustion propulsion, the primary fuel has an energy density on the order of 11kWh/kg. For comparison, Lithium-Ion, the leading battery energy storage chemistry, has an energy density on the order of 0.3kWh/kg. Additionally, unlike a conventional system, fuel mass is not burned throughout the flight, so more energy is required for the same flight. In order to ensure that an all-electric or partially electric propulsion system meets an aircraft's mission objectives, special care must be taken in every aspect of the design process, from system architectures to subsystem components.

When considering the architecture of an electric aircraft power system (EAPS), a designer is faced with a multi-objective problem. An ideal EAPS would be one that is the lightest while maintaining a high reliability and also has a very high operating efficiency. However, many times these performance parameters are competing in the sense that an improvement in one leads to a degraded outcome in another. For

example, a safer aircraft may be obtained by adding multiple components in parallel to ensure redundancy and fault tolerance, but this would lead to an increase in mass, which is undesirable. Therefore, a main contribution this dissertation will focus on is the design of optimal EAPS topologies.

As there is much room for innovation regarding system level design, subsystem components also contribute greatly to the overall performance of the aircraft. In recent years, there has been a rise in the availability of wide bandgap (WBG) semi-conductor devices for commercial and research applications. These WBG devices are desirable because they offer significant benefits over their traditional Silicon counterparts such as increased power density, efficiency, switching speed, and reliability. The aeronautics industry in general is an ideal application area for WBG devices, primarily owing to the strong necessity to minimize mass on-board the vehicle and to operate as efficiently as possible. Furthermore, aircraft with partial or fully electric propulsion systems show even more potential benefits from the use of these devices, considering the portion of the aircraft mass associated with the electric power system is of greater significance. Primarily due to smaller on-resistances and negligible reverse recovery, WBG devices are much more efficient than traditional Silicon, enabling converter efficiencies of greater than 98 percent. In the case of an electric aircraft, this not only provides an advantage in operating costs and reduction in energy usage, but also by reducing the mass and volume penalties that are required for waste heat

dissipation. Such power electronic converters have been developed in the SPARK lab at UK and have been used in this dissertation research to demonstrate a new current weakening control technique.

In addition to the previously mentioned advanced in power electronics and controls, there is much need for electric machines with high performance. Electric aircraft have high power demands and require the propulsion systems to be lightweight to carry greater payload and to provide longer flights. There has been debate among experts which electric machine topology is most suitable for aircraft propulsion. High efficiency is desired to reduce waste heat, leading to additional mass associated with thermal management, as well as to reduce energy usage and operating costs. Specific power, reliability, fault tolerance, torque ripple, and noise are all other key factors for propulsion motors. Coreless axial-flux permanent magnet (AFPM) synchronous machines have been studied in transportation applications and have been noted for their high power density, compactness, and efficiency. This dissertation investigates coreless AFPM machines and their suitability for electric aircraft applications.

1.2 Literature Review

Over the past decade, the conceptual development of new, partially-electric and all-electric aircraft has been accelerated. The integration of electric powertrain technologies in aircraft has lead to various system architectures. Larger aircraft concepts,

Table 1.1: Example Electric Aircraft Power and Energy Ratings

Aircraft	Turbogenerators	EMs	Batteries	PV
NASA N3-X [1]	30.6 MW (2)	4.42 MW (14)	None	None
Airbus/Siemens/Rolls-Royce E-Fan X [45]	2 MWh (1)	2 MW (4)	2 MW	None
Eviation Alice [46]	None	260 kW (3)	900 kWh	None
Airbus E-Fan[47]	None	32 kW (2)	29 kWh	None
Solar Impulse 2 (HB-SIB) [48]	None	13 kW (4)	164 kWh	66 kW
QinetiQ Zephyr 7 [49]	None	450 W (2)	3 kWh	N/A
Autonomous Systems Laboratory AtlantikSolar [50]	None	420 W (1)	73 Wh	275 W

intended to serve long-haul missions with many passengers often include turbogenerators such as those in NASA's N3-X concept plane (Fig. 1.1) [1]. Turbo-electric topologies like this one incorporate electric machines for propulsion, but include little to no energy storage. At the other extreme, smaller scale aircraft, such as the Zepyhr 7 designed by QinetiQ, frequently incorporate solar arrays and battery energy storage (BES) (Fig. 1.2) [2]. In between lie all-electric topologies for thin-haul missions like the X-57 by NASA [1] and the hybrid-electric airplanes such as seen by Airbus, Siemens, and Rolls-Royce [45]. A sample of system ratings in recent electric aircraft are included in Table 1.1.

A vehicle's mission is typically predetermined, and the aircraft general topology of turbo-electric, hybrid-electric, or all-electric can be set based on its goals. However, once this is decided, there are many choices for a designer to make concerning the layout of the power system. One example in the literature of this process is illustrated in the development of Turboelectric Distributed Propulsion (TeDP) technology [51]. When assessing various architectures, the authors weigh several metrics associated with the system including weight, failure response, component count, and breath of
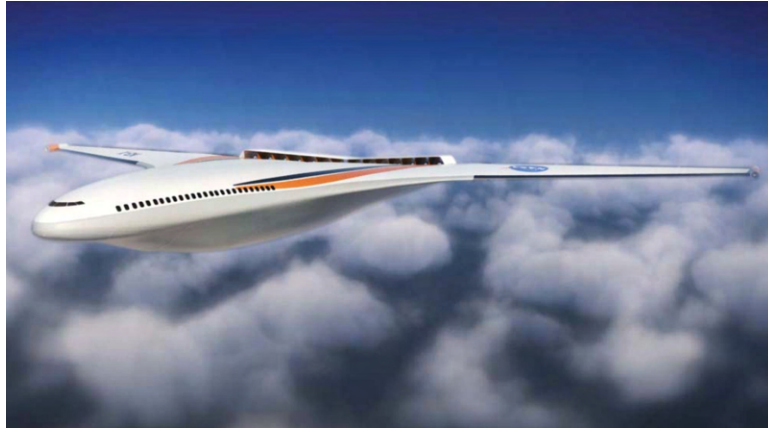
Figure 1.1: NASA N3-X concept turboelectric aircraft. The N3-X utilizes two wing-tip mounted gas-turbine-driven superconducting electric generators [1].

the protection scheme. It is shown that several of these metrics are in competition, such as weight and the breath of the protection scheme, both of which valuable contributors to the overall performance of the aircraft. Alternative methods for topology interpretations are presented in [52].

The transition to more electric aircraft propulsion systems will require subsystem components to have exceptionally high power density and efficiencies. Since mass and efficiency are of upmost importance in the development of an EAPS, researchers are investigating the use of unique approaches in several categories including wiring, electric machines, power electronics, and battery technologies. For applications of hybrid and turbo-electirc aircraft, NASA Glenn Research Center is currently developing a high efficiency megawatt machine (HEMM), with target goals including a power rating of 1.4MW, greater than 98 percent efficiency, and a power density

Figure 1.2: The Airbus ZephyrT high altitude pseudo-satellite. This is the larger of the Zephyr series of solar aircraft designed for military and commercial use [2].

greater than 16kW/kg [53]. In order to meet these high performance goals, an unconventional machine topology is used consisting of a semi-slotless stator with an internally-cryocooled, superconducting rotor. To drive such machines for the next generation of aircraft, equally high performance standards are placed on the power electronics. With the utilization of advanced converter topologies and wide bandgap semiconductor devices, MW rated power converters are being tested with ultra-high 99 percent efficiency and power densities of 12kW/kg [54].

Detailed literature reviews are distributed throughout this dissertation and included in each chapter. These cover power system optimization techniques in chapter 2, methods for multi-physics simulations of electric vehicles in chapter 3, methods of extended speed range operation in chapter 4, and existing coreless and slotless electric machines, and design considerations for PCB stators in chapter 5.

1.3 Research Objectives and Original Contributions

Statement of problem

At the conceptual design stage of an airplane, there are many variables that are available for selection and modification. While certain characteristics of the system may be set by aircraft goals such as desired fuel savings, maximum lifting capability, and flight endurance, multiple power system topologies may satisfy the same initial aircraft objectives. In such an instance, it is beneficial to determine which architectures yield the best performance. Aircraft performance metrics may include mass, efficiency, reliability, and survivability. Often these performance metrics are competing in the sense that an improvement in one leads to a degradation in the other. One challenge this dissertation seeks to address is the need for a design procedure for EAPS architecture optimization. A novel method for EAPS optimization is introduced in this dissertation. Through decomposition of an EAPS into a graph consisting of nodes, which represent components, and edges, which define the interconnection, methods of graph theory are used to evaluate topology performance. A software implementation of this approach has been completed and employed to analyze thousands of candidate designs to provide the user insight into strengths and weaknesses of each architecture.

Once an architecture is determined, multi-physics simulation is used to verify

validity of selected design over a specified mission profile. These simulations often include models of various subsystems such as aerodynamic and power generation and distribution. In the case of EAPS, time constants across the subsystems vary greatly. For example, aerodynamics may change in seconds, while power electronic converter simulations require nanosecond time steps. If simulated together, this leads to very long computational times, which can slow the design process significantly. This challenge opens an avenue for improved multi-physics simulation techniques, especially since power electronics are becoming even faster with the latest generation Silicon Carbide and Gallium Nitride switching devices.

These emerging technologies for power converters come with several opportunities and challenges. More diverse applications can be served in a similar or smaller footprint due to WBG device's much higher voltage ratings when compared to traditional Silicon based devices. This enables the use of unconventional techniques for increased performance, such as the current weakening approach discussed in chapter 4, that may have added prohibitively mass or volume when implemented with conventional devices.

Electric aircraft power systems require components which show very high performance capabilities with respect to power output, power density, efficiency, noise and reliability. Two electric machine variations which have gained recent attention for use in transportation applications are coreless and slotless machines, both of the radial

and axial-flux arrangements. This dissertation discusses recent coreless and slotless machines in the literature and considerations for the design of AFPM machines with PCB stators. The applicability of these machines for electric aircraft propulsion is examined and performance is experimentally evaluated.

The main **original contributions**, which will be described throughout the dissertation, may be briefly enumerated as:

- Development of a graph theory-based method for the optimization of EAPS architectures. The developed software framework allows system designers to evaluate thousands of candidate designs. The optimization method utilizes component data based on an extensive survey and evaluated each topology based on performance metrics such as efficiency, total mass, and survivability. (Chapter 2)

- A co-simulation software framework for multi-physics evaluation of electric plane EAPS architectures, electrical components, and airframe has been developed. Novelty lies in the decoupling method proposed for the reduction of effective simulation times while maintaining investigative capabilities. (Chapter 3)

- A method for extending the constant power speed range in low inductance machines with simulation and experimental validation. This current weakening

approach addresses the challenges posed by the limited field weakening capability of low inductance permanent magnet synchronous machines. (Chapter 4)

- Analysis and prototyping of two novel coreless axial flux permanent magnet machine designs with PCB implemented stator windings. Theses designs show potential for suitability in aircraft propulsion applications based on the designed machine scaled to higher power ratings. (Chapter 5).

1.4 Dissertation Outline

In order to address the design of electric aircraft propulsion power systems, the following chapters have been included. Chapter 2 proposes a novel approach to the optimization of an aircraft's propulsion system using graph theory. This method provides insight into the benefits and drawbacks of many power system topologies that satisfy user input constraints. Chapter 3 discusses a method of electric aircraft co-simulation, which considers the dynamics associated with the power electronics, electric machines, as well as the vehicle body. All of these system dynamics generally occur on a vastly different timescales, which can lead to prohibitively long calculation times if simulated together. The proposed simulation framework offers a decoupled solution for faster calculations while still capturing important information regarding transients. In response to the trend of low inductance motors used in electric vehicles,

Chapter 4 discusses the challenges associated with traditional field weakening operation of these motors, as well as a systematic review of existing methods of extending the speed range. Furthermore, a new method is proposed with experimental demonstration. In chapter 5, the requirements for electric machines in hybrid and electric aircraft propulsion applications are discussed. Additionally, the design considerations of coreless axial flux permanent magnet machines utilizing PCB stators is discussed and two designs are proposed with experimental results. Conclusions and proposed future works are provided in Chapter 6.

1.5   Publications

- Lawhorn, D., Rallabandi, V., and Ionel, D. M., "Multi-objective Optimization for Aircraft Power Systems using a Network Graph Representation," IEEE Transactions on Transportation Electrification, Vol. 7, doi: 10.1109/TTE.2021.3066123., 11p (2021)

- Lawhorn, D. Lewis, P. Han, and Ionel, D. M., "On the Design of Coreless Permanent Magnet Machines for Electric Aircraft Propulsion", Proceedings, IEEE ITEC 2021, Online, 6p (*Accepted for publication*, Jun 2021)

- Lawhorn, D., Rallabandi, V., and Ionel, D. M., "A Network Graph Technique for the Design of Electric Aircraft Power Systems", Proceedings, IEEE ITEC 2020, Chicago, IL, 4p (Jun 2020)

- Lawhorn, D., Rallabandi, V., and Ionel, D. M., "Scalable Graph Theory Approach for Electric Aircraft Power System Optimization", Proceedings, AIAA/IEEE EATS 2019, Indianapolis, IN, 5p (Aug 2019)

- Lawhorn, D., Rallabandi, V., and Ionel, D. M., "Electric Aircraft System Co-simulation including Body, Propeller, Propulsion, and Energy Storage Models", Proceedings, IEEE ITEC 2019, Novi, MI, 5p (Jun 2019)

- Lawhorn, D., Rallabandi, V., and Ionel, D. M., "Power Electronics Powertrain Architectures for Solar and Hybrid Aircraft with Distributed Propulsion", Proceedings, AIAA/ IEEE EATS 2018, Cincinnati, OH, 6p (Jul 2018)

- Lawhorn, D., Taran, N., Rallabandi, V., and Ionel, D. M., "A Comparative Study of Constant Power Operation Techniques for Low Inductance Machines", Proceedings, IEEE ITEC 2018, Long Beach, CA, doi: 10.1109/ITEC.2018.8450 184, 6p (Jun 2018)

- Zhang, Y., Lawhorn, D. L., Han, P., and Ionel, D. M., "Integrated AC to AC Converters for Single-phase Input to Two-phase Output Motor Drives," Proceedings, IEEE IEMDC 2021, Mohegan Sun, CT, 5p (*see SPARK website*, May 2021)

- Kesgin, M. G., Han, P., Lawhorn, D., and Ionel, D. M., "Analysis of Torque Production in Axial-flux Vernier PM Machines of the MAGNUS Type " Proceedings, IEEE IEMDC 2021, Mohegan Sun, CT, 5p (*see SPARK website*, May 2021)

- Kesgin, M. G., Han, P., Taran, N., Lawhorn, D., Lewis, D., and Ionel, D. M., "Design Optimization of Coreless Axial-flux PM Machines with Litz Wire and PCB Stator Windings," Proceedings, IEEE ECCE 2020, Detroit, MI, doi: 10.1109/ECCE44975.2020.9236194, pp. 22-26 (Oct 2020)

- Zhang, Y., Lawhorn, D. L., Han, P., Cramer, A. M., and Ionel, D. M., "Electric Drives with Wide Bandgap Devices for Two-Phase Very Low Inductance Machines," Proceedings, IEEE ECCE 2020, Detroit, MI, doi: 10.1109/ECCE44975. 2020.9235388, pp. 6125-6129 (Oct 2020)

- Lewis, D., Lawhorn, D., and Ionel, D. M., "On the Feasibility of Electrification for Large Mobile Cranes," Proceedings, IEEE ICRERA 2020, Glasgow, UK, doi: 10.1109/ICRERA49962.2020.9242871, pp. 467-470 (Sep 2020)

- Rallabandi, V., Lawhorn, D., Ionel, D. M., and Li, X., "Multi-Physics Modeling for Electric and Hybrid Vehicles with In-wheel Electric Motors", Proceedings, IEEE ITEC 2018, Long Beach, CA, doi: 10.1109/ITEC.2018.8450091, 6p (Jun 2018)

- Rallabandi, V., Lawhorn, D., He. J., and Ionel, D. M., "Current Weakening Control of AFPM Motor Drives for Solar Race Cars with a Three-port Bi-directional DC/DC Converter", Proceedings, IEEE ICRERA 2017, San Diego, CA, doi: 10.1109/ICRERA.2017.8191158, 6p (Nov 2017).

Chapter 2

Design Optimization for Aircraft Power Systems using a Network Graph Representation

2.1 Introduction and Formulation

Electric aircraft are becoming increasingly more popular, driven by incentives such as fuel efficiency, cost, and noise pollution. Manufacturers have already begun electrification of many auxiliary systems in today's planes, as well as the demonstration of electrically propelled aircraft. These studies have produced a large number of designs, all of which vary greatly with respect to the power system (Fig. 2.1). The question of how these different architectures may perform has led to the development of a tool which can be used to determine the optimal number of components and configuration within the power system.

When considering the electrification of air transport, the EAPS architectures may
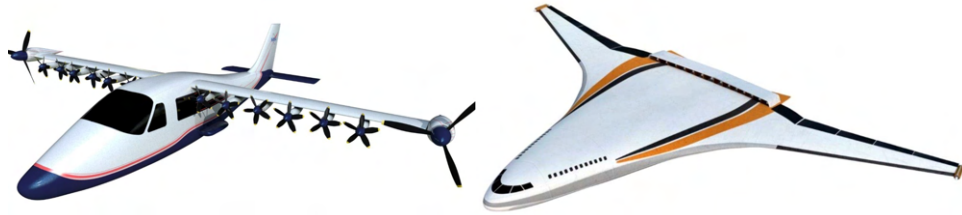
Figure 2.1: Example distributed electric propulsion aircraft designs by NASA with varying power system topologies. All-electric demonstrator X-57 Maxwell currently under development utilizing multiple electrical machines with varying ratings [3] (left). Conceptual turbo-electric N3-X aircraft which utilizes electrical energy from generators coupled to jet engines [4] (right).

be broken down into three main categories: all-electric, hybrid-electric, and turbo-electric. The first of these mentioned include a propulsion system which fully derives its energy from electrical storage means. With the current state of the technology's maturity, all-electric aircraft concepts are most commonly seen. In fact, several demonstrator aircraft have been constructed or are currently under development.

One of the first all-electric demonstrator aircraft to attract significant attention was the E-Fan developed by Airbus [55]. This 60kW, two-seater prototype was the only one produced and first flew in 2014, before Airbus transitioned to the development of their hybrid-electric aircraft concept. More recently, electric propulsion company, MagniX partnered with AeroTec to modify a Cessna 208B Grand Caravan to be electrically driven by MagniX's 560kW system in 2020 [56]. Another notable unique all-electric currently under development is NASA's all-electric X-57 (Fig. 1). This aircraft will not only serve as a demonstrator for electric machines in aviation,
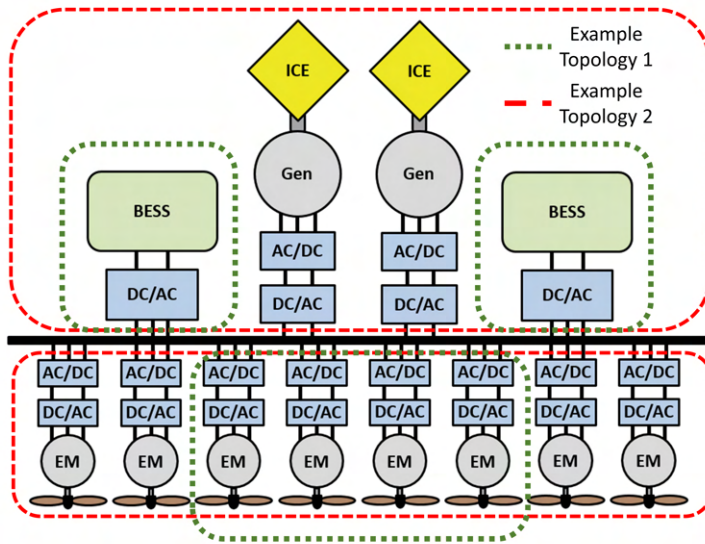
Figure 2.2: Example aircraft power system representations with a variable number and ratings of internal combustion engines (ICE), generators (Gen), rectifiers (AC/DC), inverters (DC/AC), battery energy storage systems (BESS), and electric motors (EM). The proposed graph theory based optimization approach identifies high performance candidates from the most general of architectures.

but also for a concept called distributed electric propulsion (DEP), which, according to studies, may increase flight efficiency further. While many organizations are showing that purely electric flight is a possibility, all-electric aircraft are typically seen to be short range and carry a limited number of passengers, due to the current limitations with lithium-ion energy storage energy density.

As current electrical energy storage means limit maximum payload and flight time in all-electric aircraft, researchers have proposed alternative approaches to incorporate further electrification into aircraft propulsion systems. The most commonly seen method of driving propulsion in modern commercial aircraft is through combustion jet engines, which is a proven technology that the industry has become well suited to manufacture. Electrification of these propulsion systems type may be achieved through the coupling an electrical generator to the turbine of a jet engine. This method allows the jet engine to perform its duty of producing lift while simultaneously generating electrical energy. A hybrid-electric aircraft power system includes significant energy storage means for the generated electricity, which may be used to drive electric machines connected to propulsors at any period during the flight. One hybrid-electric aircraft example concept is the E-Fan X, a collaborative effort between AirBus, Rolls-Royce, and Siemens [57].

Turbo-electric aircraft, in comparison, directly use the power produced by the jet turbine to drive the electrical propulsion motors, including little to no means of

electrical energy storage. Turbo-electric concepts generally offer a less massive design when compared to a hybrid considering the very small amount of battery used. This, however, makes the power system less flexible and decreases its potential for reduction of direct carbon emissions. Example turbo-electric aircraft concepts include NASA's Single-aisle Turbo-electric Aircraft with an Aft Boundary-Layer propulsor (STARC-ABL) and N3-X [58, 59].

At the preliminary design stage, an aircraft's mission is typically predetermined based on flight goals such as endurance, intended payload, etc. Generally, the aircraft topology of turbo-electric, hybrid-electric, or all-electric may be set based on its mission duration, primarily due to energy storage constraints. The leading electrical energy storage technology in electric vehicles, Lithium-ion, may possess a specific energy in the range of about 160 Wh/kg [60].

Fossil fuel, with an energy density two orders of magnitude higher, holds an advantage over electric energy storage. Thus, when considering electrical energy storage for a commercial airliner such as the Boeing 777, it may be expected that significantly more mass is required to achieve the same energy content as fossil fuel, and this severely limits the maximum flight time.

There are still many choices for a designer to make concerning the layout of a power system, including the degree of electrification, distribution type, number and rating of power conversion devices, energy storage systems, and propulsion units such

as motors and jet engines [61]. Determination of these free variables in the process is not a trivial question and requires detailed analysis.

In past EAPS design studies, a common approach is to construct a small set of candidate architectures and evaluate performance metrics compared to a baseline, such as the approach seen in [62]. When considering propulsion design, aerodynamics, thermal, and electrical systems are highly coupled. Multidisciplinary tools such as GT-HEAT of Georgia Institute of Technology, and GENUS of Cranfield University have been developed to assess integrated vehicle impacts of various subsystems [63, 64]. While, graph theory based methods have been employed recently for the design of microgrids and large electric ships to evaluate system reliability and cost, the applications to EAPS is less widely researched [65, 66].

This chapter proposes an approach, intended to be used as an early stage design tool, which utilizes mathematical methods involving graph theory to identify optimal solutions with regard to the electric aircraft power system (EAPS) configuration built off of the initial work conducted in [67]. This dissertation brings contributions, not only in applications to electric aircraft, but also in the theoretical development and the software implementation, as explained later in the chapter. Example results include performance trade-offs for an array of design candidates in the terms of efficiency, mass, and survivability.

The chapter is organized as follows. Section II presents considerations and a
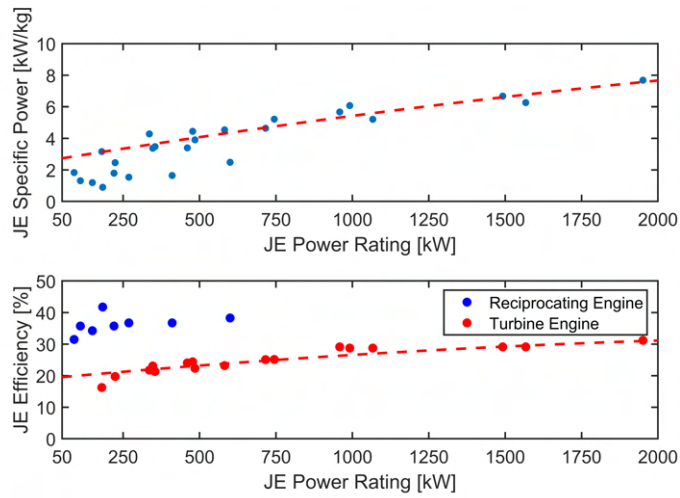
Figure 2.3: Survey of specific power and efficiency values for commercial jet engines, including both turbine and internal combustion engines based on a large set of references [5–11]. Trendlines shown are used in the EAPS model.

review of components commonly seen in EAPSs. Section III discusses the proposed optimization method based on predefined mission parameters including components characteristics outlined in the previous section. An example case study for a 500kW airplane using the framework is presented in Section IV. Based on the results from the case study, architecture performance sensitivity to the various components is discussed in Section V. The full chapter is concluded in Section VI.
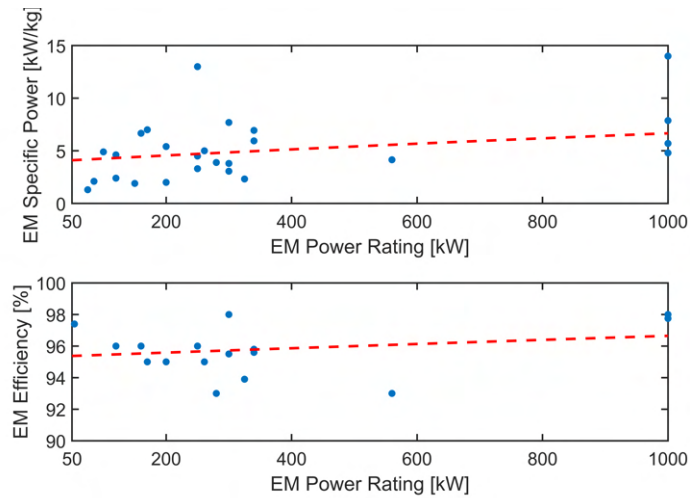
Figure 2.4: Collection of specific power and efficiency values for both academic and commercial electric machines designs based on a large set of references [12–25]. A trendline is extracted and used in the EAPS model.

2.2 Electric Aircraft Propulsion Component Survey

An EAPS may be represented in the form of a graph network in which the graphs nodes are determined by the components incorporated in the power system architecture. For an electric aircraft, these may include, but are not limited to electric machines, i.e. motors or generators, power converters, energy storage devices, and protection equipment (Fig. 2.2). Each component and its respective graphical node may be assigned characteristics including specific power or energy, operating efficiency, and failure rates. These characteristics may be constant values, such as a failure rate for a particular component, or they may vary with other variables related to that component. For example, efficiency may be calculated as a function

of the component's power rating and anticipated loading over the specified mission. In this study, surveys have been conducted to extract these parameters from both commercially available components and those reported in the literature.

2.2.1 Internal Combustion Engines

Airplanes are traditionally driven with one of two powerplants types to generate thrust. Reciprocating, or piston engines can commonly be seen on fixed-wing propeller aircraft or helicopters and are generally more inexpensive and easier to operate. These engines are used in lower power aviation applications such as training and short-haul missions. For use in higher power demand applications, aircraft adopt a power turbine. In fixed-wing designs a turboprop or jet turbine may be used, while in helicopters utilize turboshaft engines. An extensive survey was conducted to gather parametric data across commercial aviation reciprocating and turbine engines [5–11]. From this survey, second order polynomial fitting was used to represent the variations in specific power and efficiency with rated power, as illustrated in Fig. 2.3. Turbine internal combustion engine (ICE) efficiency in percent, η_{ICE}, was estimated using the following equation;

$$\eta_{ICE} = -1.46 * 10^{-6} P_{ICE}^2 + 8.95 * 10^{-3} P_{ICE} + 19.08, \tag{2.1}$$

where P_{ICE} represents the rated power of the ICE in kW. Similarly, the power-to-weight ratio of the engine can be represented as

$$sp_{ICE} = -3.03 * 10^{-7} P_{ICE}{}^2 + 3.15 * 10^{-3} P_{ICE} + 2.57, \qquad (2.2)$$

where sp_{ICE} is the specific power in kW/kg.

2.2.2 Electric Machines

Electric machines may serve several functions in an electric aircraft system. The most commonly envisioned propulsion application is the direct linkage of the electric machine to the propulsive device, be it a propeller or ducted fan. In this application the machine mainly operates in motoring mode, working to drive the propulsive device to generate lift for the aircraft. However, regeneration and emergency braking is also achievable by the device. In hybrid-electric and turbo-electric aircraft, electric machines may be coupled to the turbine of jet engines to serve as generators, providing electrical power to the energy storage or directly to motoring electric machines. In this configuration, the electric machines may also be used as starters for the jet engines. For use in the optimization framework, a collection of performance parameters in electric machines designed for vehicle applications was constructed, using the assumption only active mass has been reported (Fig. 2.4). The majority of electric machines used in transportation applications and for which data is publicly available, fall in power ranges below 500kW [12–25]. The specific powers and rated efficiencies

24

can vary significantly, as illustrated in Fig. 2.4. Therefore, if a least squares regression line was utilized as described for the combustion engines, a poor correlation may be the result. The efficiency and specific power are considered to increase with power rating, The goodness factor defined as the equation below:

$$G = \frac{2p^2\mu_o f}{\pi p_r g},$$

(2.3)

serves a dimensionless index which can be used to compare electric machines of different ratings [68]. Where p is the pole-pitch, p_r is the surface resistivity, and g is the air-gap length. It was shown that higher rated machines have a higher goodness. Further, as the power rating increases, inactive materials make up a smaller percentage of the overall weight, leading to higher specific power. Likewise, auxiliary losses comprise a smaller percentage of the overall loss. In addition, the probability of using expensive, low loss components is higher, all these factors contribute to a higher efficiency. Based off of the survey data, it has been assumed in this study that the power-to-weight ratio of electric machines increases linearly from 5 to 10 kW/kg as the power rating increases to 2.5MW. Similarly, the efficiency over this power range was assumed to increase linearly from 95 to 98 percent. Power rating of the electric machines has been determined based on the power requirements dictated by the mission profile, for the case study presented in this chapter, the aircraft has a total power rating of 500kW. Second order effects of fan drag, efficiency, and weight are neglected.

2.2.3 Power Electronics

Each electric machine represented in the aircraft designs must be utilized with the implementation of power electronic converters to condition the power where appropriate. A survey of performance characteristics for various industrial and academic power electronic converters has been conducted and is illustrated in Fig. 2.5. The survey consists solely of designs for three-phase, two-level inverters due to the fact that such a topology is the most common implementation for an electric vehicle motor drive application. Additional detail could be added to the modeling by including survey results for various motor and drive combinations. A logarithmic fitting has been used to generate a least squares regression line from the data points and is used in the optimization. Specific power, sp_{PE}, of the power electronic converters, or the power-to-weight ratio, has been estimated as

$$sp_{PE} = 3.47 + 2.78 log(P_{PE}), \tag{2.4}$$

where P_{PE} is the rated power of the power electronics. Typically, in matured technologies and applications of electric machines and power electronics, efficiency is expected to increase with rated power. These trends are noted in common practice and have theoretically demonstrated in the following chapter [68]. With EAPS technologies, there is large variation in between technological designs, which may explain the variations in the survey data. Due to the lack of efficiency reported by manufacturers, in
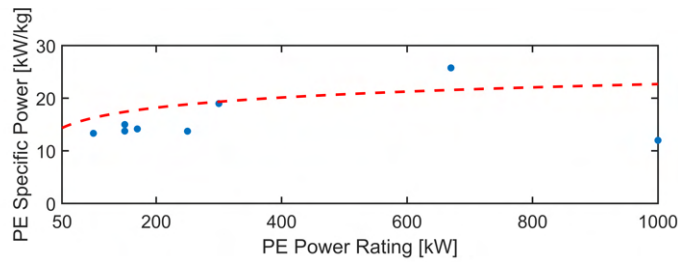
Figure 2.5: Survey of specific power and efficiency values for commercial and academic power electronic conversion devices, based on a large set of references [26–32]. Trendlines shown are used in the EAPS model.

this study the efficiency of the power electronics is assumed to follow a linear increase from 97 to 99 percent as power increases to 1MW.

2.2.4   Energy Storage

The studies conducted in this chapter and previous works show that energy storage systems are among the most influential components included in the design of an electric aircraft power system when considering mass. Although primarily dominated by Lithium-Ion battery technology, there are many studies on implementation of energy storage in electric transportation including supercapacitors, various forms of chemical batteries, fuel cells, and flywheels. In this study it is also important to consider the energy stored in jet fuel used in a hybrid topology. A survey of recent review papers on energy storage for electric vehicle applications was conducted and performance characteristics are illustrated in Fig. 2.6. As shown in Fig. 2.6, power and energy-to-weight ratios vary between energy storage technologies. Therefore, when calculating the mass of electrical energy storage, both power and energy ratings
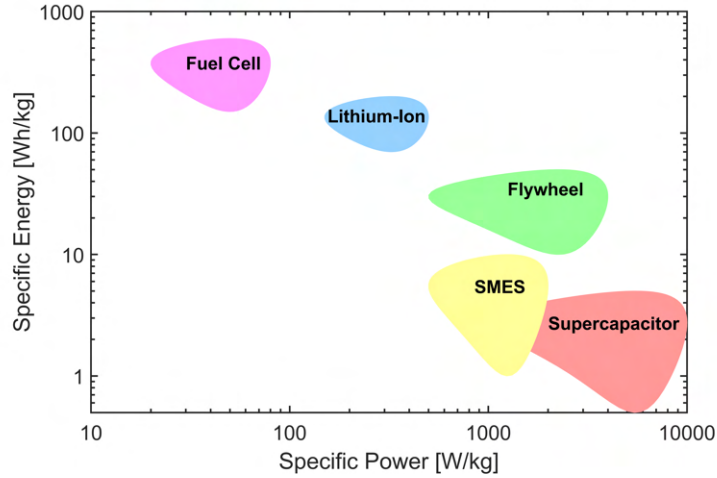
Figure 2.6: Ragone plot illustrating specific energy and power of various energy storage means usable in electrical transportation based off of references [33–35]. Survey conducted includes hydrogen fuel cells, lithium ion batteries, flywheels, superconducting magnetic energy storage (SMES), and supercapacitors. While a higher specific energy is typically favorable in electric propulsion, the specific power of the energy storage means must also be considered.
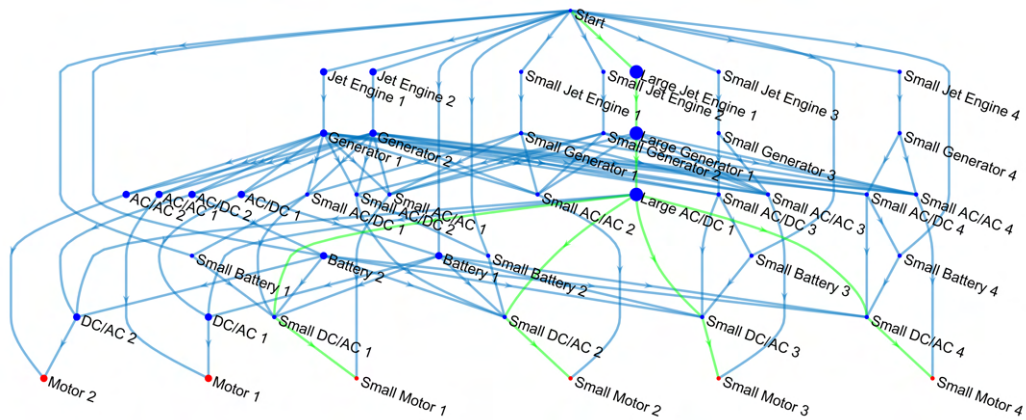
Figure 2.7: Graph containing power system components seen in hybrid and turbo-electric aircraft topologies with varying ratings. The illustrated graph represents thousands of potential candidate designs. The developed framework extracts valid subgraphs meeting the flight requirements, such as the one shown in green, for further analysis.
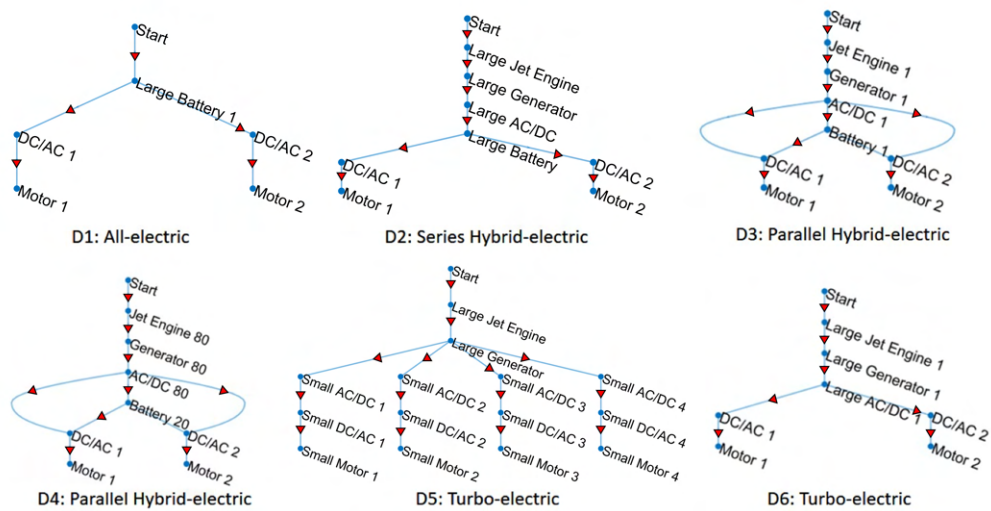
Figure 2.8: A collection of potential design candidates to fulfill an electric aircraft concept which meets the flight power and energy requirements predetermined by the system designer. All the shown topologies were selected automatically as subgraphs from a graph containing many designs. These architectures include purely turbo-electric, hybrid-electric and all-electric energy storage means.

are considered. In most applications, the energy rating is the dominate factor. However, in fuel cells for example, power rating may dictate mass, considering specific energy is higher than the specific power when compared to other technologies. Architectures which can make use of high power, lower energy applications such as energy recovery during landing, may favor storage means which have show higher specific power. For Lithium-ion batteries, which are based on a technology under accelerated development, relatively large variations of the specific energy with rating have been reported, making it difficult to conclude on an analytical relationship for the trends. For the studies reported in this chapter, it has been assumed that the specific energy for the battery remains constant at the typical value of 160Wh/kg [60].

29
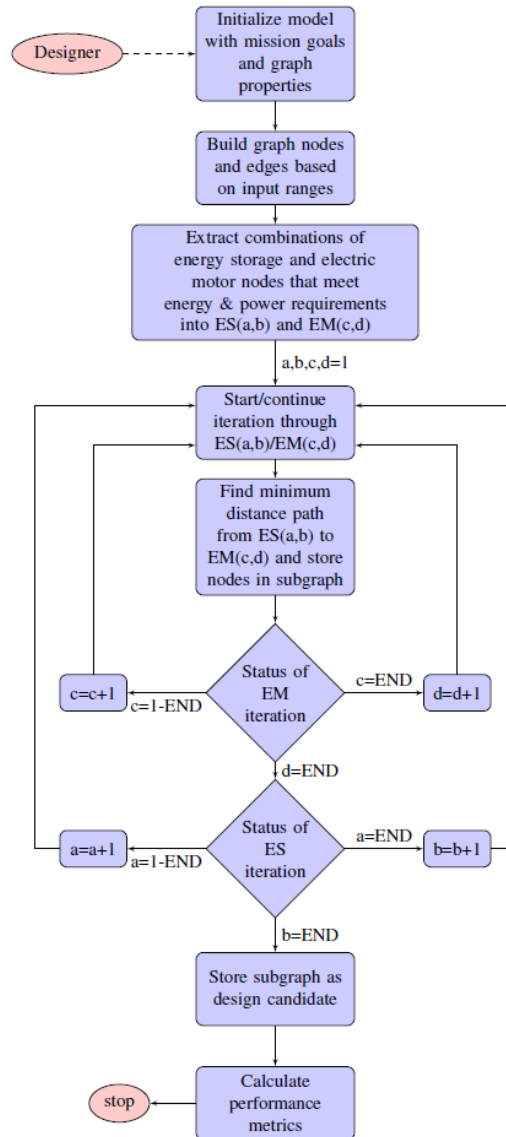
Figure 2.9: Workflow for the EAPS optimization process. The designer begins the approach by defining system characteristics and the framework outputs how viable power systems perform based on specified metrics. Example performance metrics include mass and efficiency.

30
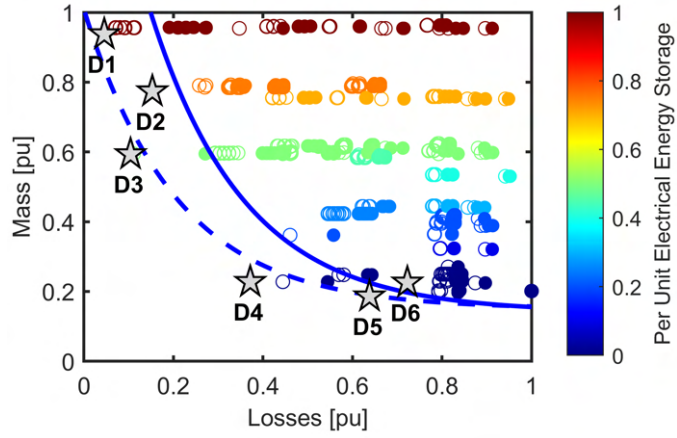
Figure 2.10: Total mass and losses for the entire power system of aircraft including combustion engine, electric generation, energy storage, power conversion and electric propulsion motor are shown as empty circles. Filled circles indicate designs that consider both power system and propulsion losses. The dashed and solid lines indicate generic pareto fronts for both calculations. Designs with purely electrical energy storage have the highest efficiency (D1) and turbo-electric designs are least massive (D5 and D6). Hybrid designs such as D2-D4 tradeoff mass and losses.
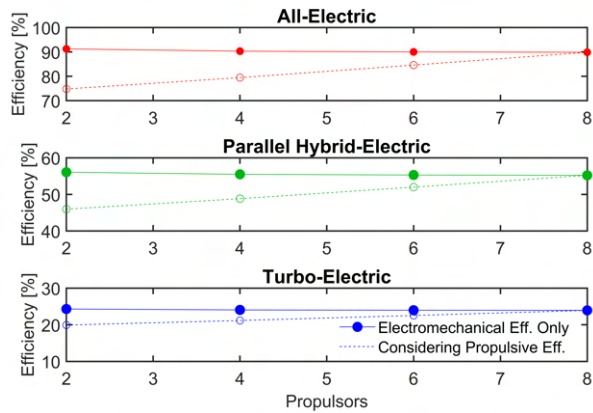
Figure 2.11: Distributed electric propulsion (DEP) effects on total system efficiency. When only the electromechanical efficiency is considered, losses increase with the number of propulsors due to the decrease in component efficiency as the power rating decreases. If the benefits of DEP are also considered, the overall system efficiency increases with the number of propulsors.

31

2.2.5 Circuit Protection

Circuit breakers can be mechanical or solid state devices. Mechanical breakers (vacuum, SF6, air chute) are conventionally designed for AC applications. In order to use them in DC systems, an artificial current zero-crossing is achieved through passive and active resonant circuits. Such breakers feature a low contact resistance, and can be designed to withstand high voltage, but have large fault clearing times, of the order of milliseconds, and a large number of moving components. In contrast solid state breakers, based on thyristors, IGBTs, etc. have operation times of the order of micro and nano seconds [69]. One limitation is the high on-state loss, which can be mitigated by the use of wide band gap devices. The available current and voltage ratings are limited, necessitating, for high power applications, several devices to be connected in series, parallel or both, and their synchronous operation. This additional complexity may favor power system topologies with a large number of lower rated components.

2.3 Exhaustive Design Space Evaluation Process

The edges of a graph represent interconnections between the various components. A graph for an EAPS is directed to signify possible directions of power flow. Some nodes such as an auxiliary heating unit may only accept power, therefore its edges should only be directed toward and not from the node. These edges may be assigned

weights, examples include mass associated with the inclusion of a particular vertex, power flow capacity, or physical distance. Further descriptions of how power systems may be represented as graphs can be seen in [70], [66]. Connectivity in between the various graph vertices may be used for minimal path calculation as in this study to determine lowest mass or highest efficiency. Additional studies in the literature have used graph theory for reliability evaluation by utilizing minimum cut sets to determine power loss scenarios [71].

The optimization process begins with inputs from the system designer regarding the intended use of the aircraft and technology available. Vehicle goals such as desired fuel savings, power requirement at maximum lift, and flight profiles, which describe aircraft power output over time, may be initially introduced by the user and later used as constraints. In addition to these vehicle-level inputs, the user also must define component-level information for the framework to use. These attributes include specific power and energy, efficiency, and failure rates. These may be defined static values as described earlier, or by ranges depending on the availability of resources to the aircraft designer. Introduction of ranges for component attributes also enables the use of sensitivity analysis to determine which components and attributes have the largest influence on performance metrics. In this study, a survey of various aircraft components was conducted to obtain values for efficiency and specific power as a function of power (Fig. 2.3 and Fig. 2.4). To further the accuracy of this model,

additional power system components such as gearboxes can be modeled, as seen in [72].

Once the components under consideration and the desired ranges are defined, a graph is constructed to represent many candidate designs, as seen in Fig. 2.7. An iterative process is established for the addition of commonly seen power flow paths into the graph to avoid excessive manual entries by the user. One example of a common path starts from a jet engine as a generation source, which converts mechanical energy to electrical through an AC generator, from this point the power can be rectified with a AC/DC converter, then this power can be used to drive an AC. As an example, the conceptual design for a 500kW aircraft will now be demonstrated. The system graph is iteratively created using components with varying power ratings, those labeled "large" represent a full power rating of 500kW, those with no indicator possess power of half the rated value, and those with "small" indicate a quarter of the power rating.

From the full graph, thousands of architectures are extracted which meet the power and energy requirements input by the user, such as those seen in Fig 2.8. To perform this extraction process, node are classified into power delivery (PD), energy source (ES), and power conversion groups. Jet engines are treated as both ES and PD nodes since fuel storage is included in the node characteristics. All possible permutations of ES and PD nodes are then calculated and stored into matrices, as illustrated in Fig. 2.9. The framework then iterates through the matrices to remove any permutations

whose total power and energy capacity do not meet the requirements imposed by the designer, which may be described as the following equation:

$$P_{req} = \sum_{i=1}^{n_{EM}} P_{EM,i} + \sum_{i=1}^{n_{JE}} (P_{JE,i} - P_{L,i}),$$

$$E_{req} = \sum_{i=1}^{n_{BAT}} E_{BAT,i} + \sum_{i=1}^{n_{JE}} E_{JE,i}, \tag{2.5}$$

where P_{req} is the maximum power and energy required for the aircraft's mission, P_{EM}, E_{EM}, P_{JE}, E_{JE} and E_{BAT} are the rated power and energy of the electric motors, jet engines, and batteries, P_g is the generated electrical power from a jet engine's turbines and n_{EM}, n_{JE}, n_{BAT} are the number of components in the design candidate. Subgraphs are then formed by using the previously defined ES and PD nodes in combination with minimum path algorithms to add edges and power conversion nodes. Additionally, the algorithm ensures the following power flow constraints between one a parent and daughter node(s):

$$P_s = -\sum_{i=1}^{n_l} P_l; \quad P_s < 0; \quad P_l > 0, \tag{2.6}$$

using the convention of supplied power being noted as negative and absorbed power as positive, where P_s is a parent node and P_l is a daughter node.

These architectures that are extracted include the extreme cases of all-electric and turbo-electric, which offer the most efficient and lightest designs respectively, and also series hybrid and parallel hybrid-electric aircraft power systems, which offer best case compromises. Design D1 is an purely electric topology with a battery rated

for 500kW and two 250kW motors and associate drives. Design D2 is a series hybrid with a 500kW jet turbine powering a similarly rated generator, rectifier, and battery, which then supplies two 250kW motors and drives. Designs D3 and D4 are parallel hybrids with a 250kW jet engine supplying a generator, rectifier, and battery of the same rating. D3 and D4 differ in the amount of energy stored in the battery and fuel tank, where D3 uses 50 percent of each and D4 uses 80 percent stored in the engine and 20 percent from the battery. Designs D5 and D6 are turboelectric systems with no electrical energy storage, both utilizing a 500kW engine and generator. D5 is a more distributed approach, which may prove more reliable and exhibit increased aerodynamic efficiency with four 125kW rectifier, inverter, motor combinations. D6, in contrast, has a single 500kW rectifier with two 250kW inverters and motors.

2.4   Discussion of Example Studies

A collection of valid subgraphs was constructed using the optimization approach discussed. Once obtained, post-processing may be done to evaluate the performance characteristics of each subgraph representing the aircraft power system topologies. In this study, two example studies were conducted to assess architecture performance on the basis of mass, efficiency and survivability. To further validate the design candidates produced by the framework, multi-physics co-simulation of the architecture may be conducted, as seen in [73].

2.4.1   Evaluation of Mass and Efficiency

The total power system mass may be calculated as the sum of all individual components masses and any energy storage. Nodes that represent loads or power conversion devices derive their mass from the node's rating and the associated specific power. The mass for those nodes which represent Lithium-ion batteries, is calculated using specific energy.

A special case is introduced for jet engine nodes, which represent both the engine and fuel storage. Total ICE node mass is calculated as the sum of engine mass, based on specific power, and mass of the required fuel. The mass of fuel used by an ICE per energy output is known as specific fuel consumption (SFC). Based on the survey conducted in Section II A, a second order polynomial fitting has been used to estimate a turbine's SFC as a function of power rating:

$$C_{ICE} = 2.14 * 10^{-8} P_{ICE} - 1.27 * 10^{-4} P_{ICE} + 0.42, \qquad (2.7)$$

where C_{ICE} is SFC in kg/kWh. To determine the required energy, a mission profile was used, which defines power consumption of the aircraft over time.

Another very important performance metric that is of interest to an aircraft designer is the overall system efficiency, which directly effects fuel consumption. Furthermore, the power losses determine the sizing for the thermal management and cooling. Recent studies have shown that distributed propulsion with multiple propellers and their associated electric machines may provide a higher aerodynamic efficiency [74].

Based on this reference, in a 250 PAX twin-jet, changing the number of engines from two to eight may increase the propulsive efficiency from 80 to 86 percent [75]. Although aerodynamic efficiency is expected to increase by means of boundary layer ingestion, as discussed in a number of references [74, 75], there isn't a clear analytical relationship established yet. In our current study, for the purpose of simplified exemplification, it has been assumed that an increase in efficiency from 80 to 86 percent occurs linearly as number of propulsors increases from two to eight.

$$\eta_{sys} = \frac{E(\eta_{comb}(1 - \zeta)) + (\eta_{elec}\zeta))\eta_{aero}}{E},$$ (2.8)

where η_{comb} represents the efficiency of a path from the combustion engine source to a motor load, η_{elec} represents the efficiency of a path stemming from battery energy storage, ζ is the degree of electrical energy storage, being a value from zero to one and η_{aero} is the aerodynamic efficiency. For a fully turbo-electric architecture, ζ will be equal to zero, as all the energy used for flight is stored in the jet fuel. It is assumed that the battery is charged independently of the engine.

This framework example study is conducted for a 500kW peak power electric aircraft. The total system efficiency versus EAPS mass was calculated using multiple values of ζ and both, with and without, the propulsive efficiency considered. The results, shown in Fig. 2.10, indicate that higher efficiency is achieved at the cost of mass in systems with battery energy storage, which is in line with expectations, and therefore confirms the applicability of the proposed approach.

In the case where assumed benefits of distributed electric propulsion (DEP) are included in the overall system efficiency calculation, topologies that use smaller, more distributed approaches may have fewer losses (Fig. 2.11). The distributed architectures result in an increase in mass, due to the decrease in power density as power rating decreases. The effects of DEP are achieved by the number of propulsors, and the incurred mass may be minimized by using architectures with the largest power rating and fewest number of power system components that posses more propulsors.

In many cases, it may be desirable to include multiple redundant paths for power flow, so that the overall system reliability may be increased. In power systems, this is done through the addition of multiple redundant conductors between feeders and controlling the connections through a combination of breakers and relays. Each of these add mass to the EAPS, and therefore must be accounted for. A constant mass penalty for interconnection edges is included in the model to better represent effect of conductors and interfacing hardware such as circuit breakers. To further improve accuracy of this model, a designer may include geometry of an aircraft, voltage and current ratings to obtain exact conductor and interconnect specifications.

Two forms of energy storage are considered in this study, electrical and chemical. When jet fuel is burned, this exhibits a mass variability throughout a flight profile. In the case of a hybrid aircraft utilizing jet fuel or fuel cell technology, total aircraft mass decreases as it progresses throughout its flight. This variability may be significant in
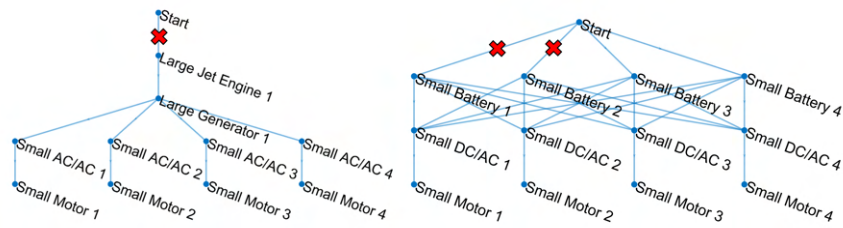
Figure 2.12: Illustration of topology survivability for designs considered in the optimization. Red markers on the graphs indicate minimum number of failures prior to flight power decreasing below 75 percent. Figure includes two designs selected from the pareto front when considering mass versus losses.
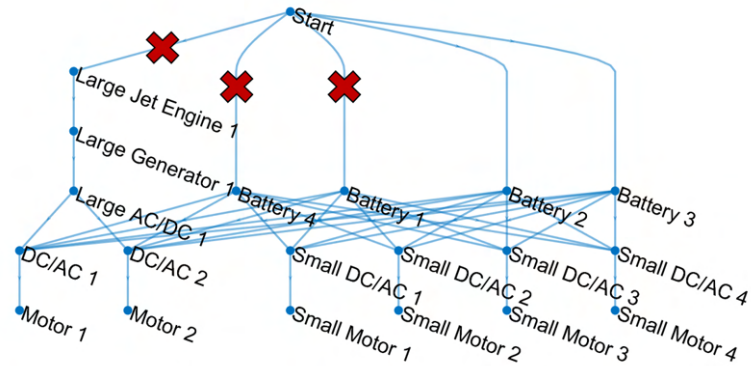
Figure 2.13: Electric aircraft power system topology that demonstrates N-3 survivability. While assurance of flight safety is increased by the addition of multiple redundant connections and components, overall system mass increases accordingly.

certain cases and is therefore included in this study. As the mass decreases, power requirements for various flight conditions will decrease as well. This is reflected in the total energy used calculations and output performance characteristics of the EAPS architecture.

2.4.2 Design Candidate Survivability

Power system architectures may also be evaluated based upon their survivability, meaning how well the system can perform if components go offline. In this chapter, survivability was scored using a tiered method, based on how many components may fail before thrust production capability falls below 75 percent of the nominal rated power of the case study.

A set of pareto front designs from the mass versus efficiency example discussed in the previous section was extracted and evaluated for their survivability (Fig. 2.12). Topologies which have a higher survivability index often exhibit greater mass, due to redundant components and connections. For example, a hybrid-electric architecture with N-3 survivability may be achieved through the addition of many redundant feeders (Fig. 2.13).

Turbo-electric topologies with fewer system components may perform best when considering metrics such as overall power system mass and efficiency, as discussed in the previous section. However, topologies that incorporate either a distributed approach through the implementation of many smaller energy storage and propulsive units or many redundant connections tend to exhibit higher survivability.

The proposed framework may be expanded to analyze EAPS reliability using minimal cut sets to determine, for each node, the minimum series of events which need to occur before the node is inoperative. This information can then be converted
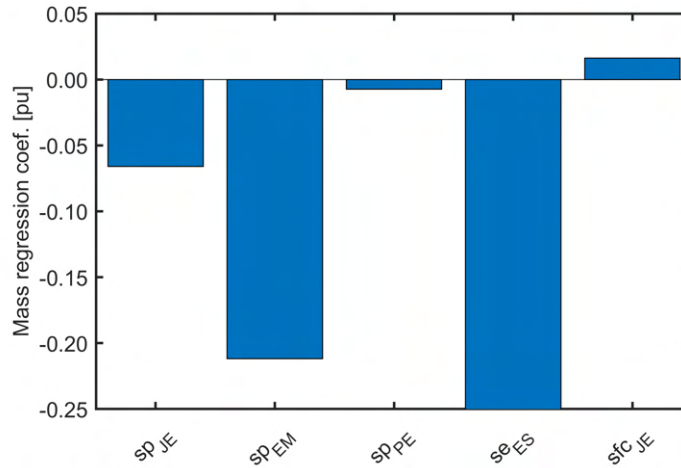
Figure 2.14: The regression coefficients in per unit associated with total power system mass resulting from numerical calculations for design candidate, D2. The regression coefficient for the specific energy for the electrical energy storage is -1.27.

into useful data such as the probability of failure. One challenge with the evaluation of power system reliability is obtaining accurate failure rates of components, which may be calculated using stress factors or specified by the manufacturer based on extensive laboratory testing. Additionally, estimating the interaction effects between components is non-trivial and must be carefully assessed, as seen in [71].

2.5   Sensitivity Analysis

As technology progresses, specific power, specific energy, and efficiency of the individual components used in the aircraft power system will advance accordingly. To evaluate the effect on performance metrics these advancements may have, a sensitivity study has been conducted for a selected topology design candidate, D2, which is a
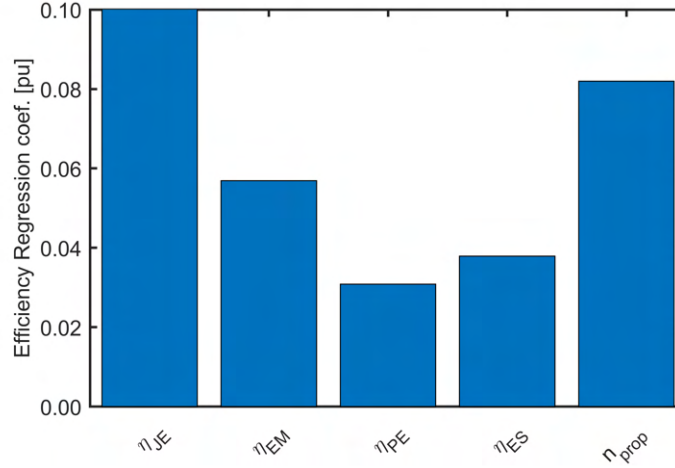
Figure 2.15: The regression coefficients in per unit associated with total power system efficiency resulting from numerical calculations for design candidate, D2. The regression coefficient for the efficiency of jet engines is 0.3.

hybrid architecture with half of the required energy for the flight mission originating from electrical storage. This was done by fitting a regression curve using a second order polynomial:

$$
Y = \beta_0 + \sum_{i=1}^{d_v} \beta_i X_{C_i} + \sum_{i=1}^{d_v} \beta_{ii} X_{Ci}^2 + \sum_{i=1}^{d_v} \sum_{j=i+1}^{d_v} \beta_{ij} X_{Ci} X_{Cj},
$$

$$
X_{Ci} = \frac{x_i - (x_{i,max} + x_{i,min})/2}{(x_{i,max} + x_{i,min})/2}; i = 1, 2, ..., d_v,
$$

(2.9)

where Y is a response parameter; β, the regression coefficient; d_v, the number of factors, x_i, the ith input factor; and X_{Ci}, the normalized (coded) value of the ith factor. Factors may be normalized as shown in (2.9). $X_{Ci} = 0$ represents the specified values of the factors, and β_0 is a representation of response parameter in this reference situation. For each of the following sensitivity studies conducted, a single 500kW parallel hybrid topology with 50 percent electrical energy storage as seen in design

43

D3 was used. The factors and associated ranges of variation considered for the analysis were derived from that seen in the literature review conducted on the power system components shown in Table. 2.1.

When considering mass as a primary objective for a given design candidate, there are five factors that affect the total power system mass: jet engine specific power, electric machine specific power, power electronics specific power, electrical energy storage specific energy, and jet engine specific fuel consumption. The results of this sensitivity study show that within the currently available technology, the greatest reduction of mass can be achieved by utilizing the highest performance energy storage with respect to specific power, as seen in Fig. 2.14.

Alternatively, when the primary objective is system efficiency, the five factors that influence the output are efficiencies of the jet engines, electric machines, power electronics, and energy storage and number of propulsors. This study shows that, given the current ranges of available component efficiencies, jet engines may have the greatest contribution to the total system losses (Fig. 2.15).

2.6 Summary

Electric aircraft designs today show large variations in power system types as well as number of components used. This chapter presents developments toward an optimization approach for aircraft power systems which incorporate electric propulsion.

Table 2.1: EAPS component variables. Values stated reflect those seen in the survey conducted in Figs. 3-6.

Component Factors		Ref. values (min, max)
se_{ES}	Energy storage specific energy [kWh/kg]	0.07, 0.2
sp_{JE}	Jet engine specific power [kW/kg]	1, 11
sfc_{JE}	Jet engine specific fuel consumption [kg/kWh]	0.186, 0.495
sp_{EM}	Electric machine specific power [kW/kg]	1, 16
sp_{PE}	Power electronic specific power [kW/kg]	11, 34
η_{JE}	Jet engine eff. [%]	16.23, 43.20
η_{EM}	Electric machine eff. [%]	93, 98
η_{EM}	Power electronics eff. [%]	96, 99
η_{EM}	Energy storage eff. [%]	95, 99
n_{prop}	Number of propulsors	2, 8

The proposed approach is capable of evaluating thousands of design candidates based on performance metrics such as mass, efficiency, and survivability.

This chapter includes a study for an aircraft designed for a rated power of 500kW, intended for short-haul missions, such as those seen in commercial aviation. The case study power system candidate pool includes both conventional jet and electrical propulsion means, and steps of granularity in between degrees of electrical energy storage. Example outcomes include comparative evaluation of potential power system architectures with respect to mass, efficiency and survivability.

The results of this study show that aircraft with greater means of electrical energy storage exhibit higher efficiency, while those with more chemical energy storage and fewer components perform better when considering mass. Additionally, when the efficiency benefits of distributed propulsion was considered, designs with more, smaller propulsors may have a greater overall efficiency and prove to be more survivable, at the cost of an incurred mass. The framework developed provides a tool for system designers to evaluate tradeoffs between various EAPS topology candidates. While it may be apparent that purely electric designs are most efficient and turbo-electric architectures have the lowest mass, what is often needed is a trade-off, based on mission goals. It was demonstrated that the proposed automated optimization process is able to identify such best-case compromises represented by series and parallel hybrid architectures with various degrees of electrical energy storage and topology layouts,

including multiple propulsors.

Chapter 3

Multi-physics Co-simulations of Electric Aircraft Power System and Vehicle Dynamics

3.1 Introduction and Problem Formulation

This chapter discusses the multi-physics modeling of an electric aircraft with distributed electric propulsion. Mathematical models for the aircraft body, propellers, propulsive motors, power electronics inverters, and batteries are developed. Two types of models are proposed for the power electronics inverters and electric machines, namely, average models which allow study of the aircraft performance under a specified mission profile, and detailed switching models used for transient examination. A new simulation framework was developed to allow communication between these two types of models so that losses and thermal stresses in the power electronics converters can be estimated especially during takeoff, landing, and other extreme

conditions. Case studies are presented for an example aircraft based on the ratings and configuration of X-57 Maxwell, NASA's first all-electric distributed electric propulsion electric aircraft, which employs fourteen propellers driven by synchronous electric motors.

In the past decade, there have been several all-electric demonstrators and concept aircraft to support the progress toward electrification of flight. This chapter reports the development of a simulation framework which can be used to examine the power system and flight dynamics associated with a wide array of electric and hybrid aircraft topologies. Many topological variations have emerged with respect to airplanes incorporating electric propulsion, both in the literature and flight proven vehicles. Electric aircraft may be categorized as turbo-electric, hybrid-electric or all-electric. Turbo-electric powertrains use traditional internal combustion engines (ICE) with coupled generators feeding electric machines and utilize minimal energy storage, such as NASA's N3-X [76]. Hybrid-electric concepts incorporate both ICE and electric machines for propulsion and include a significant portion of energy storage. One example hybrid aircraft is the PEGASUS concept shown in [77]. In this study, an all-electric aircraft employing a distributed propulsion system with ratings similar to NASA's X-57 Maxwell [36] is used as a case study (Fig. 3.1). Results are presented for a 240 kW aircraft which produces thrust through 14 three-phase synchronous motors, two of which are positioned at the wing tips, with the remaining distributed

along the wing. These electric machines are driven by three-phase, two level inverters utilizing silicon carbide devices for high efficiency and reduced harmonic distortion. Energy storage onboard the modeled vehicle consists of Lithium-ion batteries which supply the described powertrain. Physics based models are developed for different components including the aircraft, propellers, batteries, power electronics equipment and propulsive motors. There exist many instances of co-simulation platforms being used to evaluate hybrid and electric vehicles in the literature. Work done in this area vastly covers ground transportation such as hybrid and electric cars [78], [79], [80]. However, fewer studies exist for the multiphysics domain analysis of electric air transportation.

The simulation framework described in this chapter includes two types of models owing to the widely different time constants of the electrical and mechanical systems, average power converter and propulsion motor models, suitable for the study of aircraft dynamics and performance over a flight profile and transient switching models, useful for determining the stresses associated with the power electronics equipment under takeoff, landing, and other similar conditions (Fig. 3.2). This framework has been presented with a case study of NASA's X-57 Maxwell and, in principal, can be used for detailed efficiency analysis, sizing of the thermal management system, and to study influence of switching harmonics at the system level of similar aircraft.

3.2 Modeling of Aircraft Dynamics

The dynamics associated with the body of the aircraft are simulated over a given flight profile alongside the average model of the motor and battery energy storage system. A pilot subsystem send commands to the motor model as well as flight actuation system to control air speed and altitude. The average electric machine model previously described takes in a speed command from the pilot and is coupled to the propeller model through shaft speed and associated load torque. The energy storage model uses the product of these two outputs to calculate the state of charge (SoC) of the battery throughout the mission. In parallel, the aerodynamic modeling receives the value of generated thrust from the propeller in addition to external forces associated with the environment and calculates the vehicle's motion. Data from this subsystem is then sensed and fed back to the pilot (Fig. 3.3).

Motor operating speed is dependent on the motion of the aircraft at the current state and the desired performance. As the primary focus of this study is to examine electrical performance, the vehicle geometry and aerodynamic modeling is based off of the work conducted in [37]. Considering only the x and z axes, the equations of motion for the aircraft are as follows:

$$
\begin{aligned}
A_{xb} &= \frac{du}{dt} = \frac{F_x}{m} - qw - gsin(\theta); \\
A_{zb} &= \frac{dw}{dt} = \frac{F_z}{m} + qu + gcos(\theta),
\end{aligned}
\tag{3.1}
$$

where F_x represents the total force in the x-axis in kg, m is the vehicle mass in kg, q is

the pitch angular rate, w is the z-axis velocity, g is the acceleration due to gravity, and θ is the pitch attitude. The force due to gravity contributes to the positive z direction as well as in the x direction. The force acting on the vehicle in the positive x-axis is the propulsive thrust. The propulsive thrust is derived from the electric motor and propeller. The thrust is a function of the thrust coefficient, C_T, air density, ρ, propeller diameter, D, and rotational speed of the motor shaft, n:

$$F_{thrust} = C_T \rho D^4 n^2,$$ (3.2)

where F_{thrust} is thrust in newtons, C_T is the coefficient of thrust, ρ is the air density, D is the propeller diameter in meters, and n is the propeller speed in revolutions per second. where F_z represents the total force is the z-axis and u is the vehicle velocity in the x-axis. The change in pitch angular rate is a function of the moments and the inertia:

$$\frac{dq}{dt} = \frac{M}{I_{yy}}.$$ (3.3)

3.3   Modeling of Electric Propulsion System

The propulsive force generated by the propeller is supplied from an electrical power system onboard the aircraft. The propellers are attached to twelve 10-kW and two 50-kW synchronous machines, supplied by means of three-phase, two-level inverters. These drives utilize advanced SiC power switches, capable of higher switching frequencies than traditional silicon devices, enabling a light-weight aircraft due to the
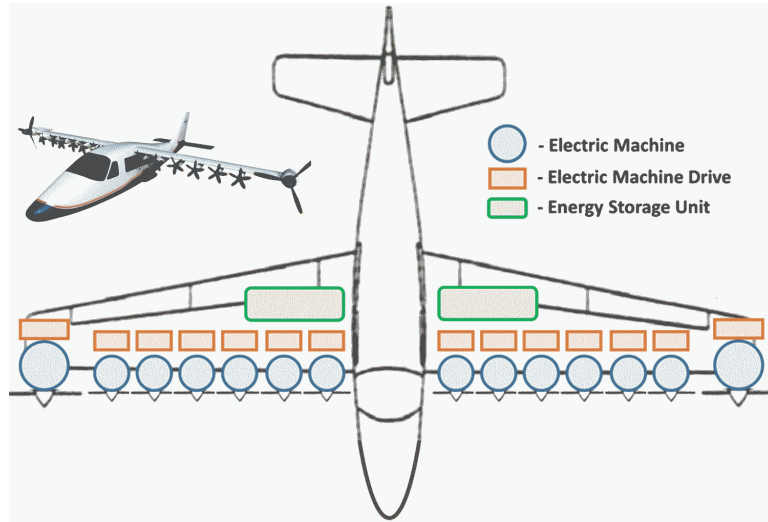
Figure 3.1: The X-57 Maxwell, NASA's first all-electric distributed electric propulsion electric aircraft. The new modeling software framework developed in this chapter considers the aircraft power system shown with a combined total rated power of approximately 250-kW [36], [37].

reduced mass of electrical filtering. The flight profile studied in this chapter covers a wide array of operating conditions including those where the power system is driven to the extremes that would be required during a typical flight plan. The combined powertrain is simulated at peak power demand during periods of takeoff when rapid acceleration of motor speed is required. Additionally, the inclusion of an emergency flight extension due to an unavailable landing runway allows endurance evaluation of the energy storage system.

When simulating aircraft dynamics, an average model is used for evaluation of the electric motors, which is coupled to a propeller subsystem through shaft speed and load torque (Fig. 3.4). The synchronous machines are driven through vector control,
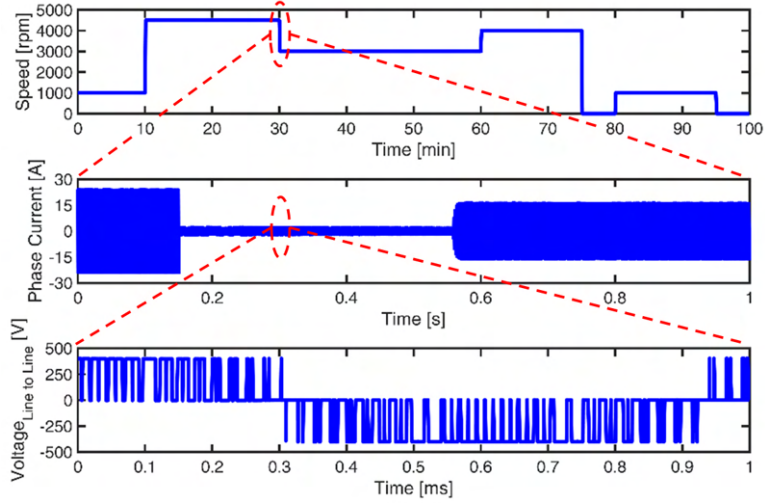
Figure 3.2: Illustration of the large variations in timescales between important transitions associated with each subsystem. Flight profiles may require changes in altitude over a period of minutes, leading to the need of simulating motor state transitions which occur over fractions of seconds. Additionally, the power electronics that drive the propulsion motors have associated time constants in the sub-millisecond range.

using a dq reference frame (Fig. 3.5). The load torque as seen by the propeller is derived from the pilot input speed command. The acceleration of the propeller shaft is governed by the following equations:

$$T_M - T_L = J\frac{d\omega}{dt},\qquad(3.4)$$

where T_M is the electromagnetic torque, T_L is the load torque produced by the propeller, J is the moment of inertia of the propeller, ω is the motor's angular speed.

The load torque of the propulsion motor is that required by the propeller at a given speed. This torque can be obtained through multiplication of the output thrust and the diameter of the propeller as well as an additional torque coefficient, C_Q:

$$Q = T_L = C_Q \rho D^5 n^2.\qquad(3.5)$$

54
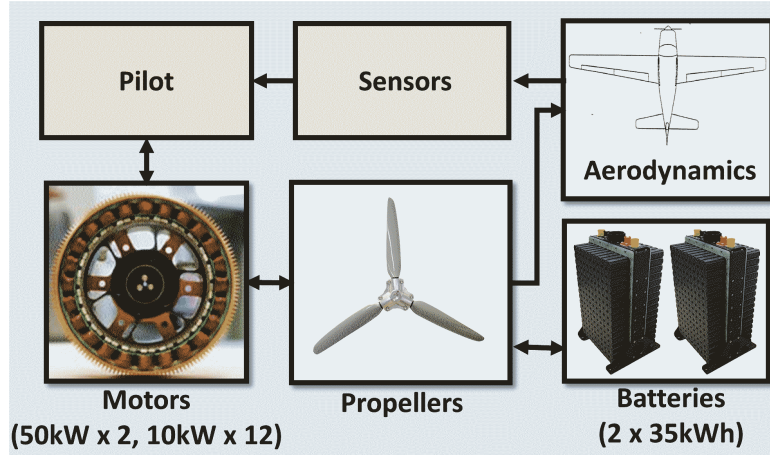
Figure 3.3: Electric power system and body dynamics simulation overview. The pilot controls the motors speed based on desired aircraft velocity and feedback sensor data. The motor model communicates with the propeller to obtain load torque and thrust, which used for aerodynamic modeling. The power used is employed by the battery model to determine state of charge (SoC).

The values for coefficients of thrust and torque are commonly extracted from experimental data of the propeller. These coefficients are strong functions of the advance ratio, which is defined as the ratio of the true air speed and the propeller tip speed [81]. Preliminary modeling treats these coefficients as constant throughout the mission. Further analysis of propeller characteristic could include dynamic modeling of the torque and thrust coefficients through look-up tables based on interpolated manufacturer data.

The electromagnetic torque produced by the motor is a function of p, λ_m, and i_q:

$$T_M = \frac{3p}{2}\lambda_m i_q, \tag{3.6}$$

55
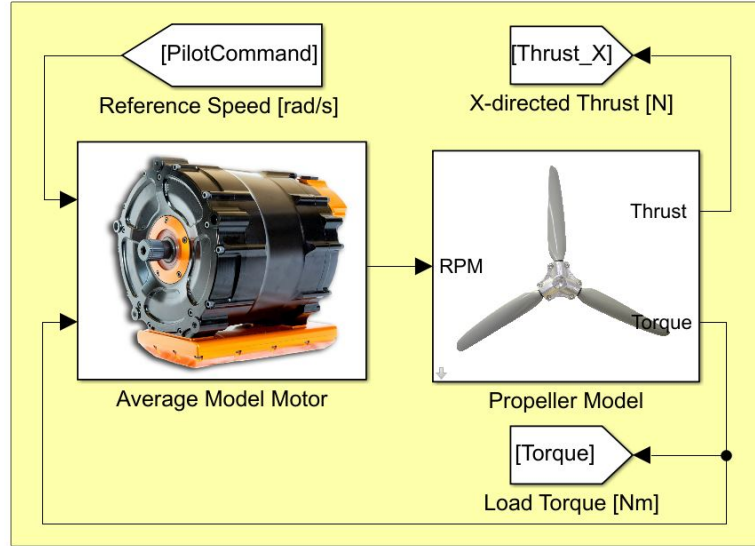
Figure 3.4: System level view of motor and propeller models. Motor speed is used as a control variable, commanded from the pilot. Load torque and thrust are modeled as a function of the motor speed and characteristics of the propeller. With these values, the motor model calculates instantaneous voltages and currents to achieve the demanded performance.

where p is the number of poles, i_q is the q-axis current, and λ_m is the magnetic flux linkage. In a dq reference frame the demanded currents, i_d^* and i_q^* are defined by:

$$i_q^* = \left(K_p + \frac{K_i}{s}\right)\left(\omega^* - \omega\right); \quad i_d^* = 0, \tag{3.7}$$

where K_p is the proportional gain, and K_i is the integral gain. The d-axis current command is kept at zero to ensure operation at maximum torque per ampere conditions. The output reference currents are then compared to the currents of the machine
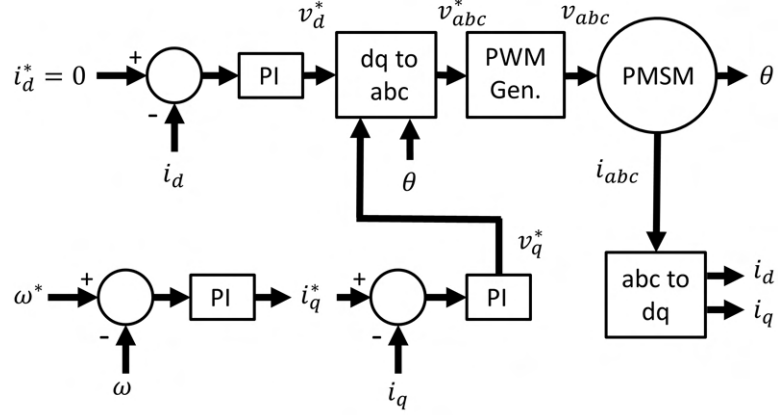
Figure 3.5: Control strategy for the synchronous machines providing propulsive force for the aircraft. The pilot provides the input desired speed reference and the PWM gating signals are generated for the three-phase inverter driving the machines.

in an additional control loop to derive the following command dq voltages:

$$
\begin{aligned}
v_q^* &= \left(K_{pq} + \frac{K_{iq}}{s} \right) \left(i_q^* - i_q \right), \\
v_d^* &= \left(K_{pd} + \frac{K_{id}}{s} \right) \left(i_d^* - i_d \right).
\end{aligned}
\tag{3.8}
$$

In the model which examines the entire aircraft system, the dynamics associated with the inverter switching characteristics are neglected. It is considered that the load torque is derived from the propeller model and the ideal voltages are applied to the motor, which is calculated using the equation below:

$$
v_q^* = v_q = Ri_q + L_q \frac{di_q}{dt} + p\omega L_d i_d + p\omega \lambda_m,
\tag{3.9}
$$

$$
v_d^* = v_d = Ri_d + L_d \frac{di_d}{dt} + p\omega L_q i_q.
\tag{3.10}
$$

However, for periods of transition between operating speeds, the switching level model is used to evaluate maximum required rating of components.
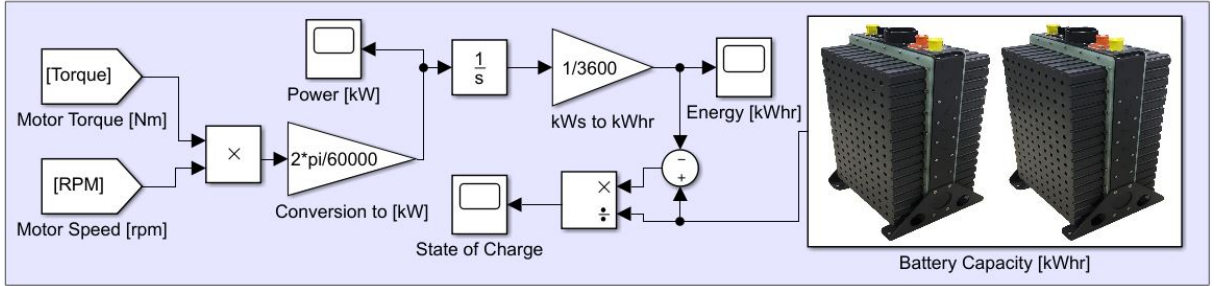
Figure 3.6: Simulation subsystem developed for estimating the state of charge of the battery (BESS). Inputs include battery capacity, motor torque and speed. The instantaneous power demand is calculated and integrated over time to derive the energy used over the flight cycle.

This model also includes measures to avoid the motor operating above its rated conditions. The output speed of the motor is limited by the available DC bus voltage (3.11). The speed will be curtailed in the case that the demand speed requires a voltage magnitude exceeding the conditions stated below:

$$\sqrt{V_d^2 + V_q^2} < \frac{V_{DC}}{2}. \tag{3.11}$$

Without the addition of supplemental power electronics, V_{DC} is the voltage of the battery energy storage system (BESS). This system constraint may be relaxed by incorporating a boost stage prior to the inverter such as seen in [82].

The aircraft is supplied by a Lithium-ion BESS and supplies the propulsion system described. The usable battery capacity is considered as 47-kWh, which is similar to that seen in the X-57 design [36]. The BESS SoC modeling is determined by integration of the combined power usage of all motors over the simulated flight cycle (Fig. 3.6).

58
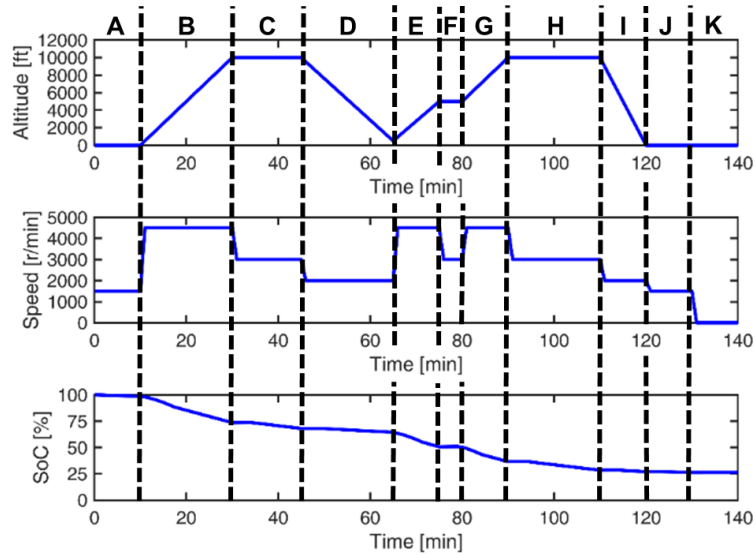
Figure 3.7: Example of flight profile comprising a typical mission followed by an emergency rerouting. Eleven distinct intervals are identified through letters. The graphs display the altitude, the speed of the electric motors, and the battery SoC.

3.4 Simulation Results and Discussion

The flight cycle imposed on the aircraft represents a case in which the airplane flies a typical flight path, then an emergency extension in order to model the system during extreme conditions. It is assumed that the aircraft has an initial position on the taxiway of an airport, at which point the pilot taxis to the runway and begins takeoff at t=10min. The aircraft is then commanded to climb to an altitude of 10,000 feet. Upon reaching the cruise level, the vehicle will maintain its altitude until t=45min. At this point, the airplane will start its descent for landing. The condition at t=65min simulates an instance where the destination runway is unsuitable for landing, therefore the pilot must climb to a low altitude cruise and hold until a new
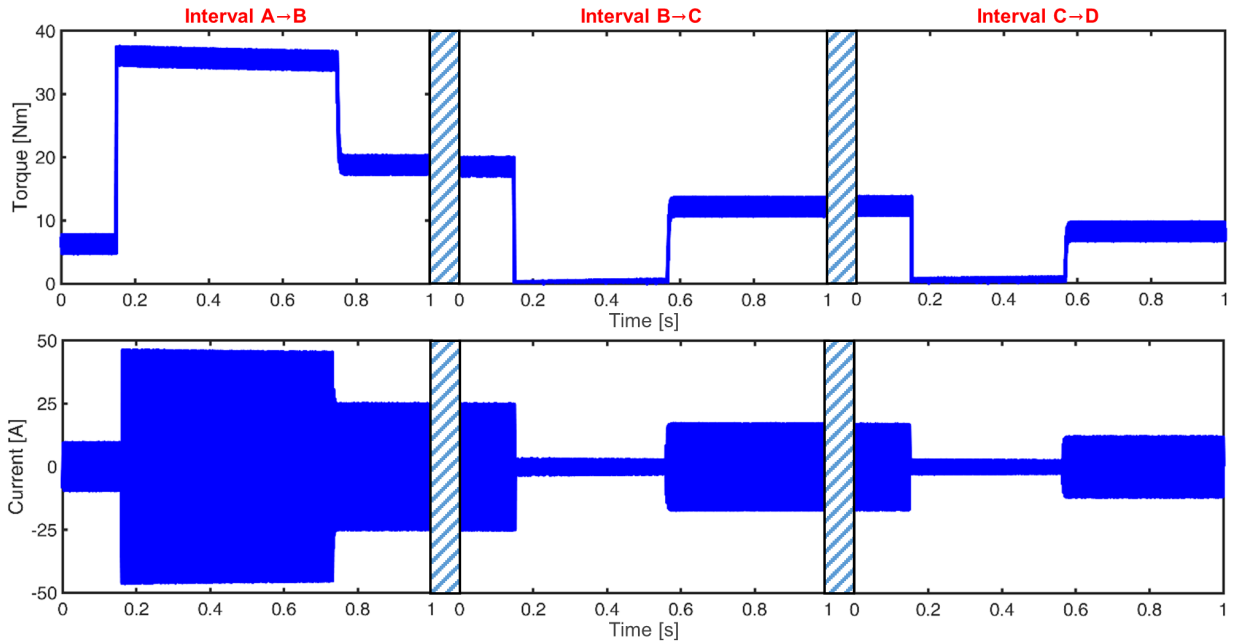
Figure 3.8: Electromagnetic torque produced by a single electric machine during flight phase transitions. Results from the long time constant simulation are used to evaluate the effects of the system's high frequency power electronic switching during transient periods. Speed transient conditions shown are from 1500 to 4500 r/min (left), 4500 to 3000 r/min (middle), and 3000 to 2000 r/min (right).

landing location is confirmed. The aircraft then follows a climb, cruise, descent and landing pattern to the secondary destination airport from t=80min to t=120min. The vehicle is then taxied from the runway and motors are stopped at 130 minutes (Fig. 3.7). The aircraft dynamics with associated average models for electric propulsion were simulated with the described flight profile. The SoC was observed throughout the mission and normalized with respect to the 47-kWh usable capacity of the BESS.

Transitions between each period of the trajectory were simulated using the detailed model which considers the switching dynamics of the power electronic converters.

Loading of the synchronous machines in this simulation were obtained from the model including propeller dynamics. During these periods of transition, the torque produced by the motors is varied to maintain the commanded shaft speed. Results shown include the electromagnetic torque and phase currents of a single three-phase, 10-kW propulsive synchronous machine during the first four periods of flight (Fig. 3.8). It can be observed from the flight cycle that the maximum loading period of the power system is during the transition from periods such as A to B, when the commanded shaft speed is at a maximum. These events occur when the aircraft is beginning its ramp to full power for takeoff or during a climb. Results such as the three-phase currents of a single machine from the detailed model may be used for system sizing during the initial system design stage. Applications include electric machine and power electronic converter component selection, thermal management system sizing, and potential filtering specifications required to meet signal noise goals. Additionally, these waveforms may be used to identify maximum discharge rate required for the BESS.

3.5   Summary

The newly developed comprehensive simulation framework for electric and hybrid aircrafts, which is described in the chapter, has the main advantage of providing a unified approach for system analysis on greatly different timescales. For simulations

of long-duration complete flight missions, aircraft aero-dynamic models are employed in combination with average models of electric machines and power electronic converters and a proposed method for calculating the SoC of the battery, which enables the optimal sizing of the electric energy storage system. For simulations of the transitions between different steady-state intervals of the flight profile, a high resolution model of the power electronics controls was implemented to simulate the high frequency switching and the associated effects on current and voltages, in order to enable the detailed design sizing, including maximum power rating, thermal management systems and filters. The simulation framework was exemplified on an aircraft with ratings reflective of NASA's first electric airplane, the X-57 Maxwell, which is equipped with a distributed electric propulsion power system.

Chapter 4

Extended Speed Range Operation of Drives with Low Inductance Machines

4.1 Introduction and Problem Formulation

Electric vehicle applications often employ permanent magnet synchronous machines (PMSM) because of their high efficiency and specific torque. These applications often require a wide constant power speed range (CPSR). In traditional PMSMs, operation in the constant power region may be achieved by the injection of a negative d-axis current, however, the range of speeds over which this is possible often tends to be small. The width of the CPSR is a strong function of the machine's d-axis inductance, and smaller values, typical of PMSMs with surface mounted permanent magnets, due to their large air-gap, often have very limited operation in this region. This issue is further exacerbated in coreless PM machines, which present a very small inductance due to the large electromagnetic airgap because of the absence of the core.

This chapter discusses different methods for constant power operation of low inductance machines, and more specifically, a multi-disc coreless axial flux permanent magnet (AFPM) synchronous machine. This motor includes two stators, with coils mounted on a non-magnetic supporting structure and three permanent magnet (PM) rotors and an exploded view is seen in Fig. 4.1. This traction motor is proposed to be employed in the University of Kentucky (UK) solar car, which is pictured in Fig. 4.2a [83]. The performance comparison of different techniques for constant power operation of low inductance machines is presented. In addition, two novel methods for achieving constant power operation, particularly applicable to coreless AFPM machines, namely current weakening and relative winding rotation are proposed.

The first method involves raising the dc bus voltage of the inverter with speed, using additional power electronics stages. The availability of wide band gap semiconductor devices with low switching loss, as well as the absence of core loss in coreless AFPM machines make such an approach feasible. The second method involves the dynamic relative rotation of the two stators in the coreless AFPM with operating speed. This reduces the flux linkage and thus, operation at very high speeds, theoretically infinite, using this technique can be achieved. Analytical equations and finite element analysis confirm the operation of this method.

The desired torque-speed characteristics in an electric vehicle application are shown in Fig. 4.2b. This figure shows that the torque must remain constant up
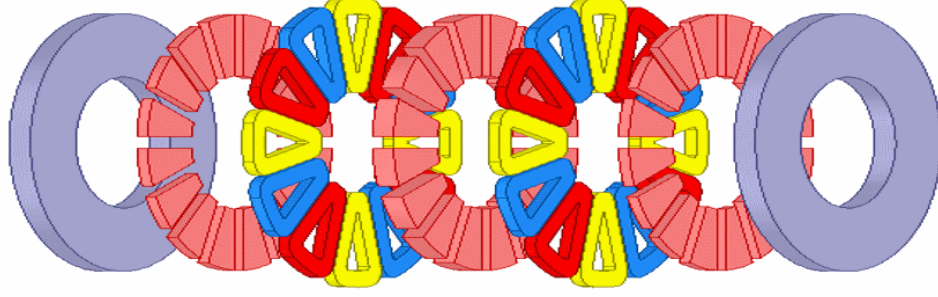
Figure 4.1: Exploded view of a coreless multi-disc axial flux permanent magnet machine with 2-stators and 3-rotors proposed to be used as a traction motor in the UK solar car. The stator includes coils placed in the airgap due to which the machine has a very low inductance.

to a base speed, i.e. the speed at which the machine's terminal voltage equals the maximum voltage from the inverter. Since constant power operation is desired at speeds exceeding the base value, in order to meet the dc bus voltage limitation of the inverter, the coil flux linkage must reduce with speed. The coil flux linkage is given as,

$$\lambda_{pm} = \frac{2}{\pi} k_{\omega 1} N_t k_{vg} \alpha_i B_{go} \tau_p \ell_{Fe} \ , \tag{4.1}$$

$$B_{go} = \frac{B_r}{\frac{\alpha_i}{k_\alpha} \frac{\tau_p}{k_b h_m} + \frac{2\mu_{mr} k_c k_{so} g_o}{k_h g_m}} \ , \tag{4.2}$$

where N_t is the number of turns per phase; k_{vg}, the ratio between amplitude of the fundamental wave and the average value of the air gap flux density; α_i, the pole-arc/pole-pitch ratio; B_{go}, the peak open-circuit air gap flux density; τ_p, the pole pitch; ℓ_{Fe}, the back iron length; k_α, the PM leakage coefficient; k_b, the number of PMs which provide polar flux; h_m, the PM height; μ_{mr}, the relative permeability

(a)
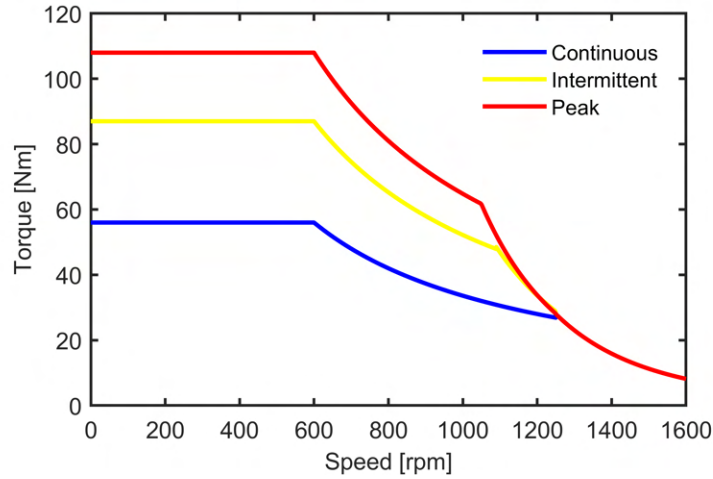
(b)

Figure 4.2: (a) Gato del Sol V of the University of Kentucky's Solar Car Team. (b) Desired torque-speed characteristics for the traction motor.

of the PM; k_c, Carter's coefficient; k_{so}, the d-axis saturation factor at open-circuit operation; g_o, the air gap thickness; k_h, the number of times the medium length flux line passes through the PMs, and g_m, the PM thickness [84].

In the surface mounted PMSMs, the saliency ratio is unity, and the inductance may be expressed approximately as,

$$L_d = L_q = \frac{2m\mu_o(k_{\omega_1}N_t)^2\tau_p\ell_{Fe}k_{ad}}{\pi^2 p k_c g_o} \ ,\tag{4.3}$$
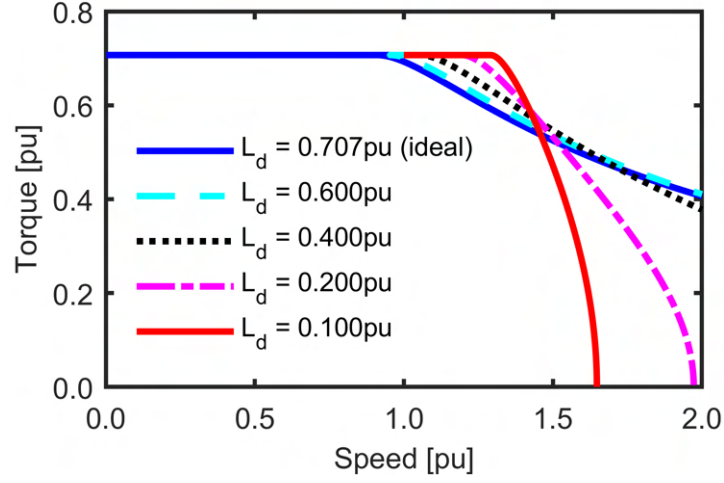
Figure 4.3: Torque speed characteristics of a permanent magnet synchronous machine with different values of the pu d-axis inductance. Smaller values, exhibited by the coreless AFPM machine, result in a very narrow constant power range, although a wide range is required for the application.

$$k_{ad} = \frac{k_c g_o}{k_c g_o + \frac{k_h g_m}{2\mu_{mr}}} \ , \tag{4.4}$$

where m is the number of phases, and p, the number of poles. The required terminal voltage to operate at a given angular velocity, ω, is given by

$$V = \omega \sqrt{(\lambda_{pm} + L_d I \cos \beta)^2 + (\xi L_d I \sin \beta)^2} \ , \tag{4.5}$$

where I is the motor current; β, the torque angle, and $\xi = L_q \ / \ L_d$, the saliency ratio.

The electromagnetic torque produced by the machine is given by

$$T = \frac{m}{2} p [\lambda_{pm} I \sin(\beta) - \frac{1}{2}(\xi - 1) L_d I^2 \sin(2\beta)] \ . \tag{4.6}$$

Since the machine is non-salient, only alignment torque is present. In a non-salient

67

(a)

Current Limit
Voltage Limit
X λ_{pm}/L_d
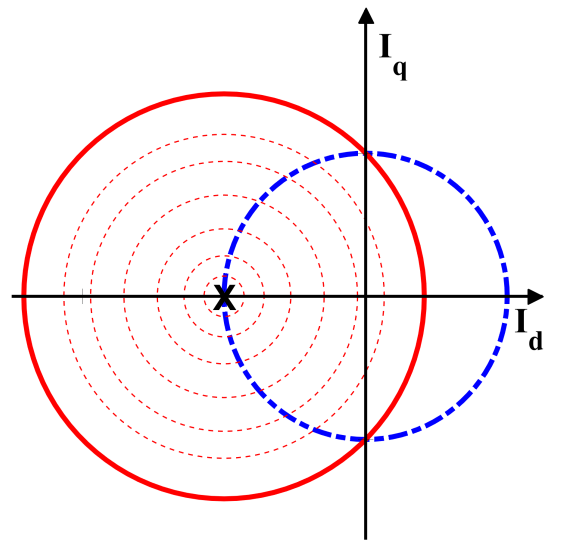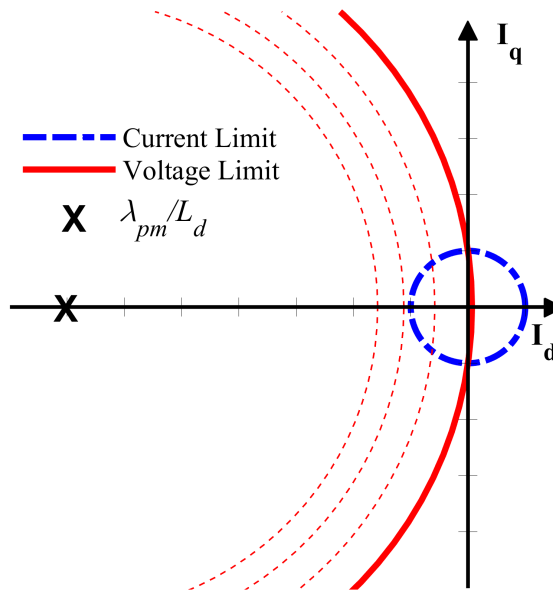
(b)

Figure 4.4: Motor drive operation range of two surface-PM machines, limited by voltage and current constraints. (a) A machine with a λ_{pm}/L_d ratio of 1. (b) A machine with a λ_{pm}/L_d ratio of 7.07. Operation is achievable in the regions encompassed by both circles. Dashed red lines indicate increasing speed.

PMSM, rotor reference frame oriented control is employed to decouple the currents into direct (d) and quadrature (q) axis components. From (4), as $\xi = 1$, maximum torque per ampere is obtained when the d-axis current is driven to zero, or β is maintained at 90 degrees. At higher speeds, a negative value of I_d can be used to reduce the terminal voltage, otherwise directly proportional to speed, as seen in (3). The value of I_d is increased such that the total rms phase current is constant, i.e.

$$I_d^2 + I_q^2 = I_s^2 \; , \tag{4.7}$$

where I_s is the phase current, at 1 pu This serves to reduce the torque, as it is directly proportional to I_q. The flux linkage reduces with increasing value of negative I_d (i.e. $90° < \beta < 180°$) such that the terminal voltage is constant.

The dependence of the width of the constant power region on the value of d-axis inductance is seen in Fig. 4.3. Lower values of pu inductance, as typical of the coreless AFPM machine lead to a very narrow constant power region. The analytically calculated torque-speed characteristics for different values of pu L_d are illustrated in Fig. 4.3. The torque-speed characteristics were calculated assuming an available terminal voltage of 1 pu in all machines. By setting a voltage constraint of 1 pu on (4.5), the voltage limited capability of a machine's drive can be defined as a function of speed, inductance, flux linkage, and current. The current limitation is expressed by (4.7). The limitations are illustrated in Fig. 4.4. Operation is achievable at any point within the intersection of the voltage and current limitation circles. The radius

of the voltage limitation circle is $V/\omega L_d$, and it is centered at $-\lambda_{pm}/L_d$. As the operating speed is increased, the radius reduces. The figure shows two machines, one with $L_d = 0.707$ pu, for ideal field weakening operation and the other with $L_d = 0.1$ pu, representative of a machine with ultra-low inductance, such as a coreless machine. The condition for ideal field weakening is

$$\lambda_{pm} = L_d I_s \; . \tag{4.8}$$

Since V = 1 pu, and $I_s = 1$ pu, and for a surface mounted PMSM, $L_d = L_q$, the value of λ_{pm} can be found by substituting these values in (5) to be 0.707 pu

It can be seen that for the lower inductance, the voltage limit circle has a much larger radius, and the center of the circle is shifted far from the origin due to the very small inductance. Thus, as speed is increased, the machine reaches the inoperable regions quickly and alternative methods are required to achieve operation at speeds higher than the rated speed.

4.2 Review of Existing Methods for Constant Power Operation

Operation at higher speeds for machines with a small inductance may be achieved by dynamic winding re-configuration. For instance, in one implementation, the windings can be connected in series for operation in the constant torque region of the
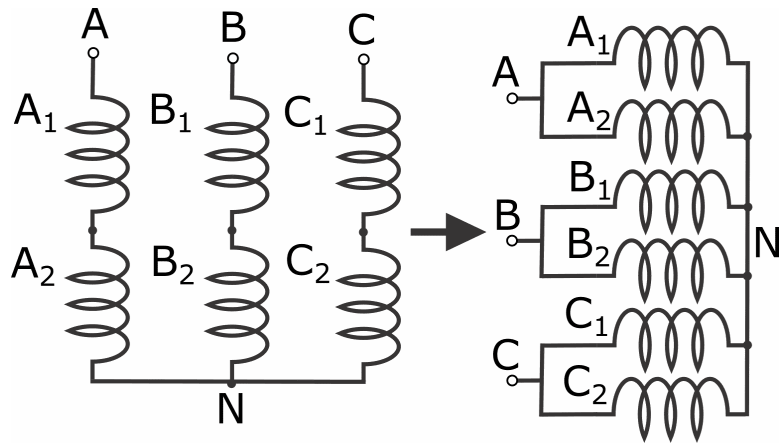
Figure 4.5: Schematic of winding reconfiguration. The series connection is employed at lower speeds, while at higher speeds, the coils are connected in parallel.
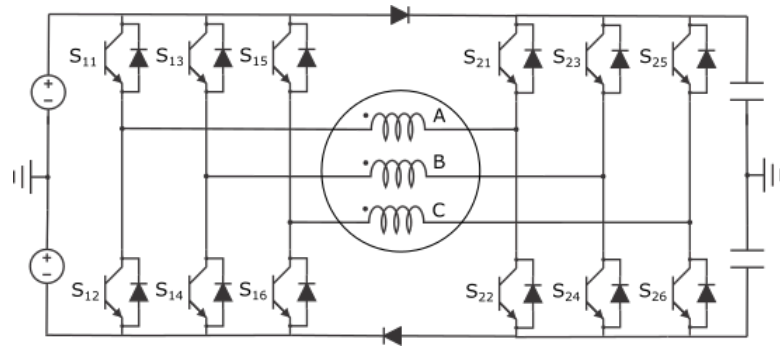
Figure 4.6: Schematic of a machine with open ended windings fed by two voltage source inverters.

torque-speed characteristics, and in parallel when constant power operation is desired (Fig. 4.5).

This technique requires each phase winding to be divided into two sections. During the shift in configuration from series to parallel, the current and voltage per winding are maintained constant [85]. Connection of the windings in parallel leads to a reduction in the number of turns, and therefore a smaller λ_{pm} and L_d, as indicated

71
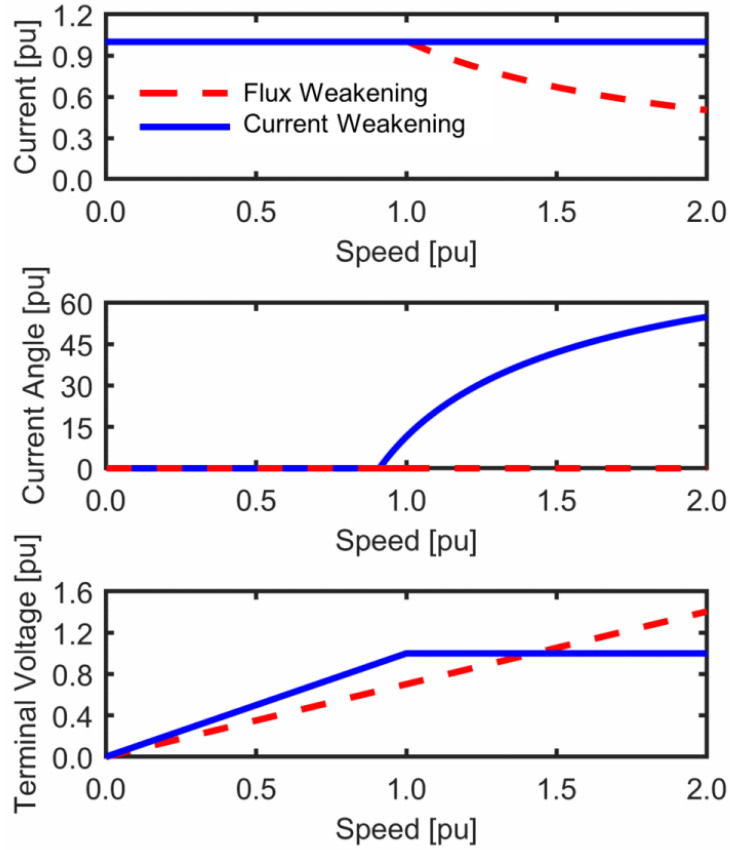
Figure 4.7: Current weakening technique and traditional field weakening approach in the constant power region.

by equations (1) and (2), and thus, higher speed can be achieved. This method requires no d-axis current to be injected, thus maximum torque per ampere (MTPA) can be maintained, as long as the maximum desired operating speed is twice the base speed. Actual implementation of this method could be achieved using back-to-back thyristors as suggested in [86].

Due to the fact that current would double when the winding configuration is

switched from series to parallel, this method does add an increase in required current and therefore, volt-ampere rating for the inverter. However, this increase in current rating may be justified, as traction motor inverters are often over-sized in order to meet the desired acceleration at low speed.

Another method for extending the speed range involves the addition of an external inductance in series with the machine, which leads to a reduction in required terminal voltage at higher speed as seen in equation (5). This method extends the field weakening range of the machine. Operating speeds past the rated value can be obtained through the tradition means of negative d-axis current injection. Since all of the current is not maintained in the q-axis in this method, MTPA is not achieved at higher speeds. The amount of external inductance added to the machine may be dynamically controlled by the required operating speed. Minimal external inductance is desired, as the reactive impedance negatively affects the power factor at speeds up to the base speed.

In a PMSM with open ended windings, it is possible to use an additional voltage source inverter (VSI) to boost the terminal voltage to the machine. The main or primary inverter is fed from a voltage source, and the secondary inverter is housed at the output terminals of the machine and is fed by capacitors Fig. 4.1. In this configuration, the terminal voltage available increases by a factor of $\sqrt{3}$ [87].

Additional increase in terminal voltage can be achieved when the capacitor is

charged to a greater voltage than the supply battery. In one possible implementation, equal AC voltage is applied to all the phases such that the resulting zero-sequence current is used to charge the secondary inverter's feeding capacitor to a higher voltage due to the boosting effect of the winding inductances. Benefits of this method include the ability to operate at MTPA at all speeds. Unity power factor operation can be achieved by control of the secondary inverter. Additionally, the introduction of a secondary inverter adds redundancy. In the case of a primary inverter failure, this inverter can be disconnected from the battery and machine and the corresponding motor terminals may be shorted. The battery may then be connected to the DC side of the secondary inverter [88]. If the failure occurs in the secondary inverter, the same actions can be taken with the exception of exchanging the battery connection.

The main disadvantages of this method include added cost to the system through requirement of a secondary inverter, and the restriction of application to open winding machines exclusively.

4.3 Mechanical Controlled Air-gap Length and Relative Stator Rotation

Constant power operation for axial airgap machines can also be achieved by modifying the machine mechanically as suggested in [89]. The method proposed utilizes a mechanical actuator to vary the air-gap distance dynamically. This serves to affect
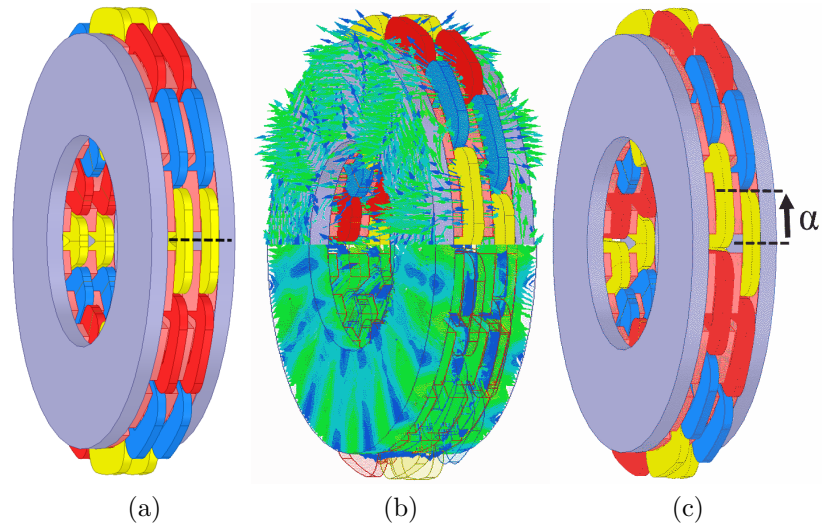
Figure 4.8: Constant power operation at higher speeds by relative rotation of the stators which reduces the winding factor, (a) Machine geometry without relative angular shift between the stator, (b) the 3D flux paths under these conditions, and (c) machine geometry after relative angular shift between the two stators is implemented. The shift angle, α, can be calculated based on the desired ratio of operating speed to rated speed.
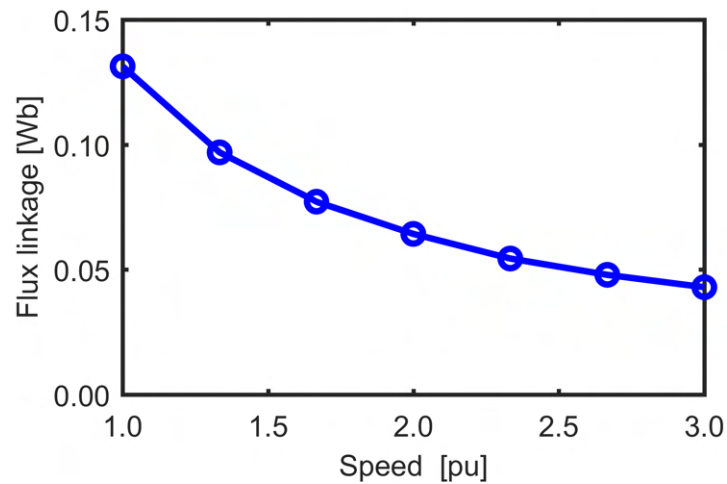
Figure 4.9: Flux linkage variation with shifting angle modified as a function of speed for a coreless AFPM.
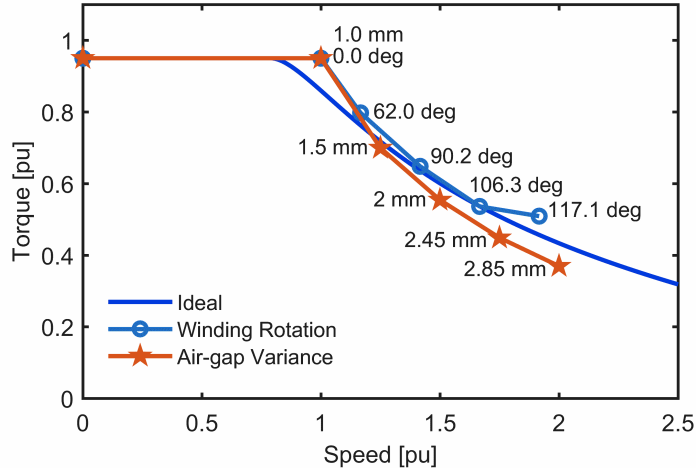
Figure 4.10: Torque-speed characteristics obtained using the air-gap variation and winding rotation techniques, along with the desired characteristics.

λ_{pm} and L_d as seen in equations (1) and (2).

An increase in the effective air gap, leads to a reduction in λ_{pm}, thereby permitting operation at higher speeds for a constant terrminal voltage. In [89], Heins et al. modeled the required air gap required for optimal efficiency over a given torque speed characteristic curve. The results of this study have been represented in Fig. 4.10. This method maintains MTPA through all operating ranges as no negative d-axis current is required to be applied. The peak operating speed is limited by the maximum value of air-gap that maintains structural integrity of the machine.

Operation at higher speeds can also be obtained in the coreless multi-disc AFPM by dynamically rotating the two stators relative to each other with increasing speed. This reduces the coil flux linkage due to decreased winding factor. An illustration of this approach is represented in Fig. 4.8. The shifting angle can be chosen, depending

on the desired ratio of maximum speed to base speed, and is calculated as,

$$k = \frac{\sin(\frac{m\alpha}{2})}{m \, \sin(\frac{\alpha}{2})} = \frac{\sin(\alpha)}{2\sin(\frac{\alpha}{2})} = \cos(\frac{\alpha}{2}) = \frac{n_r}{n} \; , \tag{4.9}$$

$$\alpha = 2\arccos(\frac{n_r}{n}) \; , \tag{4.10}$$

where m is the number of stator discs and α is the shifted angle between two consecutive stator discs in electrical degrees. For this example $m = 2$. n_r is the rated speed, 600 rpm, and n is the operating speed.

The maximum value of α is 180 electrical degrees, which results in zero flux linkage, and thus it may be inferred that the maximum operating speed is limited by only the mechanical constraints. The flux linkage versus speed with shifted discs is plotted in Fig. 4.9. The torque speed characteristics calculated from 3D FEA for the machine in Fig. 4.8 at different speeds with shifted coils is shown in Fig. 4.10, which demonstrates the successful operation of this technique.

4.4   Electronically Controlled Current Weakening

The available terminal voltage limits the maximum operating speed and therefore, increasing it would mitigate this limitation. In order to obtain constant power operation, the torque must reduce inversely with speed, which is accomplished by decreasing the q-axis component of the current as seen in Fig. 4.1. The phasor diagrams in Fig. 4.11 show how the voltage and current compare between this proposed

method and the traditional field weakening approach. In the current weakening approach, the d-axis current is maintained at zero at all speeds and therefore, maximum torque per ampere is maintained. The current weakening approach may be viewed as a means of extending the constant torque region of the motor.

In a traditional field weakening approach, at high speeds, the fundamental component of the flux density in the steel is reduced such that the core losses in the machine do not become prohibitively high. Since current weakening does not involve reduction of flux linkage and flux density, this method would lead to prohibitively high core loss in conventional machines owing to the high frequency and flux density. This can be seen in the following equation:

$$P_{hy} = K_h f B^{1.6}, P_{ed} = K_e f^2 K_f^2 B^2 . \qquad (4.11)$$

where K_h is the hysteresis constant, K_e is the eddy current constant, and K_f is the form constant.

This approach becomes feasible for use in coreless machines, wherein the steel and PM losses are nearly negligible due to the large electromagnetic airgap. Although at very high operating speeds, these losses could become significant, they can be virtually eliminated by special winding techniques [90]. Thus, since most of the loss occurs in the windings, the efficiency may in fact increase with operating speed owing to reduction in I_q.

The increase in terminal voltage with operating speed can be achieved through
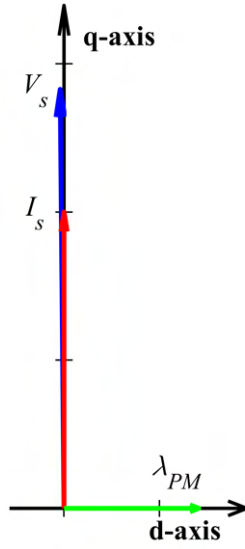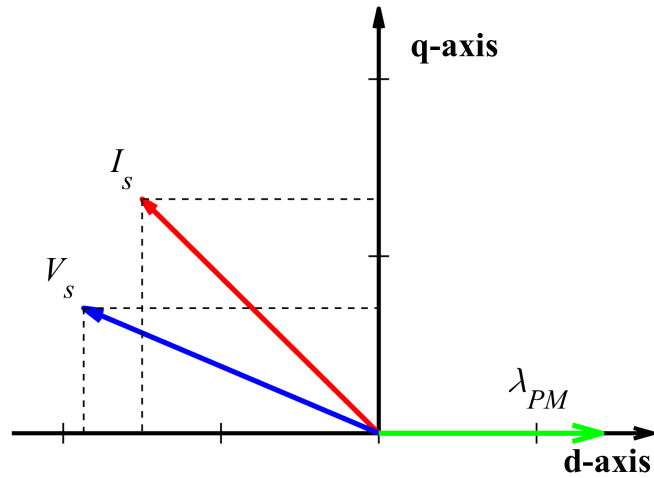
Figure 4.11: Phasor diagram for two generic permanent magnet machines with saliency operating at 2 pu speed and neglecting stator resistance. (a) Field weakening operation in a machine with per unit inductance of 0.707 through injection of d-axis current. (b) Current weakening operation of a machine with per unit inductance of 0.1. In this method there is no d-axis current injection and an oversized voltage rating of the drive.
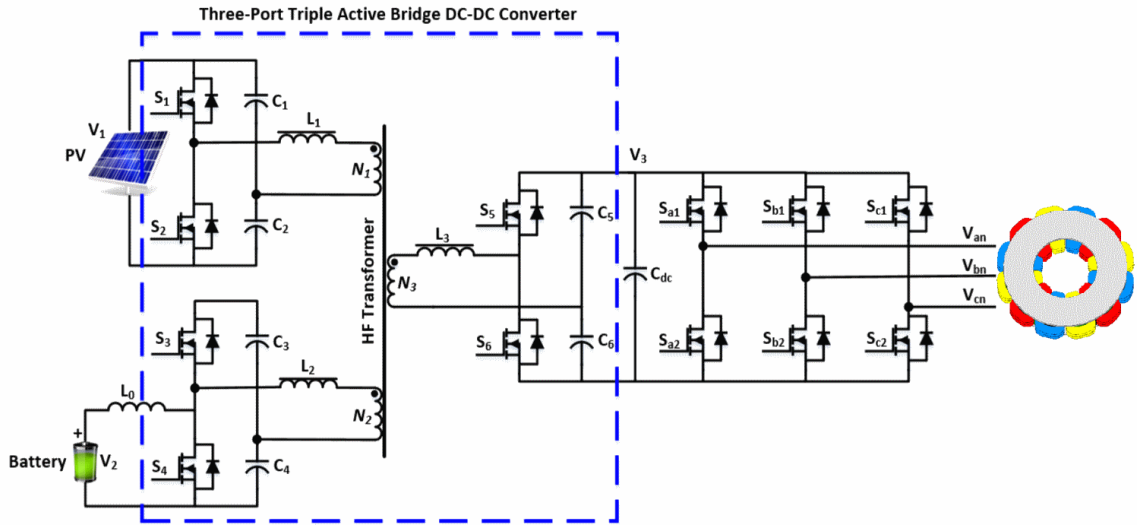
Figure 4.12: A three port dc-dc converter fed from solar panels and battery. A variable dc-bus voltage is provided to the inverter driving the traction motor. Such a configuration can be used to implement the current weakening method.

the introduction of a either a traditional boost stage prior to the inverter, or by the use of a multi-port converter as shown in Fig. 4.12 [82]. Boosting the DC bus voltage requires that the inverter is rated for a higher voltage by a factor proportional to the ratio of desired speed to rated speed. Power electronics efficiency enhancements are possible if the boost stage incorporates soft switching.

The proposed technique may be suitable for use in conjunction with WBG inverters, which would be required to reduce the excessive current ripple in such low inductance machines (Fig. 4.13). Although the devices must be rated for the maximum dc-bus voltage, the power electronics cost may not scale in proportion with the voltage due to the smaller switching loss and heat sink requirements. The smallest
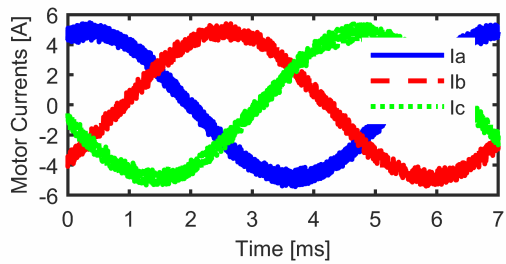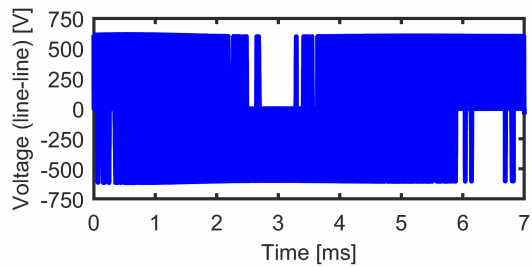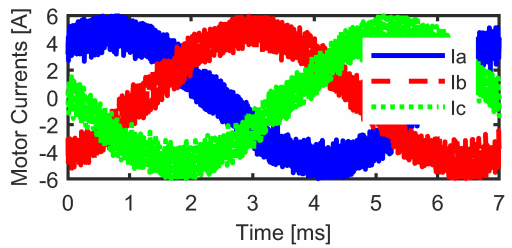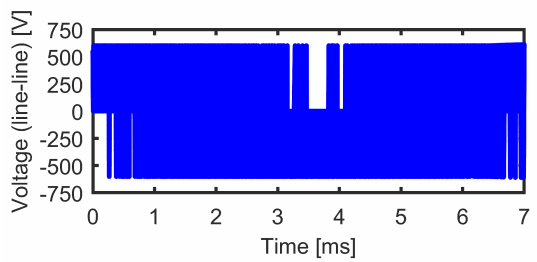
Figure 4.13: (a) motor phase currents and voltage of a machine with 1mH armature inductance, (b) motor phase currents and voltages of a machine with 0.5mH armature inductance.

rated WBG devices that meet current requirements of the motor drive which are commercially available have voltage ratings that exceed the rated voltage of the inverter present in UK's Gato del Sol by a factor of 3-4. Other benefits of this technique include the control of dc-bus voltage with load such that current ripple is always maintained within desirable limits.

This technique may also be suitable for applications in electric aircraft. It has been seen that trends in designs for electric propulsion motors in aircraft include machines with low inductance such as those seen in [91]. The proposed method is aimed towards the extension of operable motor speed while reducing current to maintain constant power, which may be favorable in the case of a propeller load.

4.5 Case Study of Solar Car with Triple-port Bi-directional Converter

Permanent magnet synchronous machines (PMSM) are popular because of their high efficiency, power factor, power density, and brushless operation. They have been used in different applications including solar powered electric vehicles [92]. Coreless axial flux permanent magnet motors (Fig. 4.14) consist of one or more central coreless stators, and two or more permanent magnet (PM) rotors. Several stator rotor discs may be stacked together for higher torque output. The power output from this machine increases linearly with the number of stator rotor discs as well. The rotor

PMs are arranged such that the magnetic flux flows axially, through the stator rotor discs. These machines, suitable for high-speed and high-frequency operation have been proposed for applications including solar airplane, solar car and generator [93–95], wind energy [96, 97] and in under water systems [98]. The stator coils, unlike in other machines are exposed to the air-gap fundamental flux, and need to be made of Litz wire in order to minimize the AC loss which could otherwise be prohibitively high [99, 100]. With windings in the air-gap, they present a very narrow range of field weakening, although a wide one is often required in electric vehicle applications. This has been achieved by mechanical field weakening, [101, 102]. These methods, although effective, may affect the stability of the vehicle.
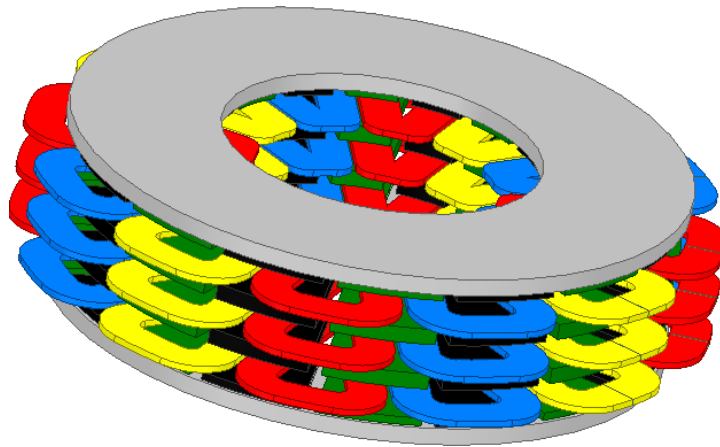
Figure 4.14: Exploded view of a coreless axial flux permanent magnet motor. The stator coils are mounted on non-magnetic supporting structures. Only the rotor discs on the ends are mounted on mild steel supporting plates, while the rotor in the center consists only of permanent magnets supported by a non magnetic structure (not shown).
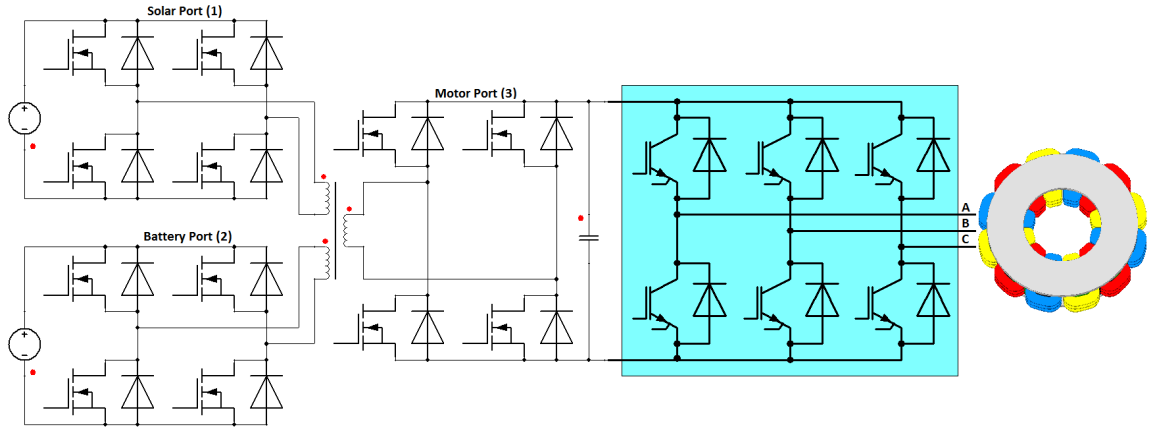
Figure 4.15: Three-port bi-directional isolated DC/DC converter, inverter, and motor for the drivetrain system of the solar race car. Schematic based on simulation from ANSYS Simplorer and Maxwell.
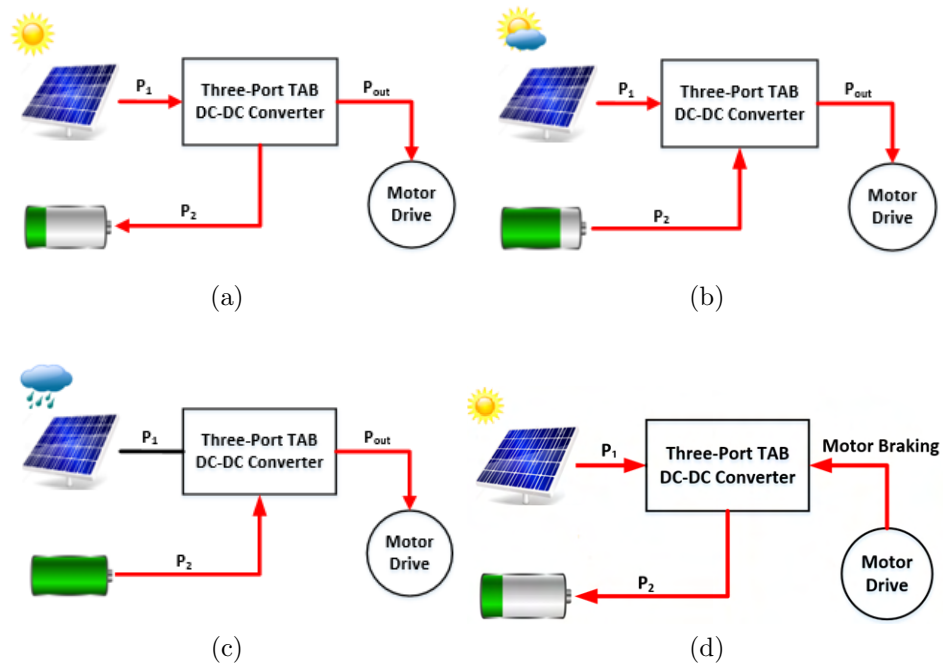
Figure 4.16: Operating modes of the three-port DC/DC TAB converter vary with the solar irradiation and operating condition of the AFPM motor: (a) Case I (b) Case II (c) Case III (d) Case IV.
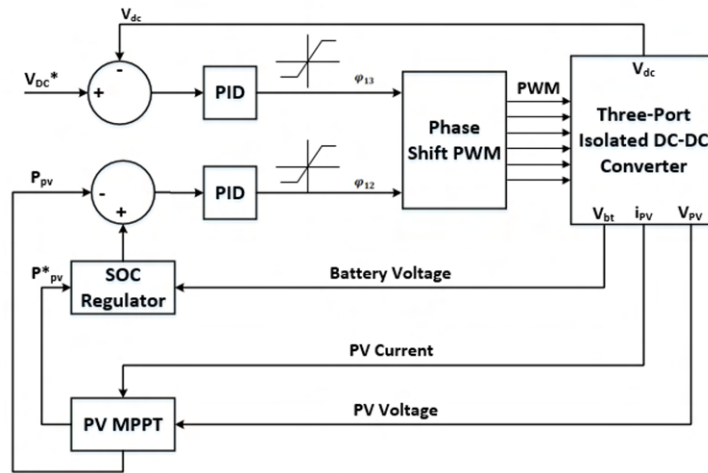
Figure 4.17: Control strategy for the three-port TAB DC/DC converter. The reference dc bus voltage comes from a look-up table requiring input from the motor speed (not shown).
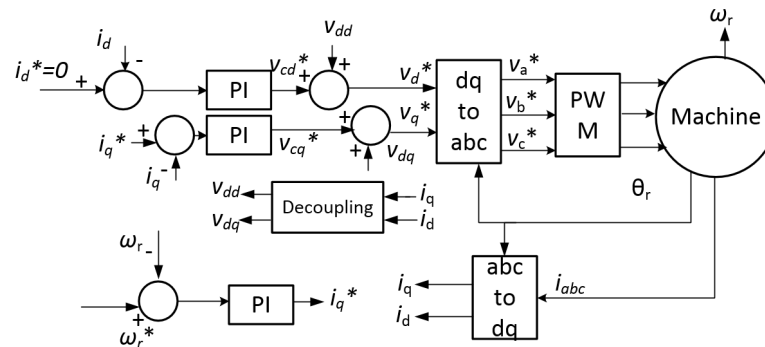
Figure 4.18: Control strategy for the coreless AFPM machine.

Table 4.1: System Parameters

Solar Cell Voltage [V]	60
PV Peak Power [kW]	1
Nominal dc Bus Voltage [V]	300
Switching Frequency [kHz]	100
Transformer Turns Ratio	6:8:70
Transformer Leakage Inductance [μH]	1,1.3,11.6

Table 4.2: Solar Car Motor Parameters

Output Power [kW]	1.75
L_d [mH]	1.32
I_q [A]	9.5
ψ_m [Wb]	0.24
R [Ω]	1.57

This section discusses current weakening achieved through an isolated bi-directional three-port triple active-bridge (TAB) DC/DC converter which connects the solar PV panels and battery to the dc bus of the inverter. High efficiency is achieved at all operating conditions owing to the use of GaN devices. In addition, the TAB converter also allows operation of the PV panel at its maximum power point (MPP) and bi-directional power exchanges between the battery and motor.

The power-train system of the solar race car in this work has two energy sources, namely, PV panel and the battery. A three-port triple-full-bridge (TAB) bidirectional DC/DC converter is proposed to provide a controllable dc voltage source for the motor. The basic circuit diagram of the TAB DC/DC converter topology is given in Fig. 4.15, which shows that there is a full bridge in each port, with a high-frequency

three-winding transformer coupling all the three ports. The leakage inductances of the transformer, L_1, L_2 and L_3, act as as energy transfer elements. The power flow between any of the two ports is galvanically isolated and bi-directional and is controlled by shifting the phase angle between the bridges. The operating principle of the TAB converter has been introduced in [103]. Multi-port DC/DC converters have been used in motor control, LED applications as reported in [104].

There are four operating modes for this three-port TAB converter, which will be detailed as follows:

- **Case I: At strong solar irradiation, the solar power is larger than the demand of the motor** $(P_1 > P_{out})$**.** Under these operating conditions, the solar PV system, which operates at its maximum power point to feed the motor, supplies the remaining power to charge the battery as illustrated in Fig. 4.16a.

- **Case II: At weak solar irradiation, the solar power is lower than the demand of the motor** $(P_1 < P_{out})$**.** At these times, the power flow from the battery reverses as compared with Case I, meaning that both the battery and solar system supply the motor, as seen in Fig. 4.16b.

- **Case III: At zero solar irradiation, the motor is powered by the battery** $(P_1 = 0, P_2 \approx P_{out})$**.** The full bridge converter on the solar side interfaces
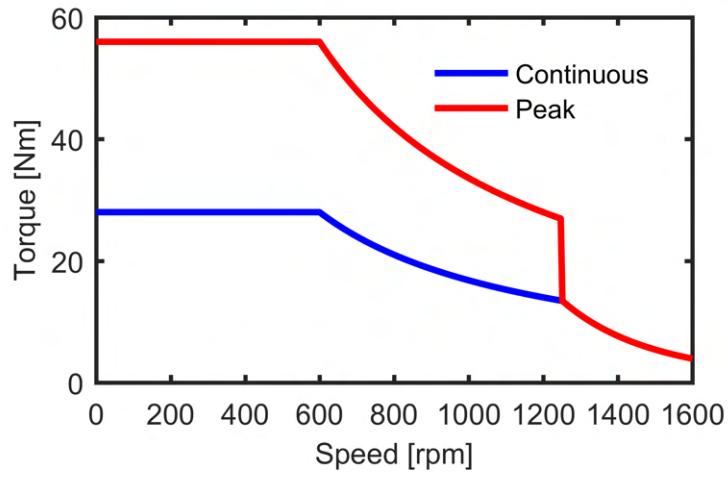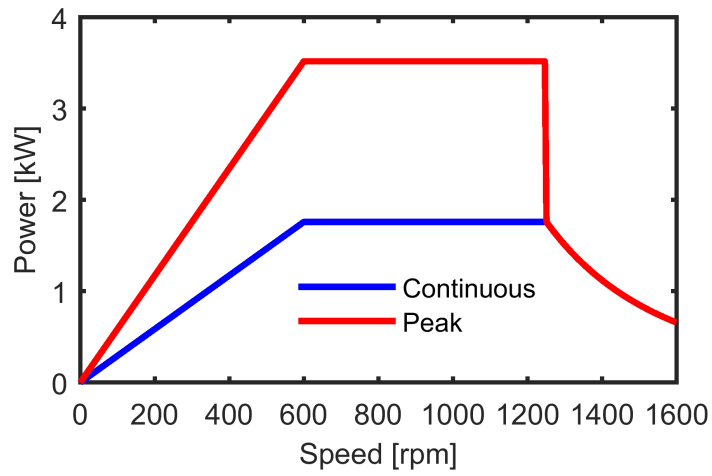
Figure 4.19: Typical overloading trends of (a) torque and (b) power in an axial flux brushless PM motor used for solar car applications.
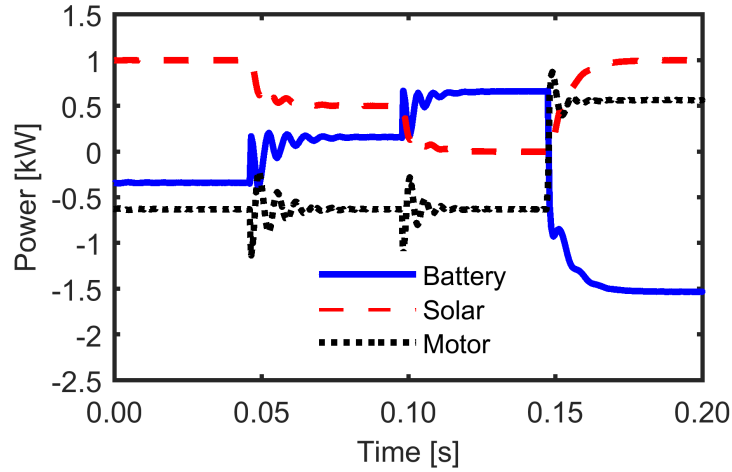
Figure 4.20: Power during the four operating modes of the DC/DC converter. A positive value indicates power being supplied by the element, while a negative value indicates the element is acting as a load, absorbing power.

no power (Fig. 4.16c).

- **Case IV: Battery is charged by the regenerative energy from the motor braking**. The motor side converter now operates in rectifier mode and supplies power to the battery. The solar PV continues to operate at its maximum power point (Fig. 4.16d).

Compared with the conventional power converter structure that has multiple DC/DC converters, this three-port TAB converter has higher efficiency, higher power density, centralization of power control between the three ports, and lower cost due to the nature of single power conversion stage and lower number of devices.

89
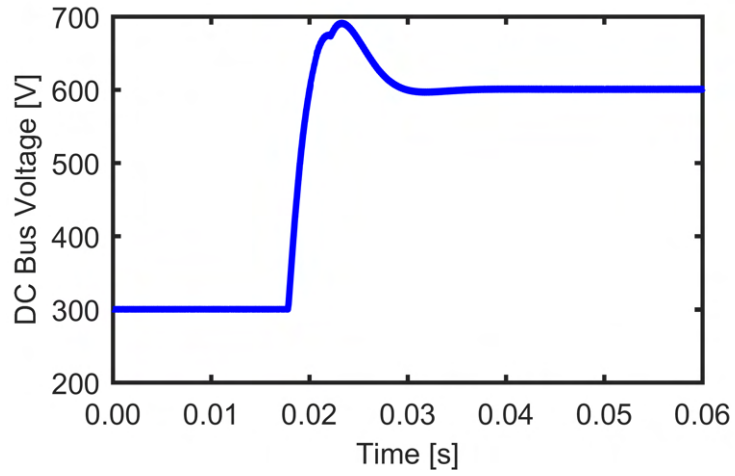
(a)
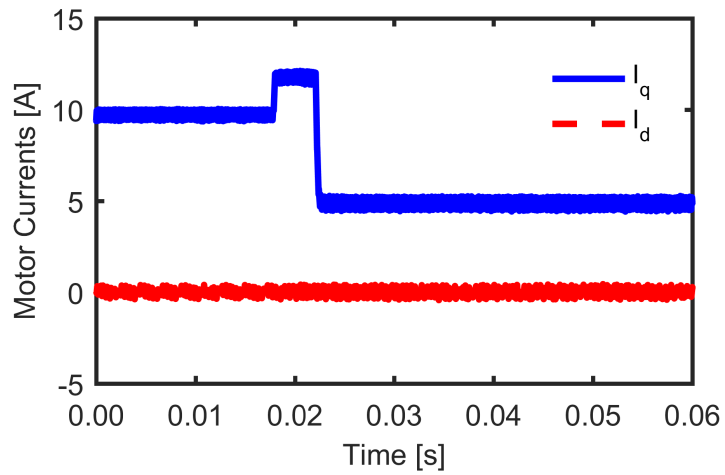
(b)

Figure 4.21: Response of the a) dc bus voltage and b) motor currents when current weakening control is conducted. The dc bus voltage can be changed in a few milliseconds, however the speed requires a longer delay to reach the desired value due to the inertia of the solar vehicle.

With the use of an AFPM as the driving motor it is beneficial to use high frequency switching devices such as GaN MOSFETs, which can operate in excess of 100 kHz. Wide bandgap devices have been used in renewable energy systems [105] and dc microgrids [106], and significant increase in power density has been reported [107]. In a coreless AFPM, the inductance is usually very small, resulting in a high current ripple. However, by implementing a higher than traditional switching frequency through the use of wide-bandgap semiconductors, the current ripple can be significantly reduced. Operation at low speeds might lead to very high current ripples owing to the large value of modulation index. In this case, the dc bus voltage is made to vary with speed, and therefore the motor can be made to operate at the modulation index leading to minimum current ripple.

Power flow in the three-port TAB DC/DC converter behavior is dependent on the phase angle between the gating pulses of the ports. ϕ_{12} is defined as the phase difference between the gating pulses of ports 2 and 1. Similarly, ϕ_{13} is the phase angle of port 3 with respect to port 1. The solar PV system can be modeled as discussed, for example, in [108]. In contrast with PV systems connected to a buck or boost converter, where the duty cycle is controlled to operate at the maximum power point as in [109], the duty cycle is maintained at a constant value of 0.5 in this system to avoid saturation of the transformer. The value of ϕ_{12} is chosen to always operate the solar PV system at its maximum power point. The control block diagram of the

three-port TAB converter is shown in Fig. 4.17. As can be seen, there are two major closed-loop control loops, namely, the dc-bus voltage control of the inverter and the dc power regulation from the PV and battery. The outputs of these two control loops are the PWM pulses with desired phase shift between the TAB full-bridge converters.

Vector control is used for the AFPM in which the q-axis current is regulated while the d-axis current is set as zero, as shown in Fig. 4.18. This is because of the lack of the rotor magnetic saliency in AFPM machine. For operation with current weakening at higher speeds, the dc bus voltage of the inverter is increased in proportion with speed by controlling ϕ_{13}.

In solar racing cars, there is a strong demand for high torque during low speed operation. This allows the vehicles to have greater acceleration from a starting position or at lower speeds. The cost of achieving this overload condition is higher current ratings, and therefore, higher power ratings of the inverter feeding the AFPM (Fig. 4.19). When current weakening is employed, the machine is capable of operating at its rated torque over a wide range of speeds, and hence a higher torque may not be required at low speed to achieve the required acceleration. Therefore, there may be only a small increase in cost of the inverter required to implement this operation method.

Two simulations were conducted to examine the power train circuit topology with the proposed current weakening control methods. The first shows the operation of the

system in different modes. From t=0.00 to t=0.05 seconds in Fig. 4.20, Case I, with the solar panel experiencing strong irradiation is simulated. The power produced is greater than the demand of the motor, therefore the battery is charged during this time period.

At t=0.05 seconds in Fig. 4.20, the system enters into the mode of Case II. The solar panel is experiencing weak irradiation in this time interval. The power supplied by the solar PV system is insufficient to meet the demand of the motor. The battery discharges in this scenario and aids the PV in supplying the load.

At t=0.10 seconds in Fig. 4.20, Case III begins. During this period, the solar panel sees zero irradiation and produces no power. All power demanded by the motor is supplied by the battery.

Case IV is simulated beginning at t=0.15 seconds in Fig. 4.20. The motor acts as a generator in this situation, regenerating power back to the battery. Power from the solar PV system is transferred to the battery if it experiences strong irradiation.

The second simulation demonstrates increase in the dc bus voltage of the machine, which permits the motor to run at higher speeds. As is shown in Fig. 4.21a, the commanded dc bus voltage is increased from 300 V to 600 V at t=0.02 seconds, in order to raise the operating speed of the motor from 600 rpm to 1200 rpm. The motor operates in the constant power region. In order to satisfy this condition, the q-axis current is decreased, as seen in Fig. 4.21b to maintain the power demand of

Table 4.3: Studied Motor Parameters:

k_e [V/krpm]	11.6
R [Ω]	0.49
L_s [mH]	1.85
I [A]	6.25
T_{em} [Nm]	0.78
Output Power [W]	245.3

the motor at a constant value, while the value of the d-axis component of the current stays at zero.

4.6 Case Study for Current Weakening Control in PM Motor Drives

A three-phase axial-flux machine was used to conduct both a simulation and an experimental study of the proposed current weakening technique (Fig. 4.22). The machine is driven by a three-phase, two-level inverter comprised of three half-bridge Silicon Carbide modules with integrated gate driver circuity, as seen in Fig. (4.23). Parameters and performance ratings for the studied machine are provided in Table 4.3.

Simulation

For a PMSM, the terminal voltage is given by,

$$V_q = kE_b - I_d\omega_e L_d, V_d = I_q\omega_e L_q, V_s = \sqrt{V_d^2 + V_q^2} \qquad (4.12)$$

where, E_b is the open circuit voltage at rated speed, k, the ratio of the desired speed of

94
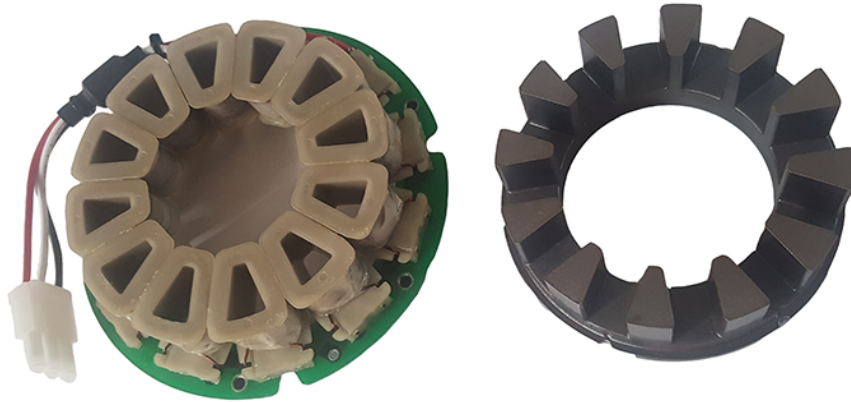
Figure 4.22: Three-phase axial-flux permanent magnet machine stator and core used for simulation and experimental studies. The machine uses a 10-pole ceramic magnet rotor (not shown).
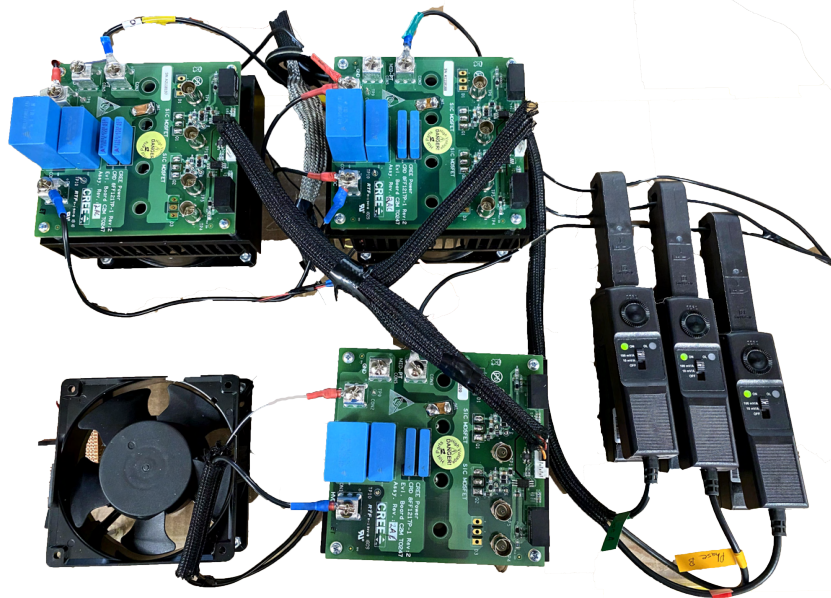
Figure 4.23: Three-phase, two-level inverter with Silicon Carbide MOSFETs, cooling and current sensors used for simulation and experimental studies.
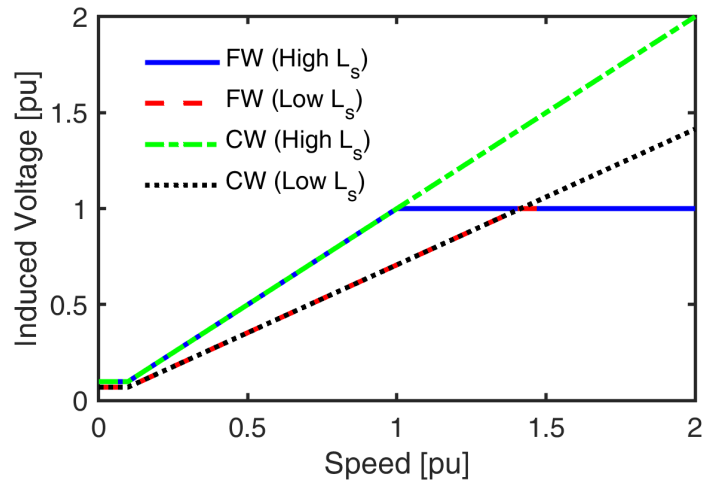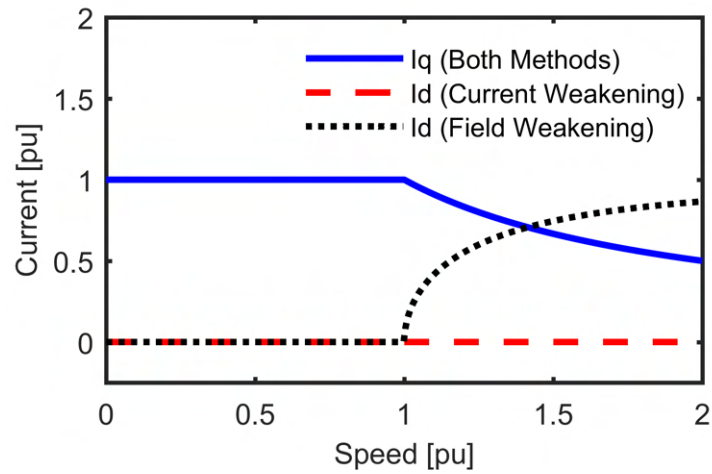
Figure 4.24: (a) ac induced voltage and (b) d-axis and q-axis current as speed increases past its rated value using both current weakening (CW) and flux weakening (FW) methods. A speed value of 1pu indicates rated speed of the motor.
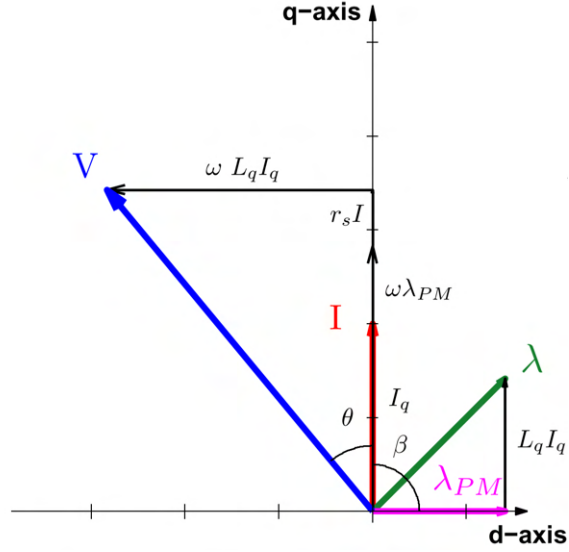
Figure 4.25: Typical phasor diagrams for a surface permanent magnet machines [38]. In a coreless machine the armature reaction is substantially smaller and according to the proposed concept the high speed constant power operation is achieved by weakening the current.

operation to the rated speed, V_q, V_d are the q and d axes components of the terminal voltage respectively, V_s, the terminal voltage, I_q, I_d, the q and d axes components of the current, ω_e, the electrical frequency in rad/s and L_q and L_d, the d and q axes inductances. Furthermore, the electromagnetic torque produced may be estimated as,

$$T = \frac{3}{2}p\lambda_{pm}I_q, \qquad (4.13)$$

assuming a three-phase, non-salient machine.

Using the estimated torque along with the known operating speed, the estimated electromagnetic power output of the machine may be calculated as:

$$P_{EM} = T\omega, \qquad (4.14)$$

97
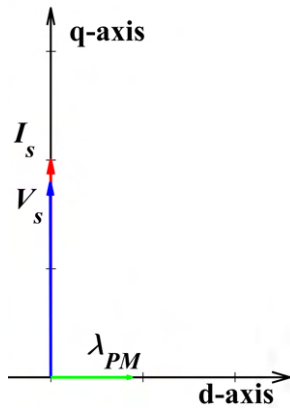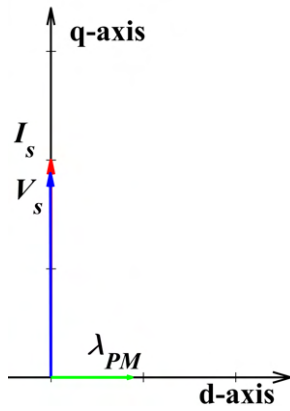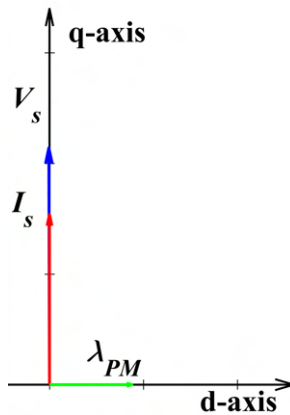
Figure 4.26: Phasor diagrams to scale for the axial-flux permanent magnet machine under current weakening conditions (a) 90% rated speed, (b) the base speed, and (c) 30 % above rated speed. As the operating speed is increased, current is reduced to maintain constant power
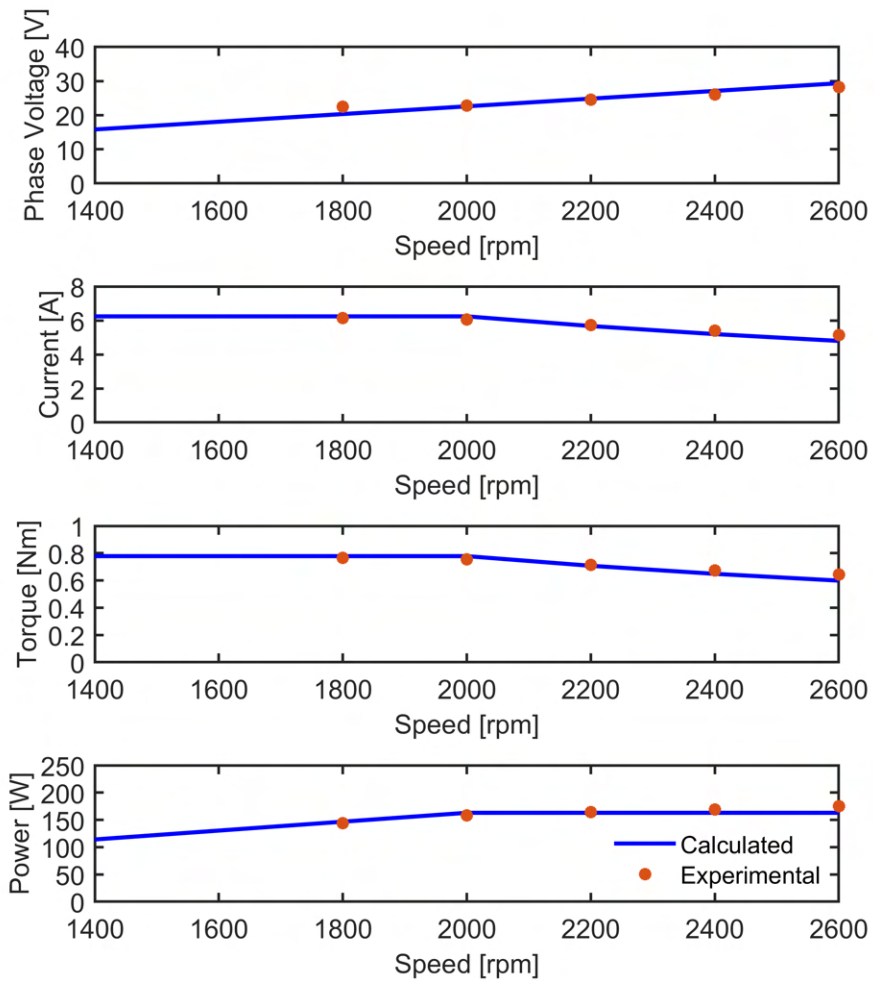
Figure 4.27: Simulated output characteristics of the AFPM machine under current weakening conditions. The five operating points highlighted on the curve were derived experimentally from the test AFPM machine and drive setup.

where ω is the shaft speed in radians per second. This estimation does not consider any losses incurred by the machine during operation, therefore, the copper losses were considered as:

$$P_{Cu} = mI^2 R, \tag{4.15}$$

where m is the number of phases and R is the phase resistance.

Operation at higher speeds is achieved by raising the terminal voltage (Fig. 4.24a). The machine always operates with all its current in the q-axis (Fig. 4.24b) and maximum torque per ampere is maintained at all speeds (Fig. 4.25). The terminal voltage is linearly proportional to speed and since operation in the constant power region is desired, I_q is reduced in inverse proportion with speed to meet this requirement. The phasor diagrams for conditions at 90%, 100%, and 130% base speed are shown in Fig. 4.26. A simulation model of the three-phase AFPM machine based on the equations in this section has been developed with ratings reflective of the experimental hardware. Operating conditions were simulated over a speed range, varying the current according to the proposed technique to maintain constant power past the base speed. These results were calculated using (4.12 and 4.13) with the experimental machine's parameters. The model was subjected to current weakening conditions, in which the reference speed was increased past the base value of 2000rpm. As the speed passes the rated value, current and therefore torque are both weakened (Fig. 4.27). Of this speed range, five operating conditions at 90%, 100%, 110%, 120% and 130% rated

speed were selected from the simulation and tested experimentally, as shown in Table 4.4. In the simulation, input motor power was estimated from the calculated electromagnetic power using (4.14) plus the copper losses (4.15). In practical applications, the machine will also experience additional supplementary ac losses and this is a subject for further analysis.

Table 4.4: Simulated and experimental operating conditions of the 3-phase AFPM machine. Experimental values are highlighted in bold.

Speed [rpm]	Inverter Power In [W]	Motor Power In [W]	Phase Voltage [V]	Current [A]	Copper Loss [W]	EM Torque [Nm]	EM Power [W]
1800	-	161.9	22.2	6.1	18.6	0.76	143.3
1815	**166.2**	**153.3**	**22.6**	**6.1**	**18.6**	**0.76**	**144.5**
2000	-	177.8	24.1	6.1	18.6	0.76	159.2
2031	**172.4**	**164.2**	**23.8**	**6.0**	**18.0**	**0.75**	**159.5**
2200	-	174.9	25.6	5.6	15.7	0.69	159.2
2183	**173.1**	**163.6**	**24.5**	**5.7**	**16.2**	**0.71**	**162.3**
2400	-	172.2	27.2	5.1	13.0	0.63	159.2
2437	**179.4**	**169.5**	**26.0**	**5.3**	**14.0**	**0.66**	**168.4**
2600	-	170.2	28.8	4.7	11.0	0.58	159.2
2557	**172.7**	**162.3**	**28.3**	**4.9**	**12.0**	**0.61**	**163.3**

Experimentation

The testing setup shown in Fig. 4.28 was developed for validation of the current weakening technique. Input commands were given at a host PC, on dSPACE ControlDesk software, where a graphical user interface has been implemented and testing data was viewed and stored. The dSPACE MicroLabBox controller was programmed with the speed control algorithms using MATLAB Simulink and code generation toolkits. Sensors attached to the hardware provide needed phase and dc bus voltage and currents, as well as shaft speed and position feedback information to the MicroLabBox by means of digital and analog interfaces. The inverter is supplied with a dc power supply of 60V for the bus, and 12V for housekeeping power. A switching frequency of 10kHz has been implemented in the experiments. The output of the converter is connected to the phase leads of a three-phase AFPM machine. This machine is coupled to a similarly rated dc generator feeding a programmable dc load, which is used to regulate load torque.

The five operation conditions mentioned in the simulation section were experimentally validated using the testing setup. A power analyzer was used to measure the input power into the inverter, the input power to the motor, and the line-line voltages of the machine and are recorded in Table 4.4. Additional validation was performed by considering the power at the dc load, which in line with expectation was lower considering the chain of losses. The measured PWM voltage of the machine,
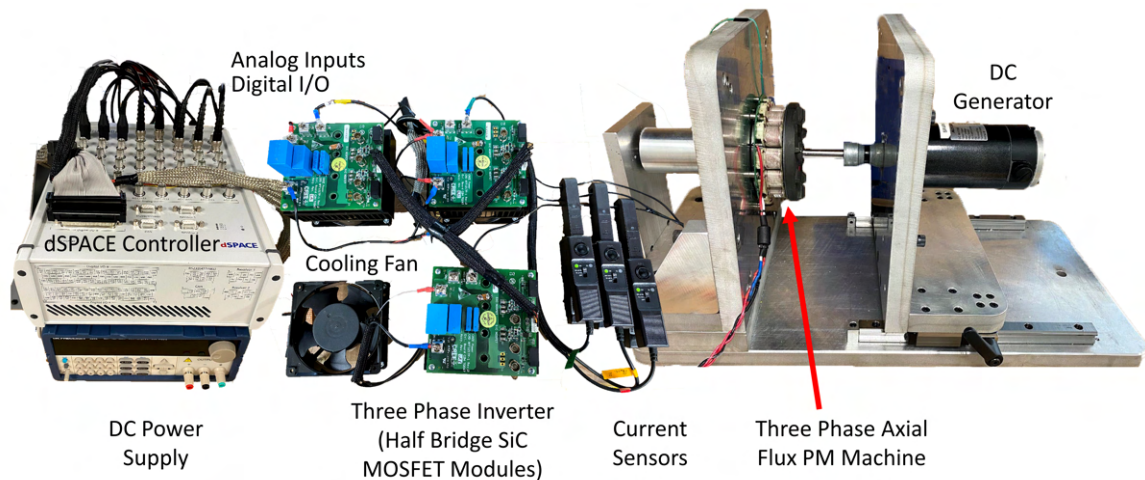
Figure 4.28: Experimental setup for validation of the proposed current weakening effect. A dSPACE controller, which provides gating signals to the inverter and reads feedback signals, is monitored and commanded using a graphical user interface on a host PC. A three-phase two-level inverter, implemented using Silicon Carbide MOS-FETs drives a three-phase axial flux machine. The machine is coupled to a dc generator and loaded using a programmable dc load.

along with the fundamental voltage at 2000rpm are illustrated in Fig. 4.29. The machine was loaded with the DC generator near the rated current of the machine, with phase currents of approximately 6A (Fig. 4.30). At this operating condition, the machine's dq-currents, calculated from the encoder position and phase currents, track the reference signals generated by the control algorithm (Fig. 4.31).

4.7 Summary

This chapter introduces the use of current weakening to achieve constant power operation of coreless axial flux permanent magnet machines for use in aircraft applications. A simulation study using a solar electric race car consisting of a machine
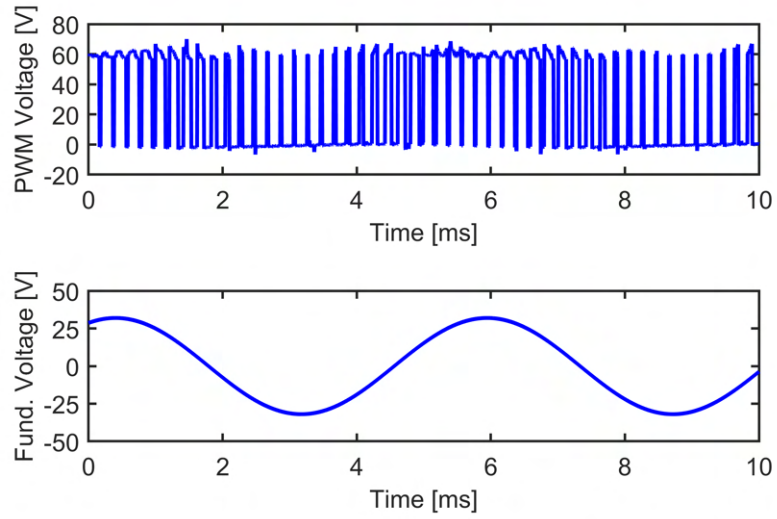
Figure 4.29: PWM voltages and fundamental voltage of the machine at 2000rpm.
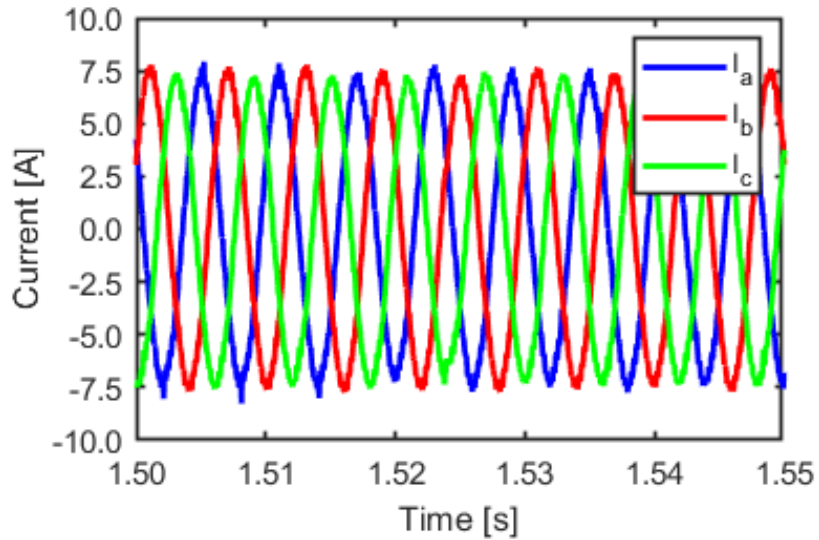
Figure 4.30: Phase currents and reference control signals of the machine during operation at full load.
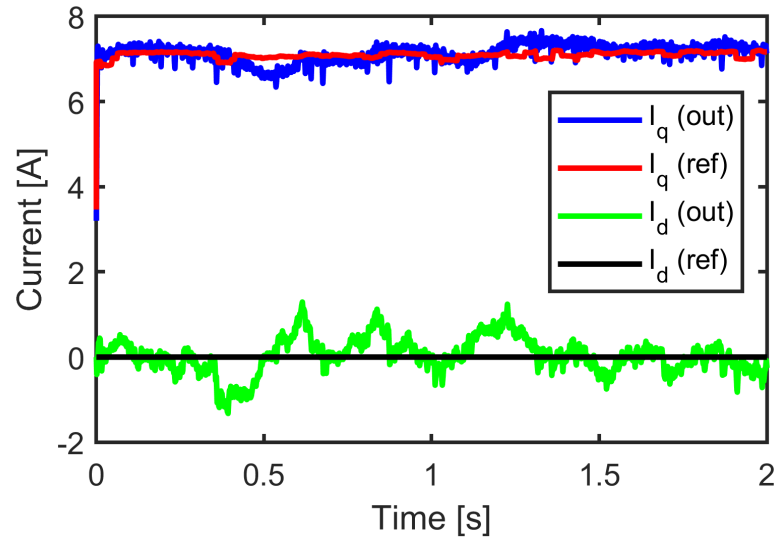
Figure 4.31: dq currents and reference control signals of the machine during operation at full load.

fed through a three-phase inverter. Control of the dc bus voltage is presented using a three-port full bridge bi-directional DC/DC converter. This converter has two sources, namely, a battery and solar PV panel which is operated at its maximum power point. The topology also allows bi-directional power flow between the battery and motor. Additionally, the proposed current weakening approach was validated with simulation and experimental results demonstrating operation of an AFPM machine and drive system at various loading and speed conditions.

Chapter 5

Coreless Permanent Magnet Machines for Electric Aircraft Propulsion

5.1 Introduction and Problem Formulation

Today, electric aircraft are becoming more feasible with recent advancements in alternative propulsion components such as electric machines, power electronics, and batteries. Efficiency and power density play vital roles in determining if an electric machine is a viable option for aviation. Coreless and slotless machines offer benefits of high power/torque density, no cogging torque, low ripple, zero or negligible core losses, and subsequently a high efficiency [83]. This chapter presents example coreless axial flux permanent magnet (AFPM) machine designs and evaluates their suitability for electric propulsion. Considerations for the design and performance estimates of coreless AFPM machines for aircraft propulsion are discussed. Additionally, design and prototyping has been conducted for two variations of Printed Circuit Board

(PCB) stators for 26-pole coreless AFPM machines and test results are included.

5.2   Literature Review

Attention has been drawn to coreless and slotless machines as potential aircraft motor topologies due to their high power density and efficiency. To the author's knowledge, one of the first applications of coreless machines for aerial propulsion applications dates back as far as two decades ago and originates from Professor J.F. Eastham's group at University of Bath. A multi-disc AFPM motor with plastic stator coil mechanical support was made for use in a high-altitude puesdo-satellite unmanned aerial vehicle [39]. The lightweight aircraft, powered by a combination of solar panels and fuel cells, had a total mass of just 70kg. The machine designed and tested was rated at an output power of 2.3kW at 1,000rpm, with a peak efficiency of approximately 92 % and 90 % when operated at half load (Fig. 5.1).

Coreless and slotless machines are realized with the elimination of the ferromagnetic stator core with non-magnetic supporting material or air. Common approaches for implementing the supporting structure for the windings include resin, plastics, or composite materials. Alternatively, stator coils may be glued or otherwise fixed to the structure of the machine with an air core. In conventional magnetic-cored machines, losses are produced in the core due to hysteresis and eddy currents. These core losses are typically reduced by adding laminations during stator core production, reducing
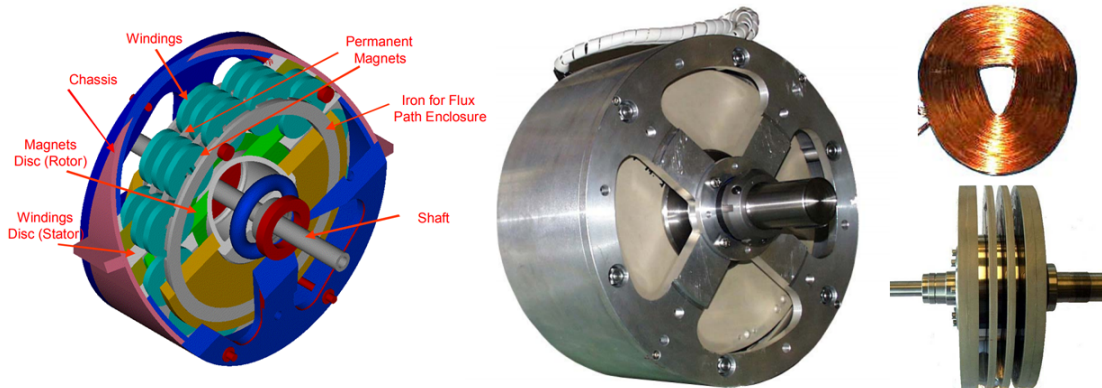
Figure 5.1: Pioneering development of an multi-disk coreless axial flux permanent magnet machine by Professor J.F. Eastham and his group at the University of Bath, designed for use in a high-altitude pseudo satellite unmanned aerial aircraft [39, 40].

the circulating currents. In coreless machines, these losses are eliminated, contributing to greater efficiencies, and also produce zero cogging torque, a characteristic which is favorable for low-noise and vibration applications.

Since then, there have been several design variations of these machines proposed and produced for electric transportation and other applications. A survey of recent coreless and slotless machine designs and their associated performance indices are presented in Table 5.1. These machines employ various stator winding implementations including multi-stranded wire, Litz wire and PCBs. Specific powers of the machines range from 0.3 to 2.3 kW/kg. Among them, the coreless AFPM machines are more attractive due to their modularized nature and high integrity. It is shown that the coreless and slotless machines can be designed to have a large variety of power ratings, ranging from tens of Watts to several mega Watts.

Table 5.1: Example coreless and slotless axial and radial flux permanent magnet (RFPM) electric machines.

Stator Type	Rated Speed [krpm]	Power [kW]	Ref.
Slotless-RFPM	15	1,000	[110, 111]
Coreless-AFPM	15	250	[112]
Coreless-RFPM	6	37	[113]
Slotless-RFPM	6	32	[113]
PCB-AFPM (Distributed)	25	16	[114]
PCB-AFPM (Spiral)	1.8	11.2	[115]
Coreless-AFPM	1	2.25	[116]
Coreless-AFPM	0.4	0.67	[117]
Slotless-AFPM	10	0.5	[118]
PCB-AFPM (Hexagonal)	0.375	0.4	[119]
PCB-AFPM (Spiral)	7.5	0.28	[41]
PCB-AFPM (Wave)	3	0.18	[44]
PCB-AFPM (Hexagonal)	2	0.04	[120]

In coreless AFPM machines, due to their lack of slot protection, the stator windings are directly exposed to the airgap flux density variations produced by the permanent magnets in the rotor. This implies that the machine is susceptible to significant ac losses in the conductors, particularly in machines with high pole count and at high speed operation. A common mitigation method used in such cases is to wind the machine with Litz-wire, reducing the conductor area and thus combating the skin effect, which reduces the losses [121]. Alternatively, multiple, smaller conductors may also be implemented as wire or in a PCB.

PCB windings have been considered a promising option for conductor area cross-sectional minimization to suppress induced eddy currents. Compared to traditional

wired windings, planar PCB windings benefit from increased flexibility and convenient design modification allowing for coil optimization, accuracy, and limited variation between stators, as well as better heat management performance due to better dissipation [44, 119].

Rigid PCB motor stators, as explored in recent years, are comprised of winding topologies, which use planar copper conductors to generate magnetic fields when an AC voltage input is applied. Torque and electromotive force (EMF) production are often optimized by maximizing the planar copper conductor's radial alignment with parallel paths being used as a planar analogue for wired stator turns [42, 44]. As such, rigid PCB stator winding designs generally focus on the maximization of radial or active conductors while minimizing heat generation in the inactive sections [41, 119]. The optimal winding pattern for improved performance is a subject of research covered in recent literature. PCB stators are seen with various implementation methods, both concentrated and distributed such as, wave windings [44, 122], radial or spiral windings [41, 42, 123, 124], and hexagonal concentric windings [119, 122, 125]. Within the topologies, the number of waves or coils and PM poles vary. In most designs, conductors, which share a phase are connected in series and multiple boards may be coupled in parallel to add current-carrying capacity.

Wave winding topologies, such as the design in [44], focus on maximizing the active radial conductor length and exhibit high scalability with increased pole pairs,

but have less capability for greater number of turns. Radial windings, such as the parallel/radial mix showcased in [42], also focus on maximizing active length and have lower phase resistance but are not easily scalable for increased PM poles and utilize less conductor length for active EMF generation. Hexagonal concentric windings maximize space and potential turn capacity while minimizing losses by reducing the inactive conductor length through inclined edges that slightly reduce active output. Series connections of hexagonal concentric and radial windings require a minimum of two layers to radially cross the PCB but allow for more turns accordingly. Wave type windings, as proposed in [122], minimize inactive sections but require multiple layers to implement and are difficult to scale with increased PM poles. Distributed windings, as used within [41], have lower copper loss due to increased heat distribution and can handle higher currents due to variable line thickness but lack in turn capability.

The number of layers, copper depth, and PCB type were also varied in previously implemented PCB stators. Utilization of multiple layers connected in parallel with plane spanning copper vias increases the current-carrying capacity and reduces the winding's resistance but increases the magnetic gap and overall cost. PCB stacking has been used as a method of increasing the number of turns and phases of PCB motor stators to compensate for the overall cost, but still increases the magnetic gap and introduces additional points of failure where the PCBs are connected in parallel. Limitations imposed by the manufacturing capabilities of standard PCB

mills restrict copper conductor depth and the current carrying capability of singular traces, accordingly. The remaining design parameters to increase the current capability include trace width modification, which effects isolation distance required between traces, and the number of PCBs or traces connected in parallel. Other groups have resorted to self-plating or manufacturing their own PCBs to gain greater copper depth and associated current carrying capability to examine and optimize PCB configurations [43]. Flex-PCB, or flexible PCB, motor stators have also been explored. In such instances, these flexible PCBs are folded in on themselves to create a greater number of turns, increased fill factor, and radial magnetic field contributions [43, 126, 127].

5.3   Electric Aircraft Propulsion Requirements for Electric Machines

The electrification of aircraft propulsion systems involve generating thrust, traditionally produced using combustion engines, with electric motors driving fans or propellers. To achieve this, machines with large power ratings, high reliability, low mass, and high efficiency are required. In addition to these critical performance indices, low noise, vibration and harshness are desired traits. Today's electric motors for aviation applications have achieved specific powers in excess of 5kW/kg and NASA has set immediate future goals of 13kW/kg [128].

For an estimate of the extended speed range required, a design with a maximum
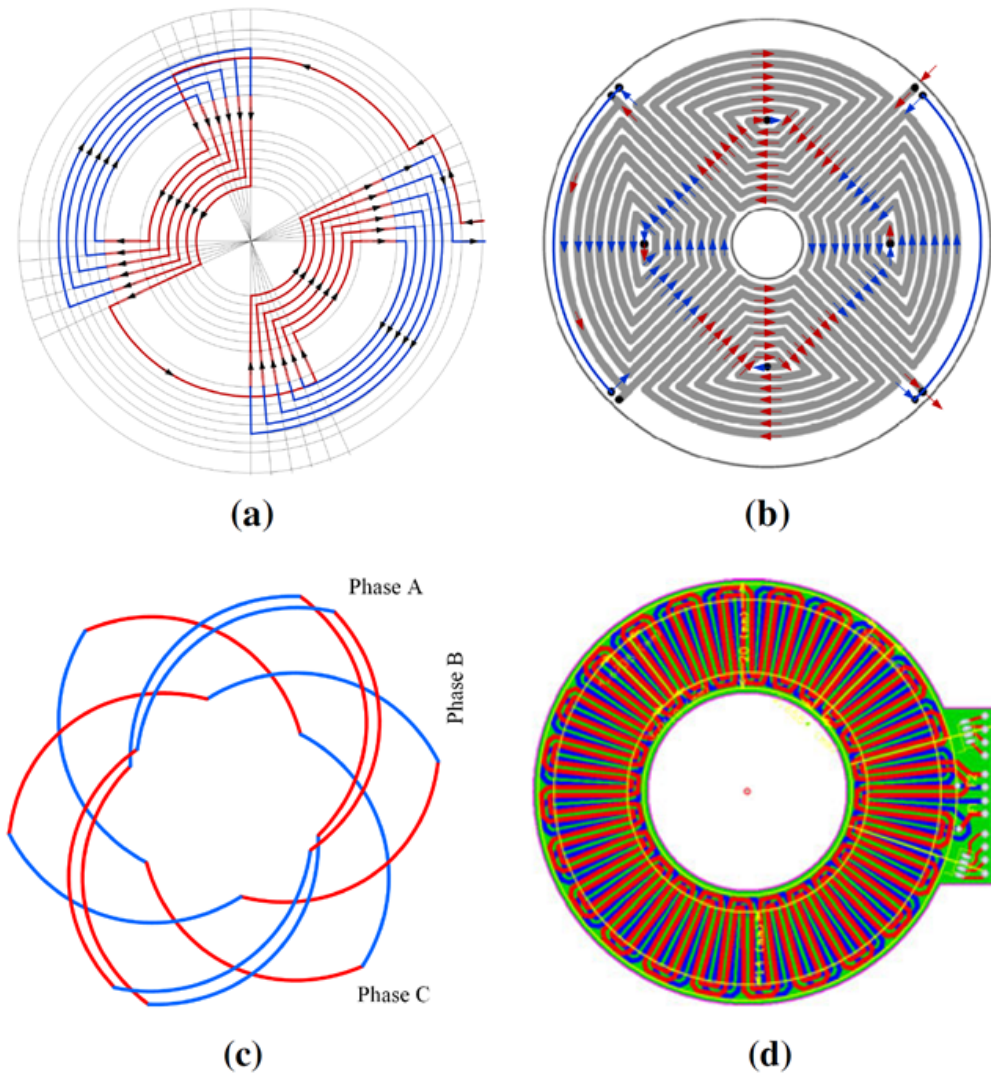
Figure 5.2: Typical PCB winding topologies, (a) Distributed winding with one phase shown [41], (b) spiral winding [42], (c) progressive wave winding with a single coil unit shown for Phases B and C, two coil units for Phase A [43], (d) continuous wave winding [44]. Red lines/arrows denote the top layer traces and blue, the bottom layer. Spiral and continuous wave winding are inherently suitable for high-polarity designs.
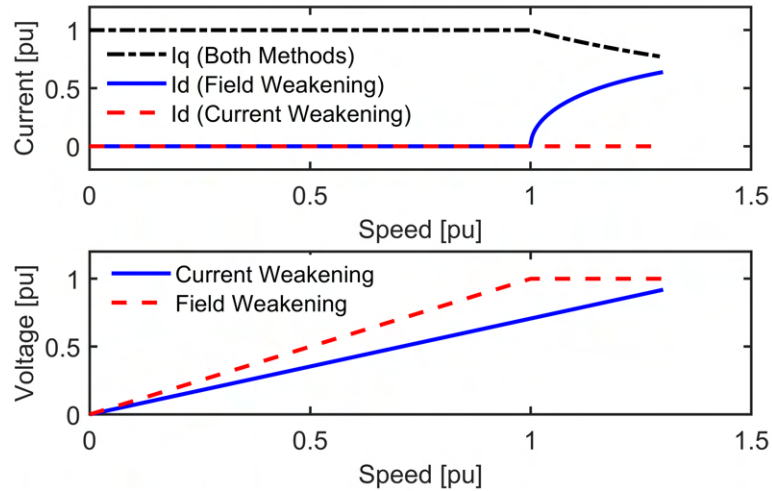
Figure 5.3:   Machine current and induced terminal voltage in flux weakening and current weakening techniques for extended speed, constant power operation. In electric aircraft propulsion applications, a constant power speed range of only approximately 30 % is required.

speed 36 % above the base speed has been developed by MagniX's cored AFPM motor used for short-haul electric aircraft [129] and as illustrated in Fig. 5.3. Coreless machines typically exhibit much smaller inductance than traditional cored electric machines and as a result the maximum speed achievable at constant rated power by using traditional field weakening techniques is much lower. The required terminal voltage to operate at a given angular velocity is lower, however, for machines with a small inductance. Implementing techniques such as relative rotation of the stators discs as a means to reduce flux linkage or by using a controllable DC boost stage to the motor drive's input and use of a current weakening approach may allow constant power operation for the additional speed range required.
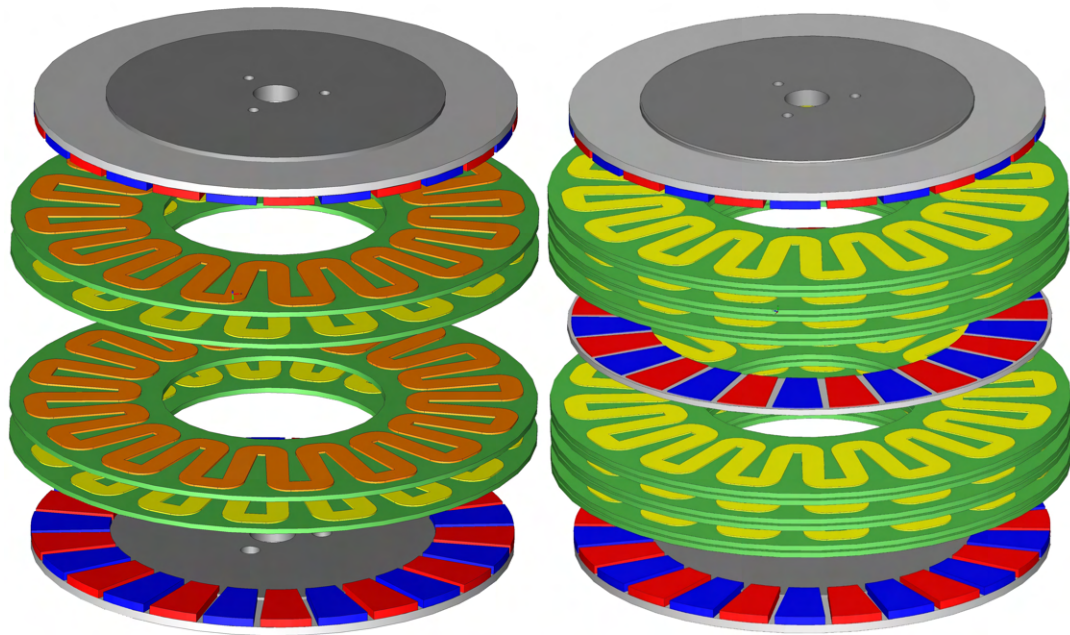
Figure 5.4: The nature of PCB stators and coreless machines offer a modular system, facilitating scaling of machine ratings achievable based on application requirements.

5.4 Design Considerations and Performance Estimates for Coreless AFPM Machines

An AFPM machine's disk-shaped stator provides opportunities for implementing the windings in unique ways, such as using PCBs. The fabrication process of PCBs is reliable, highly repeatable and has been proven in consumer electronics. Electric machine designers may make modifications to a stator's coil shape, track width, or winding configuration in professional circuit design software with minimal impact to the manufacturing setup. PCB stators may also offer a modular approach to machine design specification as it is possible to stack multiple boards in parallel or
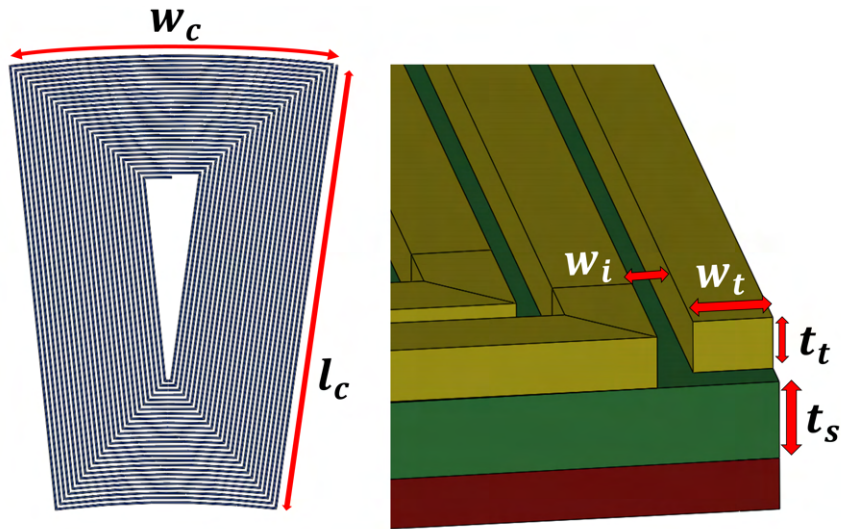
Figure 5.5: Main geometric variables for PCB stators in coreless machines. The coil shown has a spiral pattern and connects to internal layers using vias. The number of coils per PCB is the same as the number of PM poles.

series to increase speed or torque rating (Fig. 5.4). Design of the windings is a key factor to the overall effectiveness, defining a significant portion of the losses and related efficiency [130], geometric considerations for PCB stators include trace width, thickness, isolation distance, and substrate thickness, as shown in Fig.5.5.

Considering the modeling complexity and computation time, analytical equations are recommended to be used in the early design stage for initial size and torque estimation, following those equations described for example in [131]. The power output of a coreless AFPM machine is related to its rotor speed, dimensions, airgap

flux density and the current loading, as expressed by:

$$P = \frac{B_m A \pi^2 n D_o{}^3 (1 - \lambda)(1 - \lambda^2) k_{fr}}{240\sqrt{2}};$$

(5.1)

$$A = \frac{2NmI_{rms}}{\pi D_m}; \quad \lambda = \frac{D_i}{D_o},$$

where P is the output power, B_m is peak flux density in the airgap, n is rotational speed, D_o is the outer diameter and assumed to be 1, k_{fr} represents the fringing coefficient. When estimating, A, the current loading, m is the number of phases, D_m is the mean diameter, D_i is the inner diameter and N is the number of turns in series per phase. The maximum current, I, may be derived as:

$$I = Ja; \quad a = t_t w_t n_p,$$ (5.2)

where J, is the current density, a is the cross-sectional area of the copper in an equivalent coil, which in PCB stators, is a function of trace width, w_t; thickness t_t; and number of traces in parallel, n_p. While wire wound stators using Litz wire or multiple stranded wire offer a higher slot fill factor, PCB stators may allow a higher current density to compensate for the reduced copper area.

Based on these power sizing equations, the material properties, insight into how performance scales with parametric sweeps in independent design variables may be obtained. The machine mass has been calculated considering only the active components of the motor, the rotor magnets and back iron and stator PCB. The densities

of active materials - NdFeB, laminated electrical steel, PCB substrate (FR4), and copper were used as 7.45, 7.65, 1.85, and 8.96 g/cm^3, respectively. The produced prototype wave winding stator and rotor masses, described later in this chapter, were measured to be 0.16 and 3.84kg. Both the analytical estimates for the stator and rotor are within and 5 percent error at 0.153 and 3.64kg, thus verifying that the active mass calculations are valid estimates. Assuming the same ratio of OD and ID as the original prototype of 180mm/200mm, it can be seen that the machine's mass scales non-linearly with OD in Fig. 5.6.

The analytically calculated power and specific power of a coreless, PCB implemented wave wound machine with dimensions of the proposed prototype are illustrated in Figs. 5.7 and 5.8. As expected from Eq. 5.1, the power and subsequently, since the machine dimensions do not change, specific power increase linearly with the rated speed. For a given speed, however, the specific power exhibits a non-linear trend with the number of PCBs used in the stator stack. The allowable RMS current and current loading is proportional to the number of PCBs used in parallel. As additional PCBs are added to the machine, the total mass increases only marginally, considering a significant portion is the contributed by the two rotors. Under the assumption that the losses are low, these results show that for high speed applications, then coreless PCB machines show potential to exhibit high power densities.

Furthermore, the coreless machine's stator parameters may be estimated from
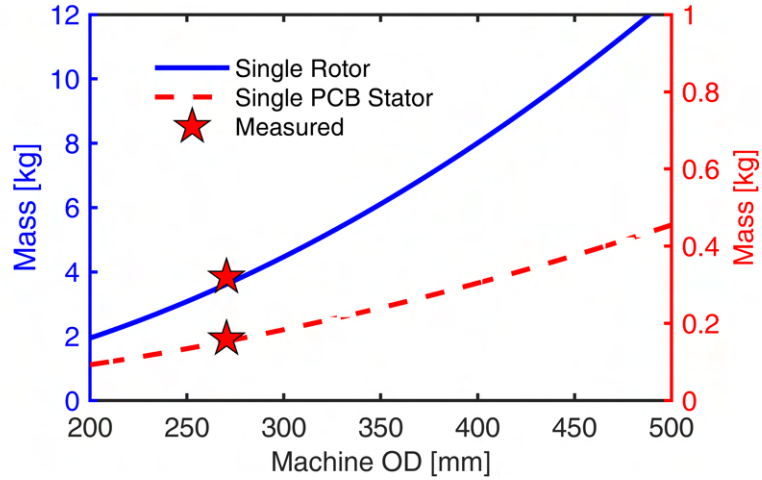
Figure 5.6: Mass of the proposed 26-pole coreless rotor and a single wave winding PCB stator, as a function of the outer diameter. It has been assumed that as the OD increases, the ratio of OD to ID remains constant at 180mm/280mm, which is used for the prototype machine. Markers indicate measured mass of the prototype active components.
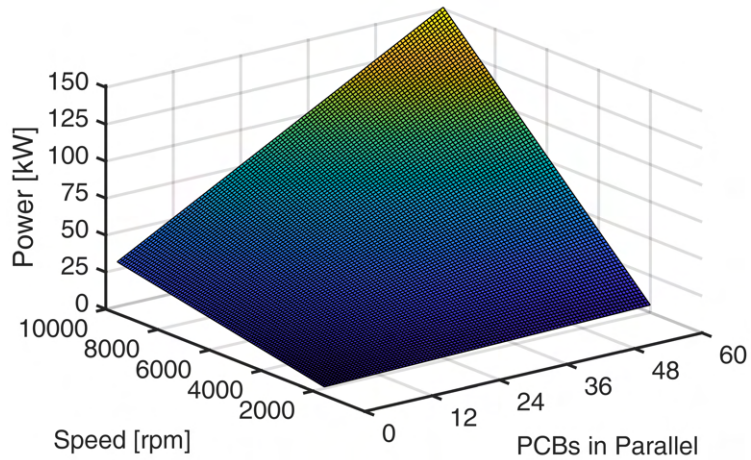
Figure 5.7: Analytically calculated power of a two-phase coreless AFPM using the PCB wave winding stator, as a function of both the rated speed and number of 1mm thick PCBs used. 150kW may be achieved with just 60mm axial length of PCB stator and a rated speed of 10krpm.
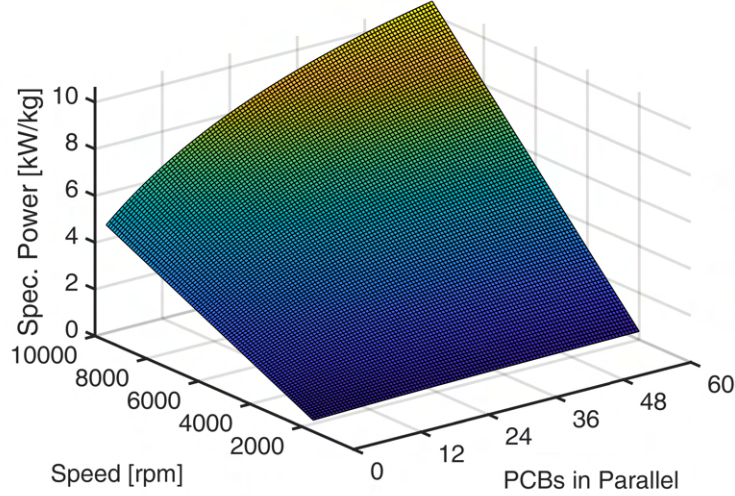
Figure 5.8: Analytically calculated specific power of a two-phase coreless AFPM using the PCB wave winding stator, as a function of both the rated speed and number of 1mm thick PCBs used. Since a significant portion of the machine mass comes from the rotor, as more PCBs are stacked in parallel, the specific power increases.

analytical equations. The trace, or corresponding phase resistance, may be calculated as:

$$R = \rho L / t_t w_t [1 + \alpha(T - 25)], \tag{5.3}$$

where ρ is the resistivity of the copper in the windings, L_t is the trace length and T is the ambient temperature, assumed to be 25 degrees Celsius.

Similarly, stator inductance, L_s may be estimated using the following equation:

$$L_s = \frac{m\mu_o(k_{w1}N_t)^2\tau_p L_{Fe}}{\pi^2 p(k_c g + \frac{L_{pm}}{\mu_{mr}})} \frac{1}{k_{sd}}, \tag{5.4}$$

where μ_o is the permeability of free space and μ_{mr} is the relative permeability of the magnets, which for NdFeB, is assumed to be 1.05. The number of turns is N_t, τ_p is the pole pitch, L_{Fe} is the outer diameter minus the inner diameter of the machine, k_c
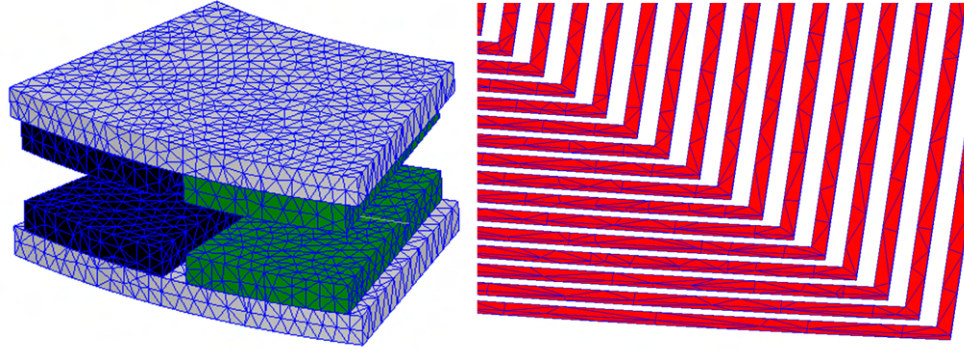
Figure 5.9: Meshing of detailed trace-by-trace model of the proposed PCB spiral winding coreless AFPM machine. The rotor back iron and magnets (left) and PCB traces (right). To provide an accurate model, the mesh for 1/13th of the machine results in over 26 million tetrahedral elements and requires over 72 hours to solve on an HPC system.

is Carter's coefficient for electric machines, k_{w1} is the fundamental winding factor, g

is the magnetic airgap, L_{pm} is the length of the permanent magnets in the direction

of magnetization, in this case, the axial direction, and k_{sd} is the saturation coefficient,

assumed to be one.

Based on the dimensions determined by equations (5.1) and (5.2), finite element

models were built and used for further performance estimation, including the eddy

current loss of PCB windings. A trace-by trace 3D representation was used in the

analysis for the windings, leading to a very dense model with *26.4 million tetrahedral*

meshing elements, as seen in Fig. 5.9 and Fig. 5.10. Such large models are computa-

tionally intensive, requiring over 72 hours to obtain data for a single electrical cycle,

therefore a high performance computing (HPC) cluster with 64 cores and 192 GB of

RAM was used to perform the calculations.
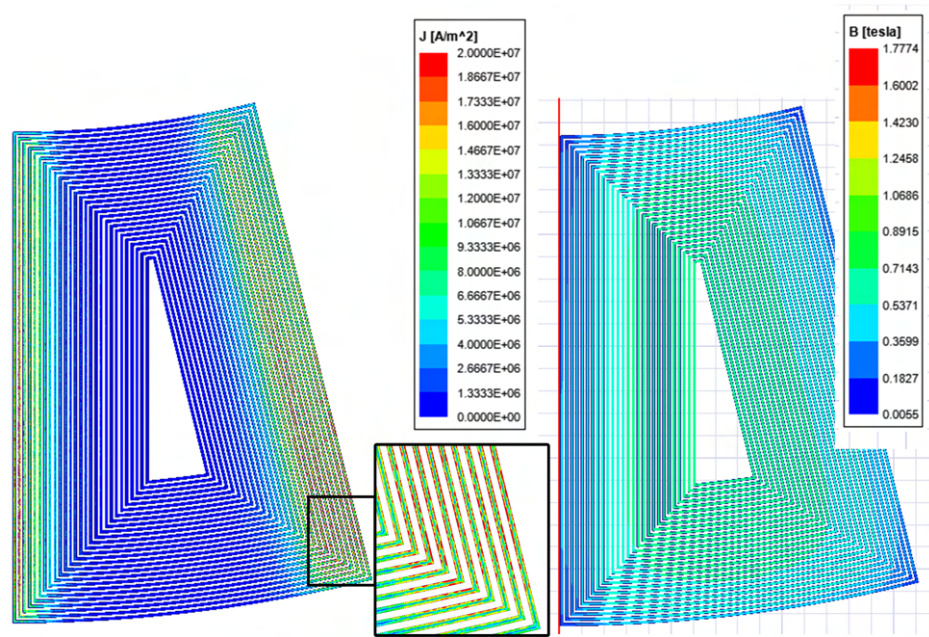
Figure 5.10: FEA results of current density distribution and flux density distribution in a spiral type PCB stator coil under open-circuit condition at 3,000r/min. Current is most highly concentrated at the edges of traces due to the eddy effect.

Figure 5.11: Illustration of the printed circuit board (PCB) winding implementation for the proposed wave winding stator.
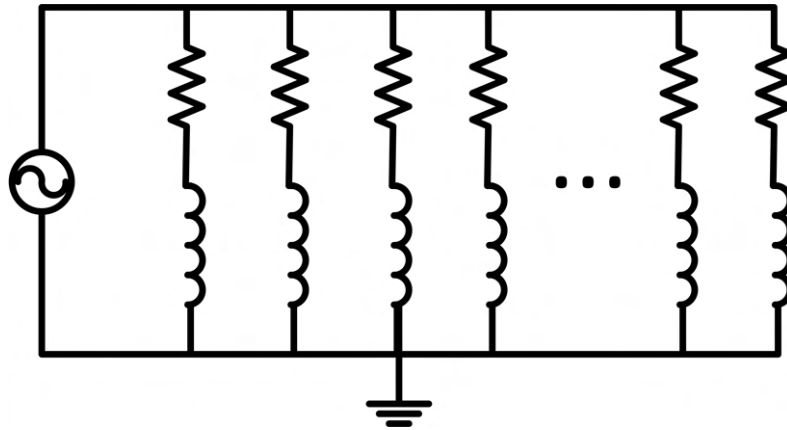
Figure 5.12: Circuit used for analysis of circulating current. The network consists of the same number of parallel resistive and inductive branches as the number of parallel traces in one turn of the wave winding machine. Induced voltage data taken from the FEA model has been used to determine the AC source applied.
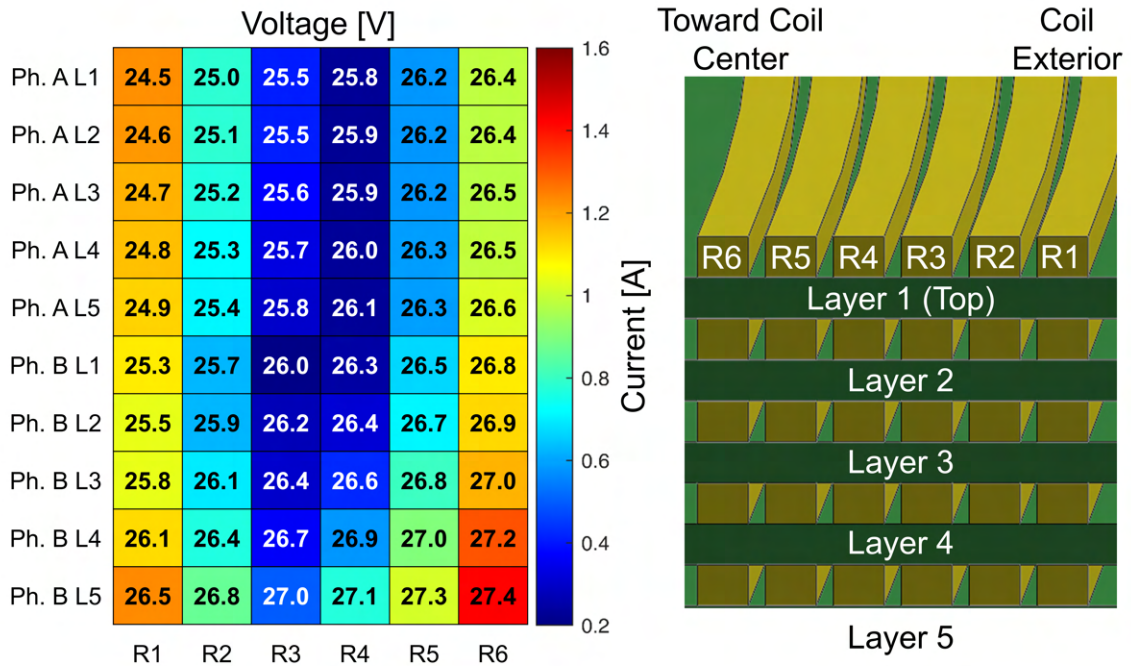
Figure 5.13: FEA calculations of induced voltage and peak circulating current in 60 active traces composing the outermost turn of the wave winding PCB toward the OD (left). Results shown are under open-circuit conditions. Naming convention for a single turn (right).

5.5   Wave Winding

The designed wave winding PCB stator utilizes a 6-layer stackup, five of which host active copper while the remaining layer is used primarily as a path to route the return terminal to the outer diameter of the stator. On each of the active layers, there are 42 traces with a trace width, w_t, of 8mil and an isolation width, w_i, of 10mil. For the same layer, conductors are grouped in parallel connections of six traces. These parallel groups of six are then connected in series to form seven turns. The same wave pattern is repeated in a total of five layers, all connected in parallel using vias. The winding pattern implemented for this wave PCB stator design is further detailed in Fig. 5.11.

The wire groups perpendicular to the magnetic field produced by the rotor magnets consist of independent traces, which vary in their distance from the magnets, both axially and radially. This difference in magnetic field variations and distance results in unequal induced voltage in each trace, which produces circulating currents. The detailed trace-by-trace FEA models allow open-circuit analysis of this effect, by obtaining the induced voltage in each trace. By calculating the resistance and using an equivalent circuit, as seen in Fig. 5.12, the resultant circulating current in each trace can be obtained. For a dual, parallel connected wave winding PCB, it can be seen in Fig. 5.13 that currents may reach as much as 2.3 A/mm^2 in some traces.The FEA models were also used to estimate the torque production of the machine (Fig.
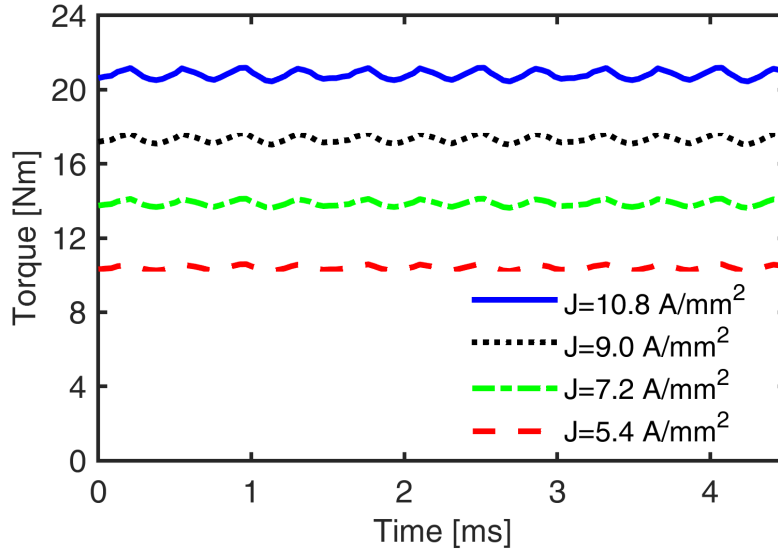
Figure 5.14: FEA calculated torque production of the proposed two-phase wave winding PCB coreless machine under different current density conditions.

5.14).

The detailed FEA models were adapted into manufacturing specifications by importing them into electrical computer-aided design (ECAD) software to create PCB schematics and layouts, as in Fig. 5.15. In addition to the winding pattern previously described, testing points have been added in order to study induced voltages.

5.6   Spiral Winding

The designed spiral winding PCB stator also utilizes a 6-layer stackup. One benefit with this winding technique is that the repeated 2-layer coil pattern naturally allows both the input and return terminals to end on the outer diameter of the PCB. This

126
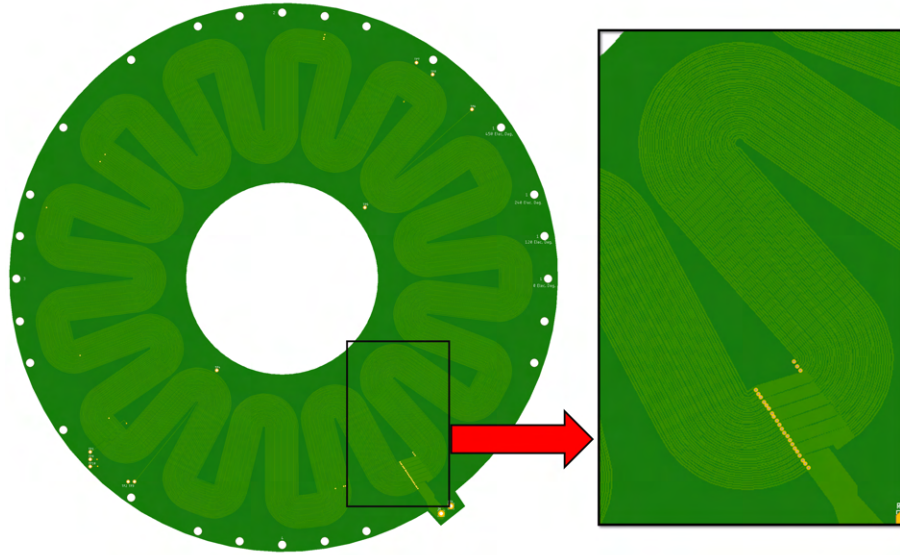
Figure 5.15: Electronic computer-aided design (ECAD) rendering of the proposed wave winding PCB stator. Board has 1 return layer and 5 active layers with a total thickness of 1mm. Seven turns of six parallel traces per active layer are connected in series.

eliminates the need for a layer to be used as a return path and all 6 of the layers may use active copper. The coil shape used in the design and development of this prototype has a coil width, w_c, of 20mm and a coil length, l_c, of 30mm. Each coil contains 27 loops of traces with 8mil and 10mil for w_t and w_i respectively. For this prototype, the t_t is 0.139mm, which corresponds to $4oz/ft^2$. As in the wave winding design, the PCB was designed using ECAD software (Fig. 5.16).

With respect to the input terminal on the top layer of the board, a complete coil with 27 loops is created, the trace then is located on the coil's inner-side. At this position, a via transitions the connection from an odd numbered layer to an even layer. The same coil winding direction is then continued until the trace reaches

127

the outer diameter of the active portion of the stator at end of the last loop. A via is then used to repeat the pattern on to the next layer. By constraining the total layer count to an even number, the traces may easily be brought out to the return terminal without a dedicated return path layer, as seen in the wave winding PCB. This maximizes the layers with active copper, and subsequently, increases the equivalent fill factor of the stator. Input and return bus bars are included along the circumference to connect the windings and ensure opposite polarity between adjacent coils. Additionally, a great advantage of the spiral winding design is that because all traces are connected in series, the circulating currents are greatly reduced. The winding pattern implemented for this wave PCB stator design is further detailed in Fig. 5.17.

5.7 Demonstrator of a Coreless AFPM Machine with PCB Stators

Design, simulation, and prototyping has been conducted for variations of PCB stator topologies for a 26-pole, coreless AFPM machine with dual rotors (Fig. 5.20 and Fig. 5.21). The first of these utilizes a spiral-type winding as shown in Fig. 5.10, with trace width and isolation of 8mil and 10mil, respectively. A single PCB uses 6-layers, all of which are in series using vias located at the interior and exterior of the coil to connect adjacent layers. The second is a wave-type winding with the same
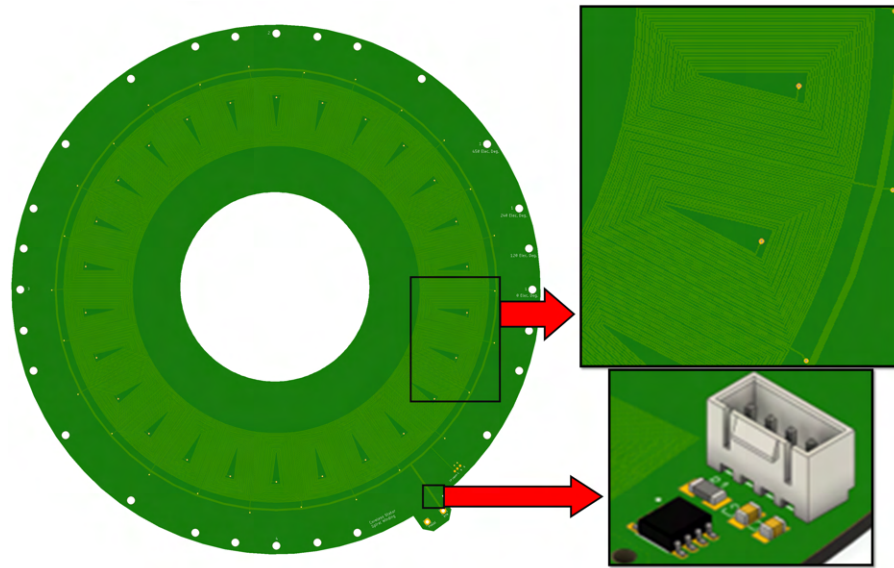
Figure 5.16: Electronic computer-aided design (ECAD) rendering of the proposed spiral winding PCB stator. In this design, 27 loops per coil are used and series connections between layers are achieved by vias. Integrated current, voltage, and temperature sensing is achievable with a PCB stator.
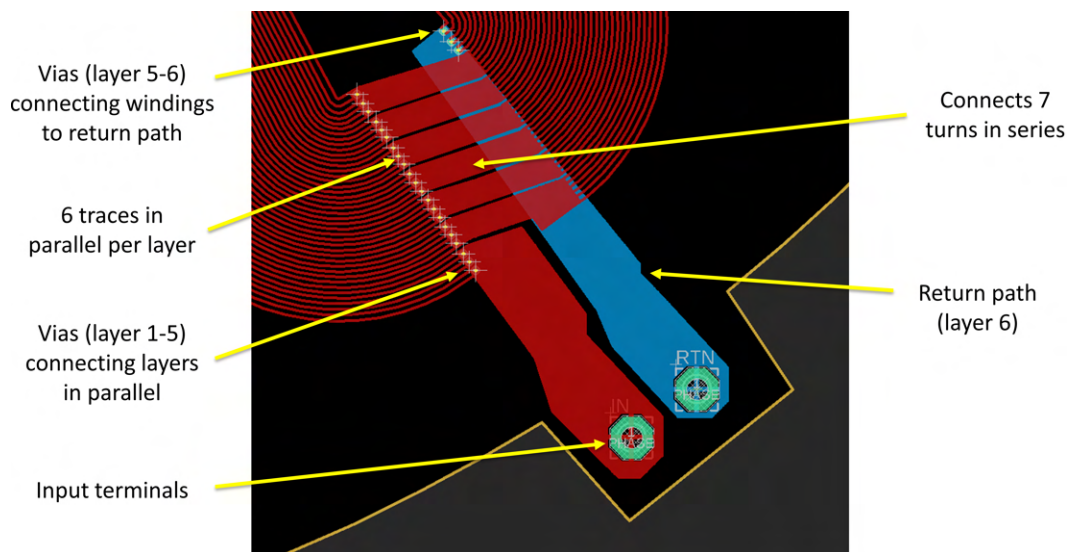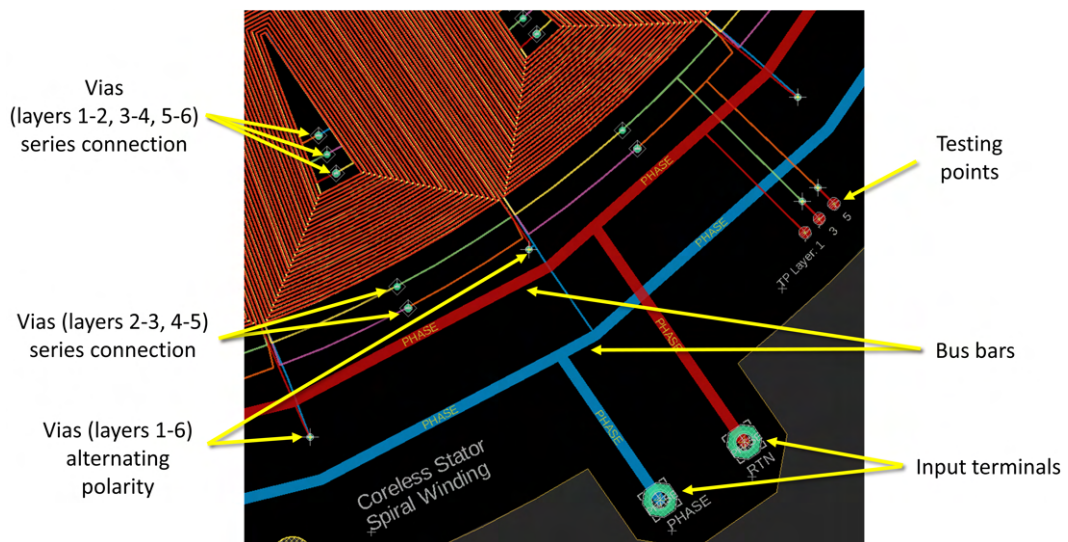

Figure 5.17: Illustration of the printed circuit board (PCB) winding implementation for the proposed spiral winding stator.
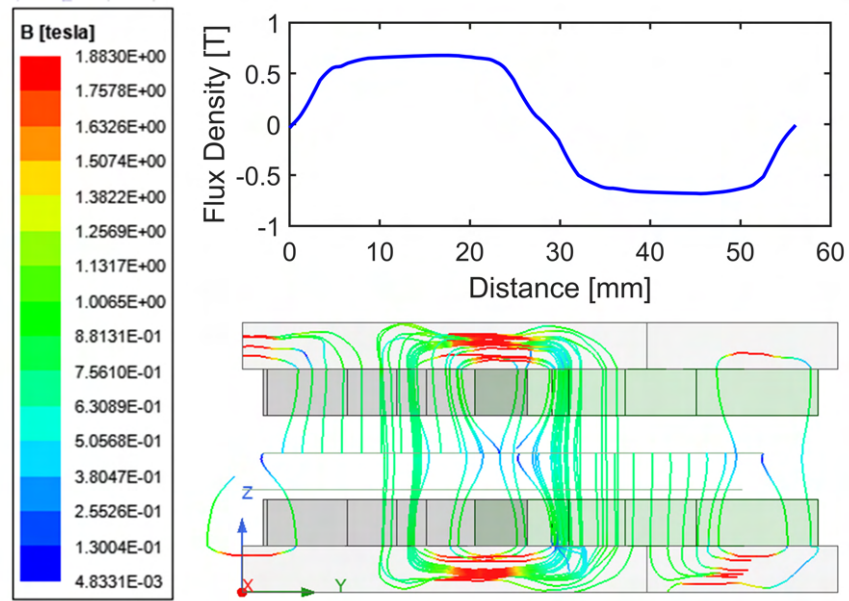
Figure 5.18: Two dimensional side view of the prototype 26-pole dual rotor design with flux density vectors shown (bottom). Flux density observed along the length of an arc located at the center of the airgap (top).
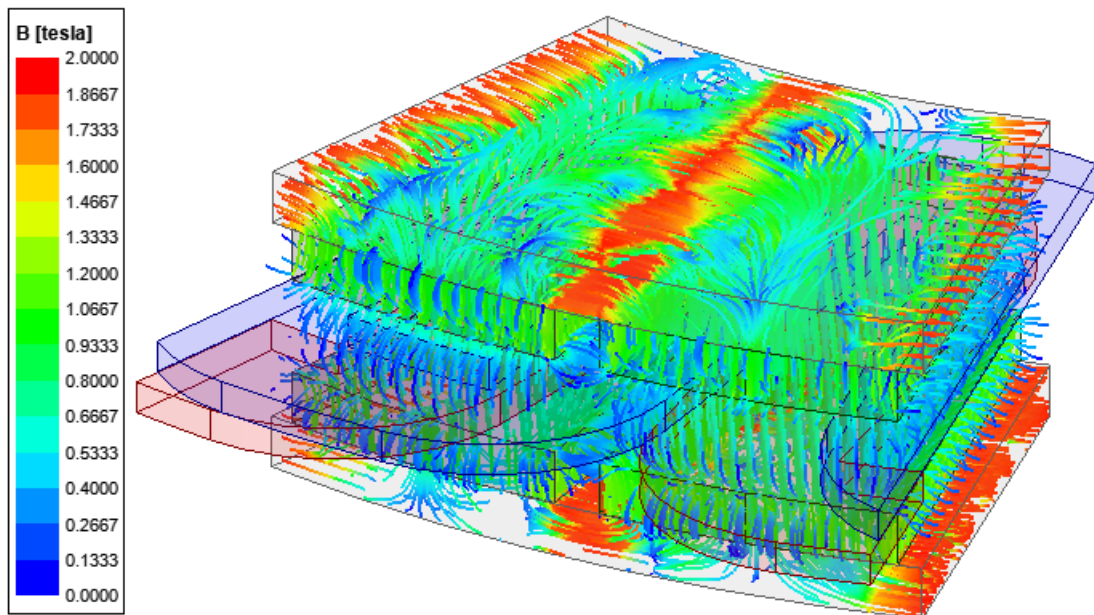
Figure 5.19: Three dimensional view of the magnetic flux density of the prototype 26-pole, dual rotor design with a two-phase wave winding stator under loaded conditions.
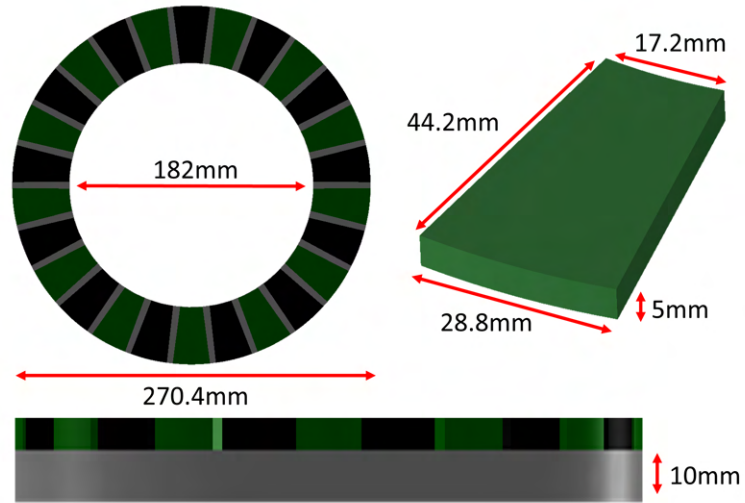
Figure 5.20: Geometric dimensions of a single 26-pole rotor used in the FEA analysis and for experimental studies.
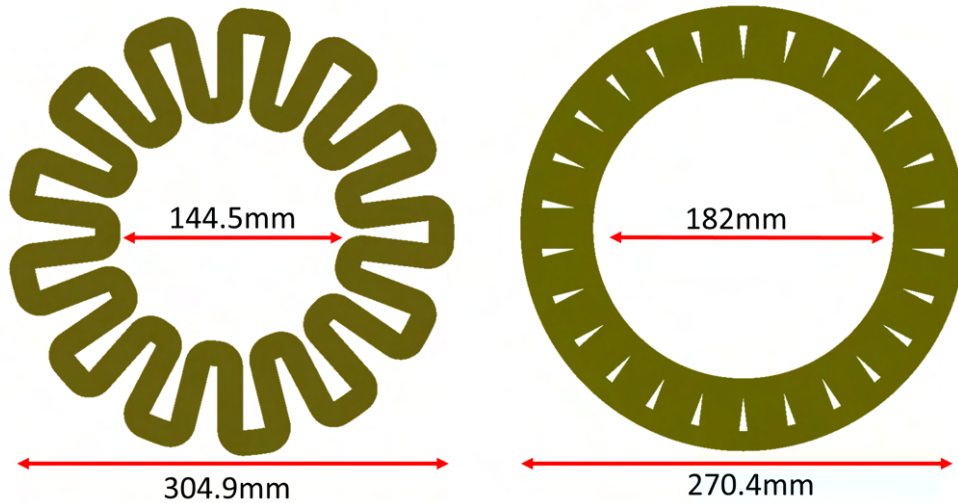
Figure 5.21: Inner and outer diameter of both proposed PCB stator windings. (left) Wave winding machine exhibits end windings past the rotor magnet OD, leading to a greater active stator OD, when compared to the spiral winding stator (right).

trace width and isolation. The wave-winding PCB also uses 6-layers, with a parallel connection by means of vias. Both of the mentioned stators use the same 26-pole dual rotor and the main dimensions of the components are shown in Table 5.2.

The prototype machine stator board was designed in AutoDesk EAGLE ECAD software and produced as a set of modular PCBs to be stacked, connected in parallel or series depending on desired machine voltage and current ratings. Phasing of the machine is achieved by angular displacement of each phase module for the appropriate electric degrees offset. Mounting holes were included on the outer diameter of the PCB stator to allow angular displacement for 120 elec. degrees offsets, used in a three phase machine, or 90 electrical degrees offset for a two phase configuration.

Analytical equations (5.3 and 5.4), along with finite element analysis were used to estimate both the wave and spiral winding stator parameters once the designs were completed, resulting in the values seen in Table 5.3. These parameters were also experimentally measured for the wave winding stator, which has been constructed.

To evaluate the prototype's performance, a mechanical testing fixture has been constructed to accommodate various stator configurations and alternate PCB stators, as shown in Fig. 5.24. Axial-flux machines are particularly difficult to assemble, considering the substantial axial force, in this case, between the dual rotors. A non-ferrous spacer was created to set the airgap between the rotors. To assemble the machine, a single rotor is attached to the shaft and fixed in place, along with the airgap

Table 5.2: Main Design Data for Prototype PCB Coreless AFPM Machines.

Rotor	
Rotor OD [mm]	270.4
Rotor ID [mm]	182
Pole Pitch at ID [mm]	17.2
Pole Pitch at OD [mm]	28.8
Magnet Thickness [mm]	5
Back iron Thickness [mm]	10
Wave Winding PCB Stator	
Stator ID [mm]	144.5
Stator OD [mm]	304.9
Active layers	5
Trace width/isolation, w_t/w_i [mil]	8/10
Trace thickness, t_t [mm]	0.07
Trace length [m]	8
Spiral Winding PCB Stator	
Stator ID [mm]	1182
Stator OD [mm]	270.4
Active layers	6
Trace width/isolation, w_t/w_i [mil]	8/10
Trace thickness, t_t [mm]	0.14
Trace length [m]	14

Table 5.3: Prototype Machine Parameters.

Wave Winding PCB Stator	
Phase Resistance [Ω]	0.84 (calc.)
	0.89 (meas.)
Phase Inductance [μH]	30.4 (calc.)
	34.7 (meas.)
k_e [V/krpm]	54.1 (calc.)
	54.3 (meas.)
Spiral Winding PCB Stator	
Phase Resistance [Ω]	0.82 (calc.)
Phase Inductance [μH]	52.4 (calc.)

spacer. The PCB stator is then freely placed over the shaft and temporarily attached to the first rotor. A rotor attachment and removal tool was specially constructed to allow precise, controlled axial displacement of the second rotor. The tool attaches to the flange mount shaft collar, which connects the rotor to the shaft, and uses a lead screw against the center of the shaft to slowly raise or lower the second rotor. Once the second rotor is in position, it is locked into place. The rotor, stator, and shaft assembly is then inserted into the testing fixture through the bearings and the stator is mounted using nylon spacer and tapped holes in the fixture.

The conditions of the experiment and simulation were set to have comparative studies, with two phases and a magnetic airgap of 7mm between the rotors in an open-circuit configuration. A prime mover was then attached to the machine's shaft and used to rotate the machine up to a speed of 3050rpm. An oscilloscope was used to record the induced back emf in one of the phases and compared to the simulated results (Fig. 5.25). A fast Fourier transform was conducted on both the experimental and simulated back EMF to evaluate the magnitude of the fundamental and harmonic components. As shown in Table 5.4, the simulated back EMF waveform contains significant contributions from the third and fifth harmonics. The FEA model of the wave winding machine does not consider magnet skew, which is present in the prototype rotor and requires further investigation.

The test setup previously described was then connected to a resistive load of 6.5

Table 5.4: Harmonic content in the simulated and experimental wave winding PCB back EMF. Experimental values are highlighted in bold.

Harmonic Order	1	3	5	7	9
Simulated Voltage [V]	165.1	12.2	3.1	0.2	0.9
Experimental Voltage [V]	**175.3**	**2.0**	**0.6**	**0.1**	**0.1**

Ohms per phase. A prime mover was used to drive the generator up to speeds that produce significant current in the windings. At 5A, the current density seen in the stator windings was approximately $6A/mm^2$. The output currents of the machine were measured and are presented in Fig. 5.26. As this test was performed, a thermal imaging camera captured the temperature at thermal steady state of the machine windings before and after operation (Fig. 5.27).

5.8 Summary

High power density, efficient electric machines are critical for enabling electrification of aviation propulsion. This chapter has presented a review of coreless and slotless machine designs with a focus on electric aircraft applications. The requirements that electric machines used for propulsion must meet have been addressed. Additionally, design considerations and analytical performance estimates for coreless machines that utilize PCB stators were discussed. Prototype PCB stators have been designed and produced for a coreless, 26-pole, AFPM machine and experimental results are presented.
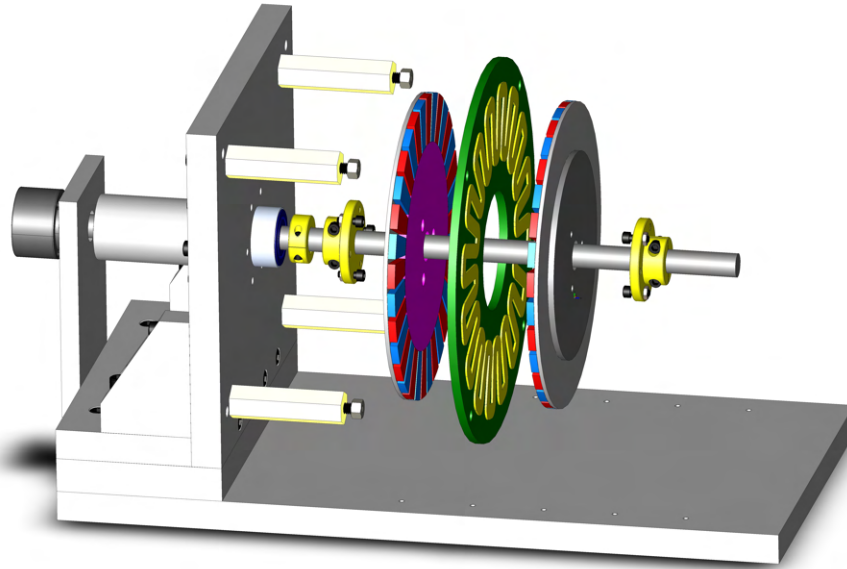
Figure 5.22: Exploded view of the computer-aided design (CAD) model for the proposed dual rotor AFPM machine on a testing fixture. The machine is shown with a conceptual wave winding PCB stator.
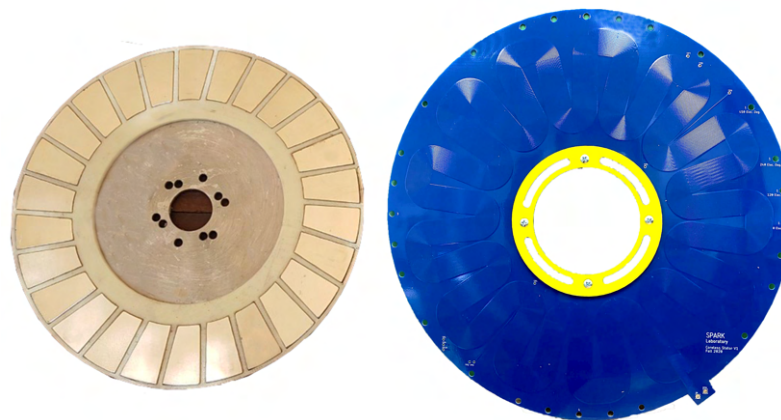
Figure 5.23: 26-pole AFPM rotor with NdFeB magnets, steel back plate, and 3D printed magnet retainer (left). The rotor is attached to a flange-mount shaft collar using the holes shown toward the center. Prototype wave winding PCB stator with 13 waves and 3D printed clamping ring on the ID used to increase rigidity (right).
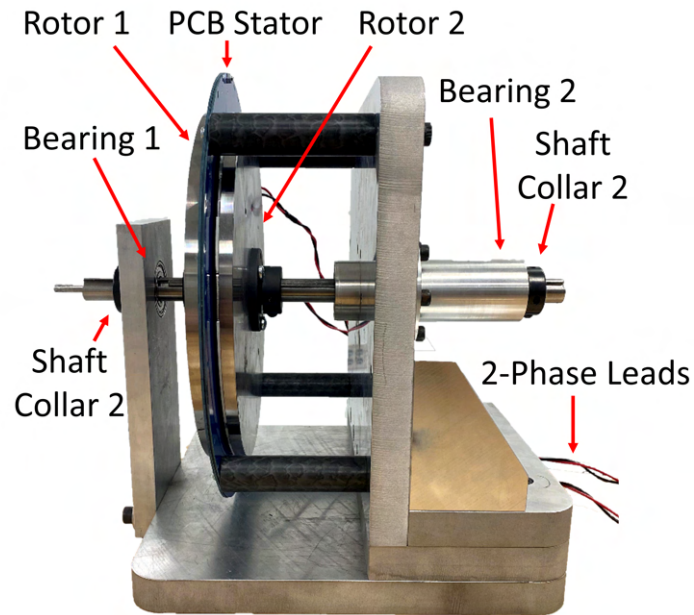
Figure 5.24: Newly developed coreless AFPM machine on experimental test fixture. The setup shown includes the dual rotor configuration with a two-phase wave winding PCB stator, consisting of (4) 1mm, 6-layer boards.
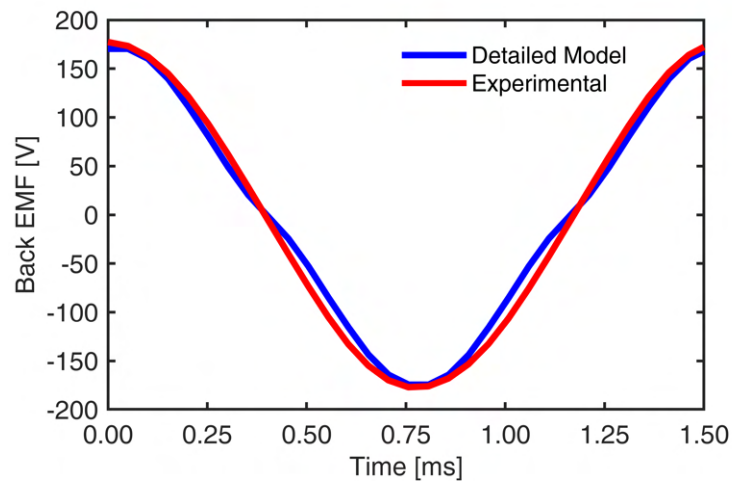
Figure 5.25: Simulated and experimental open-circuit back EMF at 3050rpm. The wave winding machine tested utilizes (4) PCBs, comprising 2-phases.
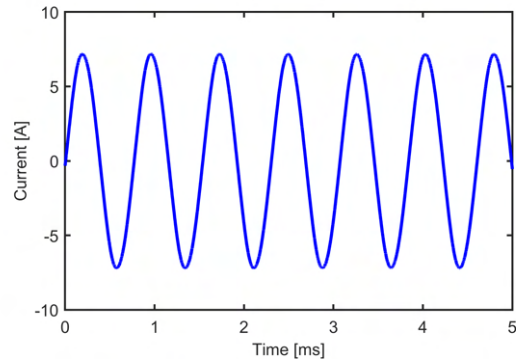
Figure 5.26: Output current of the prototype machine operating as an uncontrolled generator feeding a purely resistive load of 6.5 Ω.
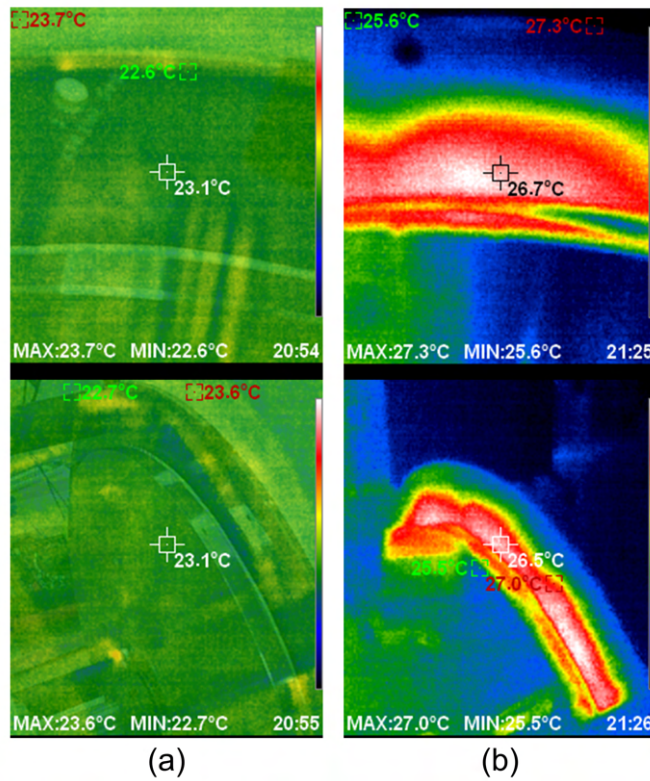
Figure 5.27: Temperature distribution on the prototype wave winding PCB stator under a loaded condition as a generator feeding a load with currents shown in Fig. 5.26. Top images show a single wave, while the bottom show a more complete view of the machine. Measurements were taken prior to operation (a) and after the machine was operated at a current density of 6 A/mm^2 for 5 minutes (b).

Chapter 6

Conclusions

6.1 Summary and Conclusions

A novel approach using graph theory for designing electric aircraft power systems for turbo-electric, hybrid-electric, and all-electric aircraft was introduced in chapter 2. The software developed employs input from the user for mission characteristics, such as a flight profile, fuel savings goals, and component ratings. The developed software framework enables the analysis of over a thousand potential design candidates, determining each topology's performance in with respect to specific metrics. Data for mass, overall and component efficiencies, and reliability provide the user with early design stage insights into which topologies are best suited to their application.

In chapter 3, a software framework for the co-simulation of electric aircraft has been proposed. This was demonstrated on an electric airplane with similar ratings to the X-57 Maxwell, currently under development by NASA. The case study examines operation over a mission profile, which includes an emergency situation, when a pilot

must redirect their destination due to restrictions at the intended airport. Simulation results include calculations for various flight dynamics, such as aircraft speed and orientation, endurance via battery state of charge, motor currents, and power electronic characteristics during periods of transition. Detailed results for the power electronic converters are derived using data fed back from the long time constant simulation of the aerodynamics with average models for the power system. The power electronic transient calculations may be used to evaluate filter designs, system ratings, thermal management systems, and efficiency.

In response to the trend toward use of low inductance PMSMs in electric airplanes due to their high power density, a new method for extended speed operation has been introduced in chapter 4 to solve the challenges originating from the limited field weakening region. A review of alternative techniques has been provided, in addition to simulation results for the proposed current weakening technique. These studies have been expanded to implement the method on an example solar electric race car with a triple-port bi-directional converter. An experimental validation of the technique has also been presented.

Chapter 5 covers the design and development of coreless AFPM machines with PCB stators has been discussed in chapter 5. Two variations of stator winding implementation have been proposed and studied: a wave and spiral winding, both of which utilize dual, permanent magnet rotors. The performance of both the wave and

spiral winding machines has been simulated using electromagnetic FEA, with detailed trace-by-trace models. Additionally, a prototype wave winding stator with 13 waves has been produced, tested, and served for satisfactory validation.

6.2 Original Contributions

The main original contributions of this dissertation may be best summarized as follows:

1. Graph theory-based method for the multi-objective optimization of electric aircraft power systems (EAPS) topologies. The developed algorithms and software framework allow system designers to establish the initial design based on thousands of candidate designs. The optimization method employed component data based on an extensive literature and publicly available information survey and evaluated each topology based on performance metrics including efficiency, total mass, and survivability. (Chapter 2)

2. A co-simulation software framework for multi-physics evaluation of EAPS architectures and electrical components, as well as airframe, propellers and associated aerodynamics has been developed. Novelty lies in the proposed decoupling method, which leads to reduction of effective simulation times, while maintaining satisfactory accuracy and detail. (Chapter 3)

3. A method to extend the constant power speed range of low inductance permanent magnet synchronous machines based on the weakening of the stator current, as opposed to the traditional method of flux weakening. Simulation and laboratory experimentation demonstrates that the method is applicable in principle for the propulsion motors of electric aircraft, which typically require only 30 percent increase in speed over the base value. (Chapter 4)

4. Design, advanced detailed electromagnetic finite element analysis, prototyping and testing of coreless AFPM machines with PCB stators. Research comprised two PCB winding patterns, one of the wave type and the other spiral winding. Feasibility was investigated for aircraft propulsion applications by computationally scaling the lab designs for higher power rating. (Chapter 5).

6.3   Recommendations for Future Work

Based on the progress of the dissertation research, anticipated and recommended further work includes:

1. Extension of the proposed graph theory approach for the optimization of EAPS. The software developed considers system mass, fuel consumption, and efficiency. Further work may include functionality to estimate overall architecture reliability, and based on this, case studies for multiple aircraft with diverse mission objectives may be performed.

2. Calibration of the coreless machine FEA models may be conducted to include the magnet skew as seen in the delivered prototype and effects on the motor performance should be evaluated.

3. Detailed analysis of the winding losses in the spiral and wave winding coreless AFPM machine designs should be considered. Furthermore, systematic experimental procedures may be developed and executed for testing of the supplementary eddy current losses.

4. A spiral winding prototype has been designed, ordered, and is awaiting delivery. Open-circuit back EMF testing and parameter measurement should take place upon arrival. Additionally, the prototype should be tested as a generating and motoring situations.

5. The ongoing development of a two-phase motor drive and associated controls for further testing of the prototype coreless machines should be completed.

6. Further experimentation and validation of the current weakening technique with the testing setup discussed in Chapter 4 should be performed. The test fixture should include an inline torque transducer for detailed and precise measurements.

References

[1] "Nasa n3-x with turboelectric distributed propulsion." [Online]. Available: https://ntrs.nasa.gov/search.jsp?R=20150002081

[2] Zephyr – the high altitude pseudo-satellite. [Online]. Available: http://www.airbus.com/defence/uav/zephyr.html

[3] S. Clarke, M. Redifer, K. Papathakis, A. Samuel, and T. Foster, "X-57 power and command system design," in *2017 IEEE Transportation Electrification Conference and Expo (ITEC)*, June 2017, pp. 393–400.

[4] J. Felder, "Nasa n3-x with turboelectric distributed propulsion," NASA Glenn Research Center, Tech. Rep., November 2014. [Online]. Available: https://ntrs.nasa.gov/search.jsp?R=20150002081

[5] "Compact, quiet, low-vibration, high-efficiency rotary engines," 2018. [Online]. Available: https://liquidpiston.com/wp-content/uploads/2018/07/LiquidPiston-X-Specifications-2018-05-14-3.pdf

[6] "Zoche aero-diesels," 2000. [Online]. Available: http://www.zoche.de/specs.html

144

[7] "Cd-200 jet-a enginer series," 2020. [Online]. Available: http://www.continentalmotors.aero/uploadedFiles/Content/Engines/Diesel_Engines/CD200-SpecSheet.pdfl

[8] "Helicopters." [Online]. Available: https://www.rolls-royce.com/products-and-services/civil-aerospace/helicopters

[9] "Helicopter engines," 2019. [Online]. Available: https://www.pwc.ca/en/products-and-services/products/helicopter-engines

[10] "Engines," 2020. [Online]. Available: https://aerospace.honeywell.com/en/learn/products/engines

[11] "Gemini diesel engines." [Online]. Available: https://www.geminidiesel.aero/application/files/5014/2828/3029/GEMINI_GenInfoSht_LowRez.pdf

[12] "Electric motor demonstrator sets two world records in two hours after five years of work," Nov 2019. [Online]. Available: https://car.osu.edu/news/2019/11/electric-motor-demonstrator-sets-two-world-records-two-hours-after

[13] A. K. Yoon, D. Lohan, F. Arastu, J. Xiao, and K. Haran, "Direct drive electric motor for starc-abl tail-cone propulsor," *AIAA Propulsion and Energy 2019 Forum*, 2019.

[14] "Electric propulsion components with high power densities for aviation," 2015. [Online]. Available: https://nari.arc.nasa.gov/sites/default/files/attachments/Korbinian-TVFW-Aug2015.pdf

[15] R. W. Dyson, R. H. Jansen, K. P. Duffy, and P. J. Passe, "High efficiency megawatt machine rotating cryocooler conceptual design," in *2019 AIAA/IEEE Electric Aircraft Technologies Symposium (EATS)*, 2019, pp. 1–15.

[16] "Yasa 750r," 2018. [Online]. Available: https://www.yasa.com/yasa-750/

[17] "Yasa p400r," 2018. [Online]. Available: https://www.yasa.com/yasa-400/

[18] "1 megawatt power generator," 2019. [Online]. Available: https://aerospace.honeywell.com/content/dam/aero/en-us/documents/learn/products/electric-power/brochures/N61-2229-000-000_1MW-Generator-br.pdf

[19] X. Zhang, C. L. Bowman, T. C. O'Connell, and K. S. Haran, "Large electric machines for aircraft electric propulsion," *IET Electric Power Applications*, vol. 12, no. 6, pp. 767–779, 2018.

[20] "E-motor," 2019. [Online]. Available: https://www.mclaren.com/applied/products/item/e-motor-120kw-130nm/

[21] A. Yoon, Xuan Yi, J. Martin, Yuanshan Chen, and K. Haran, "A high-speed, high-frequency, air-core pm machine for aircraft application," in *2016 IEEE Power and Energy Conference at Illinois (PECI)*, 2016, pp. 1–4.

[22] H. Lin, H. Guo, and H. Qian, "Design of high-performance permanent magnet synchronous motor for electric aircraft propulsion," in *2018 21st International Conference on Electrical Machines and Systems (ICEMS)*, 2018, pp. 174–179.

[23] "Hvh410-150 electric motor," 2016. [Online]. Available: https://cdn.borgwarner.com/docs/default-source/default-document-library/remy-pds---hvh410-150-sheet-euro-pr-3-16.pdf?sfvrsn=a642cd3c_11

[24] Z. Zhang, W. Geng, Y. Liu, and C. Wang, "Feasibility of a new ironless-stator axial flux permanent magnet machine for aircraft electric propulsion application," *CES Transactions on Electrical Machines and Systems*, vol. 3, no. 1, pp. 30–38, 2019.

[25] "Emrax 348," 2020. [Online]. Available: https://emrax.com/e-motors/emrax-348/

[26] ""magnidrive"," 2020. [Online]. Available: https://www.magnix.aero/products

[27] "High performance electric motors and drives," "accessed Sept. 10, 2020". [Online]. Available: https://www.mclaren.com/applied/case-study/relentless-drive-power-density-and-efficiency/

[28] "Cascadia motion - inverters," "accessed Sept. 10, 2020". [Online]. Available: https://www.cascadiamotion.com/inverters

[29] *High Voltage Low Power Inverter*, Borg Warner, 2019, hVLP-10, HVLP-20.

[30] "Yasa controllers," "accessed Sept. 10, 2020". [Online]. Available: https://www.yasa.com/controllers/

[31] D. Zhang, J. He, D. Pan, M. Dame, and M. Schutten, "Development of megawatt-scale medium-voltage high efficiency high power density power converters for aircraft hybrid-electric propulsion systems," in *2018 AIAA/IEEE Electric Aircraft Technologies Symposium (EATS)*, 2018, pp. 1–5.

[32] M. Garrett, D. Avanesian, M. Granger, S. Kowalewski, J. Maroli, W. Miller, R. Jansen, and P. Kascak, "Development of an 11 kw lightweight, high efficiency motor controller for nasa x-57 distributed electric propulsion using sic mosfet switches," in *2019 AIAA/IEEE Electric Aircraft Technologies Symposium (EATS)*, 2019, pp. 1–8.

[33] T. M. Indra Mahila, A. Jannifar, and M. Heikal Hasan, "Review of available methods and development on energy storage; technology update," *Renewable and Sustainable Energy Reviews*, vol. 33, no. 1, pp. 532–545, 2014.

[34] M. Farhadi and O. Mohammed, "Energy storage technologies for high-power applications," *IEEE Transactions on Industry Applications*, vol. 52, no. 3, pp. 1953–1961, 2016.

[35] T. Kadyk, C. Winnefeld, R. Hanke-Rauschenbach, and U. Krewer, "Analysis and design of fuel cell systems for aviation," *Energies*, vol. 11, no. 2, p. 375, Feb 2018. [Online]. Available: http://dx.doi.org/10.3390/en11020375

[36] Y. Gibbs, "Nasa armstrong fact sheet: Nasa x-57 maxwell," Sep 2018. [Online]. Available: https://www.nasa.gov/centers/armstrong/news/FactSheets/FS-109.html

[37] A. Turevskiy, S. Gage, and C. Buhr, "Model-based design of a new light-weight aircraft," in *AIAA Modeling and Simulation Technologies Conference and Exhibit*, 2007.

[38] G. Sizov, "Design synthesis and optimization of permanent magnet synchronous machines based on computationally-efficient finite element analysis," 2013.

[39] R. J. Hill-Cottingham, P. C. Coles, J. F. Eastham, F. Profumo, A. Tenconi, and G. Gianolio, "Multi-disc axial flux stratospheric aircraft propeller drive," in *Conference Record of the 2001 IEEE Industry Applications Conference. 36th IAS Annual Meeting (Cat. No.01CH37248)*, vol. 3, 2001, pp. 1634–1639 vol.3.

[40] F. Profumo, A. Tenconi, M. Cerchio, J. F. Eastham, and P. C. Coles, "Axial flux plastic multi-disc brushless pm motors: performance assessment," in *Nineteenth Annual IEEE Applied Power Electronics Conference and Exposition, 2004. APEC '04.*, vol. 2, 2004, pp. 1117–1123 vol.2.

[41] X. Wang, C. Hu, M. Zhao, L. Wu, and S. Zhou, "Design of multi-layer pcb core-less axial permanent magnet synchronous motor," in *2019 22nd International Conference on Electrical Machines and Systems (ICEMS)*, 2019, pp. 1–4.

[42] D. Gambetta and A. Ahfock, "Designing printed circuit stators for brushless permanent magnet motors," *IET Electric Power Applications*, vol. 3, no. 5, pp. 482–490, 2009.

[43] N. Kurita, R. Inomata, W. Gruber, and T. Okayasu, "Examination of flex pcb configuration for a winding of a magnetic levitation motor," in *2020 23rd International Conference on Electrical Machines and Systems (ICEMS)*, 2020, pp. 1655–1658.

[44] F. Marignetti, G. Volpe, S. M. Mirimani, and C. Cecati, "Electromagnetic design and modeling of a two-phase axial-flux printed circuit board motor," *IEEE Transactions on Industrial Electronics*, vol. 65, no. 1, pp. 67–76, 2018.

[45] M. Caujolle. Airbus, rolls-royce, and siemens team up for electric future partnership launches e-fan x hybrid-electric flight demonstrator. [Online]. Available: http://www.airbus.com/newsroom/press-releases/en/2017/11/airbus--rolls-royce--and-siemens-team-up-for-electric-future-par.html

[46] Alice commuter. [Online]. Available: https://www.eviation.co/alice/

[47] Airbus group: E-fan the new way to fly. [Online]. Available: company.airbus.com/service/mediacenter

[48] Technical challenges. [Online]. Available: http://aroundtheworld.solarimpulse.com/adventure

[49] B. C. Mecrow, J. W. Bennett, A. G. Jack, D. J. Atkinson, and A. J. Freeman,

"Drive topologies for solar-powered aircraft," *IEEE Transactions on Industrial Electronics*, vol. 57, no. 1, pp. 457–464, Jan 2010.

[50] P. Oettershagen, A. Melzer, T. Mantel, K. Rudin, T. Stastny, B. Wawrzacz, T. Hinzmann, S. Leutenegger, K. Alexis, R. Siegwart, and et al., "Design of small hand-launched solar-powered uavs: From concept study to a multi-day world endurance record flight," *Journal of Field Robotics*, vol. 34, no. 7, p. 1352–1377, 2017.

[51] M. Armstrong, M. Blackwelder, A. Bollman, C. Ross, A. Campbell, C. Jones, and P. Norman, "Architecture, voltage, and components for a turboelectric distributed propulsion electric grid," NASA Glenn Research Center, Tech. Rep., 2015.

[52] D. Lawhorn, V. Rallabandi, and D. M. Ionel, "Scalable graph theory approach for electric aircraft power system optimization," in *2019 AIAA/IEEE Electric Aircraft Technologies Symposium (EATS)*, August 2019, pp. 1–5.

[53] J. J. Scheidler and T. F. Tallerico, "Design, fabrication, and critical current testing of no-insulation superconducting rotor coils for nasa's 1.4 mw high-efficiency megawatt motor," in *2018 AIAA/IEEE Electric Aircraft Technologies Symposium (EATS)*, July 2018, pp. 1–9.

[54] D. Zhang, J. He, D. Pan, M. Dame, and M. Schutten, "Development of megawatt-scale medium-voltage high efficiency high power density power converters for aircraft hybrid-electric propulsion systems," in *2018 AIAA/IEEE Electric Aircraft Technologies Symposium (EATS)*, July 2018, pp. 1–5.

[55] "E-fan," "April 30, 2014, accessed Sept. 10, 2020". [Online]. Available: https://newatlas.com/e-fan-airbus-electric-plane/31823/

[56] "Magnix," "June 8, 2020, accessed Sept. 10, 2020". [Online]. Available: https:// www.thenakedscientists.com/articles/interviews/all-electric-plane-takes-flight

[57] "E-fan x," "accessed Sept. 10, 2020". [Online]. Available: https://www.airbus. com/innovation/zero-emission/electric-flight/e-fan-x.html#ove

[58] J. L. Kratz and G. L. Thomas, "Dynamic analysis of the starc-abl propulsion system," *AIAA Propulsion and Energy 2019 Forum*, 2019.

[59] M. J. Armstrong, C. A. H. Ross, M. J. Blackwelder, and K. Rajashekara, "Propulsion system component considerations for nasa n3-x turboelectric distributed propulsion system," *SAE International Journal of Aerospace*, vol. 5, no. 2, p. 344–353, 2012.

[60] M. A. Hannan, M. M. Hoque, A. Hussain, Y. Yusof, and P. J. Ker, "State-of-the-art and energy management system of lithium-ion batteries in electric vehicle applications: Issues and recommendations," *IEEE Access*, vol. 6, pp. 19 362–19 378, 2018.

[61] C. E. Jones, P. J. Norman, S. J. Galloway, M. J. Armstrong, and A. M. Bollman, "Comparison of candidate architectures for future distributed propulsion aircraft," *IEEE Transactions on Applied Superconductivity*, vol. 26, no. 6, pp. 1–9, Sep. 2016.

[62] M. J. Armstrong, M. Blackwelder, A. Bollmann, C. Ross, A. Campbell, C. Jones, and P. Norman, "Architecture, Voltage, and Components for a Turboelectric Distributed Propulsion Electric Grid," Rolls-Royce and Georgia Institute of Technology and University of Strathclyde, Tech. Rep., July 2015.

[63] J. C. Gladin, D. Trawick, C. Perullo, J. C. Tai, and D. N. Mavris, "Modeling

and design of a partially electric distributed aircraft propulsion system with GT-HEAT," *55th AIAA Aerospace Sciences Meeting*, 2017.

[64] H. Smith, D. Sziroczák, G. Abbe, and P. Okonkwo, "The GENUS aircraft conceptual design environment," *Proceedings of the Institution of Mechanical Engineers, Part G: Journal of Aerospace Engineering*, vol. 233, no. 8, p. 2932–2947, 2018.

[65] N. Chen, H. Wang, H. Li, and D. Xu, "Generic derivation of optimal architecture for a resilient microgrid with graph theory," in *2019 IEEE 10th International Symposium on Power Electronics for Distributed Generation Systems (PEDG)*, 2019, pp. 359–364.

[66] T. A. Trapp, "Shipboard integrated engineering plant survivable network optimization," Ph.D. dissertation, Massachusettes Institute of Technology, 2015.

[67] D. Lawhorn, V. Rallabandi, and D. M. Ionel, "A network graph technique for the design of electric aircraft power systems," in *2020 IEEE Transportation Electrification Conference Expo (ITEC)*, 2020, pp. 809–813.

[68] E. R. Laithwaite, "The goodness of a machine," *Electronics and Power*, vol. 11, no. 3, pp. 101–103, 1965.

[69] R. Rodrigues, Y. Du, A. Antoniazzi, and P. Cairoli, "A review of solid-state circuit breakers," *IEEE Transactions on Power Electronics*, vol. 36, no. 1, pp. 364–377, 2021.

[70] D. Lawhorn, V. Rallabandi, and D. M. Ionel, "Scalable graph theory approach for electric aircraft power system optimization," in *2019 AIAA/IEEE Electric Aircraft Technologies Symposium (EATS)*, August 2019, pp. 1–5.

[71] Y. Zhao, Y. Che, T. Lin, C. Wang, J. Liu, J. Xu, and J. Zhou, "Minimal cut sets-based reliability evaluation of the more electric aircraft power system," *Mathematical Problems in Engineering*, vol. 2018, 2018.

[72] H.-J. Steiner, P. Vratny, C. Gologan, K. Wieczorek, A. Isikveren, and M. Hornung, "Optimum number of engines for transport aircraft employing electrically powered distributed propulsion," *CEAS Aeronautical Journal*, vol. 5, pp. 157–170, 06 2014.

[73] D. Lawhorn, V. Rallabandi, and D. M. Ionel, "Electric aircraft system co-simulation including body, propeller, propulsion, and energy storage models," in *2019 IEEE Transportation Electrification Conference and Expo (ITEC)*, 2019, pp. 1–5.

[74] H. D. Kim, A. Perry, and P. J. Ansell, "A review of distributed electric propulsion concepts for air vehicle technology," in *2018 AIAA/IEEE Electric Aircraft Technology Symposium (EATS)*, 2018, pp. 1–21.

[75] A. Lundbladh and T. Grönstedt, "Distributed propulsion and turbofan scale effects," 2005.

[76] B. B. Choi, "Propulsion powertrain simulator: Future turboelectric distributed-propulsion aircraft." *IEEE Electrification Magazine*, vol. 2, no. 4, pp. 23–34, Dec 2014.

[77] K. P. Duffy and R. H. Jansen, "Turboelectric and hybrid electric aircraft drive key performance parameters," in *2018 AIAA/IEEE Electric Aircraft Technologies Symposium (EATS)*, July 2018, pp. 1–19.

[78] C. Irimia, M. Grovu, C. Husar, D. Fodorean, and C. Antonya, "Co-simulation analysis for an electric vehicle powered by a high-speed electrical machine," in

2017 IEEE Vehicle Power and Propulsion Conference (VPPC), Dec 2017, pp. 1–6.

[79] V. Rallabandi, D. Lawhorn, D. M. Ionel, and X. Li, "Multi-physics modeling for electric and hybrid vehicles with in-wheel electric motors," in *2018 IEEE Transportation Electrification Conference and Expo (ITEC)*, June 2018, pp. 146–151.

[80] Q. Zhang, N. Cui, K. Li, Y. Shang, and C. Zhang, "Co-simulation of energy management strategy for hybrid electric vehicle in avl inmotion," in *2017 Chinese Automation Congress (CAC)*, Oct 2017, pp. 4932–4937.

[81] A. Filippone, Z. Mohamed-Kassim, and C. Buhr, "Multi-disciplinary simulation of propeller-turboprop aircraft flight," in *The Aeronautical Journal*, 2012, pp. 985–1014.

[82] V. Rallabandi, D. Lawhorn, J. He, and D. M. Ionel, "Current weakening control of coreless afpm motor drives for solar race cars with a three-port bi-directional dc/dc converter," in *2017 IEEE 6th International Conference on Renewable Energy Research and Applications (ICRERA)*, Nov 2017, pp. 739–744.

[83] N. Taran, V. Rallabandi, D. M. Ionel, and G. Heins, "A comparative study of coreless and conventional axial flux permanent magnet synchronous machines for low and high speed operation," in *2017 IEEE Energy Conversion Congress and Exposition (ECCE)*, Oct 2017, pp. 321–327.

[84] D. M. Ionel, J. F. Eastham, T. J. E. Miller, and E. Demeter, "Design considerations for permanent magnet synchronous motors for flux weakening applications," *IEE Proceedings - Electric Power Applications*, vol. 145, no. 5, pp. 435–440, Sep 1998.

[85] M. Boxriker, P. Winzer, J. Kolb, and M. Doppelbauer, "Increasing the operating range of permanent magnet synchronous motors by switching the winding configurations," in *2016 IEEE 2nd Annual Southern Power Electronics Conference (SPEC)*, Dec 2016, pp. 1–6.

[86] S. Hemmati and T. A. Lipo, "Field weakening of a surface mounted permanent magnet motor by winding switching," in *International Symposium on Power Electronics Power Electronics, Electrical Drives, Automation and Motion*, June 2012, pp. 736–740.

[87] T. Gerrits, C. G. E. Wijnands, J. J. H. Paulides, and J. L. Duarte, "Dual voltage source inverter topology extending machine operating range," in *2012 IEEE Energy Conversion Congress and Exposition (ECCE)*, Sept 2012, pp. 2840–2846.

[88] J. Kim, J. Jung, and K. Nam, "Dual-inverter control strategy for high-speed operation of ev induction motors," *IEEE Transactions on Industrial Electronics*, vol. 51, no. 2, pp. 312–320, April 2004.

[89] G. Heins, M. Thiele, D. Patterson, and N. Lambert, "Increase in operating range and efficiency for variable gap axial flux motors," in *2014 IEEE Energy Conversion Congress and Exposition (ECCE)*, Sept 2014, pp. 5870–5876.

[90] V. Rallabandi, N. Taran, and D. M. Ionel, "Multilayer concentrated windings for axial flux pm machines," *IEEE Transactions on Magnetics*, vol. 53, no. 6, pp. 1–4, June 2017.

[91] A. Yoon, J. Xiao, D. Lohan, F. Arastu, and K. Haran, "High-frequency electric machines for boundary layer ingestion fan propulsor," *IEEE Transactions on Energy Conversion*, vol. 34, no. 4, pp. 2189–2197, Dec 2019.

[92] I. Alphonse, S. H. Thilagar, and F. B. Singh, "Design of solar powered bldc motor driven electric vehicle," in *International Journal of Renewable Energy Research*, vol. 2, no. 3, Nov 2012, pp. 456–462.

[93] R. Hill-Cottingham, P. Coles, J. Eastham, F. Profumo, A. Tenconi, and G. Gianolio, "Multi-disc axial flux stratospheric aircraft propeller drive," *IEEE Industry Applications Conference*, vol. 3, pp. 1634–1639, 2001.

[94] M. Aydin, M. Gulec, Y. Demir, B. Akyuz, and E. Yolacan, "Design and validation of a 24-pole coreless axial flux permanent magnet motor for a solar powered vehicle," in *2016 XXII International Conference on Electrical Machines (ICEM)*, Sept 2016, pp. 1493–1498.

[95] R.-J. Wang, M. J. Kamper, K. V. der Westhuizen, and J. F. Gieras, "Optimal design of a coreless stator axial flux permanent-magnet generator," *IEEE Transactions on Magnetics*, vol. 41, no. 1, pp. 55–64, Jan 2005.

[96] A. Daghigh, H. Javadi, and H. Torakaman, "Considering wind speed characteristics in the design of a coreless afpm synchronous generator," in *International Journal of Renewable Energy Research*, vol. 6, no. 1, 2016, pp. 263–270.

[97] T. S. El-Hasan, "Development of axial flux permanent magnet generator for direct driven micro wind turbine," in *2016 IEEE International Conference on Renewable Energy Research and Applications (ICRERA)*, Nov 2016, pp. 169–172.

[98] I. Topaloglu, Y. Nakanishi, F. Korkmaz, and Y. Nakashima, "Axial flux permanent magnet generator with low cogging torque for maintenance free under water power generating system," in *International Journal of Renewable Energy Research*, vol. 6, no. 2, 2016, pp. 510–519.

[99] H. C. Lovatt, V. S. Ramsden, and B. C. Mecrow, "Design of an in-wheel motor for a solar-powered electric vehicle," *IEE Proceedings - Electric Power Applications*, vol. 145, no. 5, pp. 402–408, Sep 1998.

[100] M. C. Greaves, A. G. Simpson, B. D. Guymer, G. R. Walker, and D. A. Finn, "Ironless wheel motor for a direct drive vehicle application," in *Australasian Universities Power Engineering Conference, AUPEC'03*, R. Duke, Ed., University of Canterbury, Christchurch, New Zealand, 2003.

[101] S. Javadi and M. Mirsalim, "Design and analysis of 42-v coreless axial-flux permanent-magnet generators for automotive applications," *IEEE Transactions on Magnetics*, vol. 46, no. 4, pp. 1015–1023, April 2010.

[102] NuGen Mobility Inc., "SCM150-XXX axial flux, brushless pm motor specifications," Tech. Rep., 2007.

[103] C. Zhao, S. D. Round, and J. W. Kolar, "An isolated three-port bidirectional dc-dc converter with decoupled power flow management," *IEEE Transactions on Power Electronics*, vol. 23, no. 5, pp. 2443–2453, Sept 2008.

[104] N. Güler and E. Irmak, "Design and application of a novel single input multi output dc/dc converter," in *2016 IEEE International Conference on Renewable Energy Research and Applications (ICRERA)*, Nov 2016, pp. 1039–1045.

[105] J. He, T. Zhao, X. Jing, and N. A. O. Demerdash, "Application of wide bandgap devices in renewable energy systems – 2014; benefits and challenges," in *2014 International Conference on Renewable Energy Research and Application (ICRERA)*, Oct 2014, pp. 749–754.

[106] Q. Jiao, R. Hosseini, and R. M. Cuzner, "A comparison between silicon carbide based current source rectifier and voltage source rectifier for applications

in community dc microgrid," in *2016 IEEE International Conference on Renewable Energy Research and Applications (ICRERA)*, Nov 2016, pp. 544–549.

[107] W. Fu, Q. Jiao, R. Hosseini, R. Cuzner, and A. Lemmon, "Methodology for the volume minimization in non-isolated sic based pv inverters," in *2015 International Conference on Renewable Energy Research and Applications (ICRERA)*, Nov 2015, pp. 1236–1242.

[108] T. Salmi, M. Bouzguenda, A. Gastli, and A. Masmoudi, "Matlab/simulink based modeling of photovoltaic cell," *International Journal of Renewable Energy Research (IJRER)*, vol. 2, no. 2, pp. 213–218, 2012.

[109] M. A. Abdourrziq, M. Ouassaid, and M. Maaroufi, "Single-sensor based mppt for photovoltaic systems," *International Journal of Renewable Energy Research (IJRER)*, vol. 6, no. 2, pp. 570–579, 2016.

[110] A. Yoon, X. Yi, J. Martin, Y. Chen, and K. Haran, "A high-speed, high-frequency, air-core PM machine for aircraft application," in *2016 IEEE Power and Energy Conference at Illinois (PECI)*, 2016, pp. 1–4.

[111] A. D. Anderson, Y. Wang, Y. Yu, and K. S. Haran, "Experimental validation of a high-power slotless stator," in *2019 IEEE International Electric Machines Drives Conference (IEMDC)*, 2019, pp. 1564–1569.

[112] Z. Zhang, W. Geng, Y. Liu, and C. Wang, "Feasibility of a new ironless-stator axial flux permanent magnet machine for aircraft electric propulsion application," *CES Transactions on Electrical Machines and Systems*, vol. 3, no. 1, pp. 30–38, 2019.

[113] Z. Song, C. Liu, and H. Zhao, "Comparative analysis of slotless and coreless permanent magnet synchronous machines for electric aircraft propulsion," in *2019*

22nd International Conference on Electrical Machines and Systems (ICEMS), 2019, pp. 1–6.

[114] D. D. Tremelling, "On the design and analysis of a printed circuit board in a high speed surface permanent magnet axial flux machine," Ph.D. dissertation, University of Wisconsin-Madison, 2009.

[115] P. Guedes-Pinto, "High efficiency axial flux PM machines," Aug 2020.

[116] F. Profumo, A. Tenconi, M. Cerchio, J. F. Eastham, and P. C. Coles, "Axial flux plastic multi-disc brushless pm motors: performance assessment," in *Nineteenth Annual IEEE Applied Power Electronics Conference and Exposition, 2004. APEC '04.*, vol. 2, 2004, pp. 1117–1123 vol.2.

[117] M. Aydin, M. Gulec, Y. Demir, B. Akyuz, and E. Yolacan, "Design and validation of a 24-pole coreless axial flux permanent magnet motor for a solar powered vehicle," in *2016 XXII International Conference on Electrical Machines (ICEM)*, 2016, pp. 1493–1498.

[118] M. S. Islam, R. Mikail, and I. Husain, "Slotless lightweight motor for aerial applications," *IEEE Transactions on Industry Applications*, vol. 55, no. 6, pp. 5789–5799, 2019.

[119] X. Wang, C. Li, and F. Lou, "Geometry optimize of printed circuit board stator winding in coreless axial field permanent magnet motor," in *2016 IEEE Vehicle Power and Propulsion Conference (VPPC)*, 2016, pp. 1–6.

[120] F. Tokgöz, G. Çakal, and O. Keysan, "Design and implementation of an optimized printed circuit board axial-flux permanent magnet machine," in *2020 International Conference on Electrical Machines (ICEM)*, vol. 1, 2020, pp. 111–116.

[121] M. G. Kesgin, P. Han, N. Taran, D. Lawhorn, D. Lewis, and D. M. Ionel, "Design optimization of coreless axial-flux PM machines with Litz wire and PCB stator windings," in *2020 IEEE Energy Conversion Congress and Exposition (ECCE)*, 2020, pp. 22–26.

[122] S. Neethu, S. P. Nikam, A. K. Wankhede, S. Pal, and B. G. Fernandes, "High speed coreless axial flux permanent magnet motor with printed circuit board winding," in *2017 IEEE Industry Applications Society Annual Meeting*, 2017, pp. 1–6.

[123] B. L. Schuler, R. Lee, and J. Rasmussen, "System and apparatus for axial field rotary energy device," U.S. Patent 10 727 712B2, 07 28, 2020.

[124] J. D. Jore and M. B. Jore, "Conductor optimized axial field rotary energy device," U.S. Patent 7 109 625B1, 06 19, 2006.

[125] J. S. Smith, J. D. Duford, J. D. Jore, L. M. Jore, M. B. Jore, and B. J. Sullivan, "Methods and apparatus for overlapping windings," U.S. Patent 8 736 133B1, 05 27, 2020.

[126] G. Colinet, W. Lamberts, F. Baudart, and B. Dehez, "Investigation on the potential of pcb winding technology for high-dynamic and high-precision linear actuators," in *2020 IEEE Energy Conversion Congress and Exposition (ECCE)*, 2020, pp. 3615–3622.

[127] N. Verbeek and B. Dehez, "Comparison of inner and outer rotor configurations in slotless pm machines with pcb windings," in *2019 IEEE International Electric Machines Drives Conference (IEMDC)*, 2019, pp. 1–7.

[128] R. Del Rasario, "A future with hybrid electric propulsion systems: A NASA perspective," Turbine Engine Technology Symposium, 2014.

[129] "Magnix," accessed 08 Jan, 2020. [Online]. Available: https://www.magnix.aero/products

[130] X. Wang, C. Li, and F. Lou, "Geometry optimize of printed circuit board stator winding in coreless axial field permanent magnet motor," in *2016 IEEE Vehicle Power and Propulsion Conference (VPPC)*, 2016, pp. 1–6.

[131] N. Taran, V. Rallabandi, G. Heins, and D. M. Ionel, "A comparative study of conventional and coreless axial flux permanent magnet synchronous motors for solar cars," in *2017 IEEE International Electric Machines and Drives Conference (IEMDC)*, 2017, pp. 1–7.

Vita

Damien Lawhorn, PhD Candidate

Department of Electrical and Computer Engineering, University of Kentucky

Damien Lawhorn is a Ph.D. candidate and a NASA Graduate Fellow in the SPARK Laboratory, Electrical and Computer Department at University of Kentucky (UK). After receiving his B.S. in Electrical Engineering from UK in 2017, he worked as a summer intern in the TwinBuilder development team at the ANSYS Inc. headquarters where he developed power electronic models for various applications. Since 2017, Damien has worked at UK on NASA sponsored research projects and as an intern at the NASA Glenn Research Center (GRC) for three summers, contributing to the development of motor drives for NASA's first all-electric aircraft, the X-57 Maxwell, as well as to advancements toward MW hybrid-electric propulsion systems. At the UK ECE Graduate Research Symposium in 2019, Damien received the award for Best PhD Student Research Presentation and in 2018, he was recognized as an Electric Motor Education and Research Foundation Scholar. Damien is a founder of the Kentucky Organization of Robotics and Automation, a multidisciplinary student-led club, which has competed in a NASA driven national competition, and Executive Committee member of the UK IEEE PES and IAS student chapter. His current research focuses on power electronic converters, electric machines and drives, and power systems and components for aircraft with electrified propulsion.